University of Alberta

Distributed Activation Energies Modeling of Athabasca Vacuum Residue Pyrolysis

by

Sayid Mohammad Ghafelebashi Zarand

A thesis submitted to the Faculty of Graduate Studies and Research
in partial fulfillment of the requirements for the degree of

Master of Science
in
Chemical Engineering

Department of Chemical and Materials Engineering

Spring 2014
Edmonton, Alberta

Abstract

The kinetics of the thermal decomposition of Athabasca vacuum residue (AVR) has been studied by thermogravimetric analysis. Three heating rates of 0.5, 10 and 25 K/min were used to investigate the consistency of kinetic parameters. The Weibull and Gaussian distribution functions were found to be the best distribution functions for fitting the curve of differential of conversion with respect to time. The effect of pre-oxidation at low temperature with and without goethite α-FeO(OH) as a catalyst for oxidation was investigated in closed reactor. A three lump reaction network modeled the thermal cracking and the kinetics of AVR. Based on the obtained activation energies, it was found that goethite has a negligible effect as a catalyst during pre-oxidation. The difference among the calculated activation energies indicated that pre-oxidation resulted in the polymerization the vacuum residue molecules, The resulting pre-oxidized material was subsequently more resistant to thermal cracking than the unreacted feed.

Acknowledgements

I would like to acknowledge and thank my supervisor, Dr. William McCaffrey for his continuous guidance, advice, support and friendship. Thank you for your patience and for helping me during the development of the experimental and modeling techniques.

I would like to express my special thanks to my parents for their insight, constant support and encouragement without which this could not have been possible.

Thank you to the CME machine shop for providing me all of the equipment and materials with the most convenient and the quickest way they could have.

Finally, I would like to thank all of my friends (too many to list here) to providing friendship and support that I needed.

Table of Contents

List of Tables

List of Figures

List of Abbreviations

AIC	Akaike information criteria
AVR	Athabasca vacuum residue
BIC	Bayesian information criteria
MCR	Microcarbon residue
mg	Milligram
mm	Millimeter
rpm	Rotations per minute
PVDF	Polyvinylidene fluoride
RSS	Residual sum of square
TGA	Thermogravimetric analysis
THO	Threshold oxygen
VR	Vacuum residue

Chapter 1: Introduction and Objectives

Heavy oils from around the world contain a significant fraction of material that boils over 524 ℃. This fraction is called the residue fraction. Vacuum residue is often described as the heaviest fraction of petroleum that is produced at the bottom of the vacuum distillation tower in a refinery (1). Generally, residues need to be upgraded before they can be used in conventional oil refineries. Pyrolysis is a widely used process to upgrade residues and produces gaseous products, gas oil and coke from bitumen or vacuum residue (2). Vacuum residue can be characterized as a highly viscous hydrocarbon containing high percentage of sulfur, nitrogen, and heavy metals (vanadium and nickel), and a low hydrogen/carbon ratio (1). Many studies on vacuum residue pyrolysis using thermogravimetric analysis (TGA) have been carried out to determine the kinetic characteristics of pyrolysis and the associated kinetic parameters (4-7). The complexity of the physical and chemical processes occurring in the TGA, however, make data analysis highly complex.

The properties of vacuum residue depend on the oil source and subsequent downstream processing. One common product manufactured from vacuum residue is paving asphalt (3). The quality of this asphalt is significantly related to its chemical compositions. High softening point asphalts are commonly generated by partial oxidation of the vacuum residue (8). Oxidation results in a decreased amount of saturate content and an increase in the amounts of toluene insoluables and asphaltenes. Oxidized vacuum residue has been reported to also have an increased activation energy of pyrolysis when compared to unoxidized residues (8).

Previous researchers have considered a number of kinetic expressions for pyrolysis of oil shales in an open reactor (TGA) based on three reaction schemes:

(1) first-order reaction (4, 5)

(2) consecutive first-order reactions (6)

(3) parallel first order reactions (7).

One of the objectives of this project is the evaluation of kinetic parameters of Athabasca vacuum residue from traditional and distribution of activation energies methods to minimize the error of calculation for such a complex material. To correct for this error, the most popular distribution functions, Gaussian, Weibull and Gamma, were used to determine the kinetic parameters. Both first order and parallel first order reaction schemes will be evaluated. Another objective is to look at the catalytic effect of α-FeO(OH) to oxidize Athabasca vacuum residue in a closed reactor. Previous work has shown the catalytic effect of low cost iron-based mixed oxides in oxidation (9). In this project, at first a kinetic model which can explain the reaction behavior of Athabasca VR in closed reactors is introduced, and then with respect to this model, catalytic effect of goethite α-FeO(OH) is explored by quantifying the change of the activation energy of pyrolysis.

Chapter 2: Literature Review

2.1: Structure of Bitumen/Heavy Oil

To predict thermal cracking and catalytic behavior of heavy oil during upgrading, it is important to understand both the physical and chemical properties of the feed. The hydrocarbon components of bitumens and heavy oils are classified into four general classes (10, 11):

1. Paraffins – this class consists of straight or branched chains without any ring structures. In Athabasca vacuum residue, paraffins are covalently linked to other hydrocarbon groups. In hydrocarbons from other sources, paraffins can account for as much as 2/3 of the total oil, such as in the case for light crude oils.
2. Naphthenes – this class contains one or more rings of saturated hydrocarbons, paraffinic side chains might be attached to this class.
3. Aromatics – this class has one or more fused aromatic rings, and may be attached to naphthenic rings and/or paraffinic side chains.
4. Olefins – this class consists of unsaturated hydrocarbons that have one or more double bonds, but no ring structures.

In bitumen and heavy oil, the amount of naphthenes and aromatics are greater than the paraffins, generally this trend is holds as the molecular weight, or boiling point increases. The chemical structure of heavy oil is extremely complicated; this petroleum feedstock is thought to contain up to 10^5 to 10^6 various molecules in a complex mixture of hydrocarbons, heteroatoms and metals (10, 11). Bitumen and heavy oil are very difficult to upgrade due to the high levels of nitrogen, sulfur and oxygen (12). These molecules can work as inhibitors that cause poisoning and deactivation of catalyst. A major portion of sulfur compounds can be easily removed over hydrotreating but some of them are

refractory (10). Whitehurst et al. (13) considered the hydrodesulfurization of polyaromatic sulfur compounds. They demonstrated that as long as the sulfur is in ring compounds like thiophene and benzotheophene the sulfur can be easily eliminated. As the boiling point of an oil fraction increases, the nitrogen content generally rises as well. The amount of nitrogen in heavy oil (0.1-0.9wt%) is much less than the amount of sulfur (6.5wt%), with some bitumens having up to 2wt% of nitrogen (14). Nitrogen concentration starts rising remarkably around 350 ℃ and keeps increasing with boiling point (10). The work by Holmes (15) also showed that pyridinic structures, including quinolones and acridines are the most common forms of nitrogen in heavy oil. Oxygen content in bitumen is relatively low, usually less than 1 wt%. Oxygen-containing molecules in bitumen include phenols, carboxylic acids, esters, ketones and cyclic and acyclic ethers. Ketones, esters, ethers and anhydrides are generally observed in the heavy oil fractions with higher molecular weights (16).

2.2: Reaction Behavior of Bitumen in Cracking

The main thermal upgrading process occurs at temperatures above 420 ℃ where C-C bonds dissociate at a significant rate. Highly activated free radicals are produced during the homolytic dissociation of bonds in thermal cracking of liquid phase hydrocarbons. These free radicals have an extremely active potential with an unpaired electron [19]. These short-lived radicals that participate in chain processes are only in existence in very low concentrations, as would be expected for any reactive intermediates, but they make a remarkable effect on conversion of the feed mixture. The minimum amount of energy needed to break chemical bonds is very significant as illustrated in Table 2-1. The observed activation energies (actual activation energy) for cracking of residues and pure compounds are usually less than the minimum energy required to homolytically break a

stable chemical bond (21). Olmstead and Freund (22) showed that the activation energy for cracking of Arab Heavy and Cold Lake residues is 212.8 – 216.7 kJ/mol. This number is less than even the lowest activation energy in table 2-1. A high activation energy is required to produce the radicals at the initiation step, but the propagation of radicals through numerous hydrogen abstraction and beta-scission steps requires a lower energy, therefore the overall reaction progresses at a reasonable rate (21). The detailed kinetics of this chain process are represented by the example of thermal cracking n-alkanes. Rice and Hertzfeld (20) elucidated that active free radicals play the primary role in thermal cracking of n-alkanes. The following steps are hypothesized for a generalized chain reaction of an alkane (20):

Initiation: $M \rightarrow R_i^* + R_j^*$ 2-1

Propagation:

Intermolecular Hydrogen Abstraction

$R_1^* + M \rightarrow R_1H + M^*$ 2-2

Intramolecular Hydrogen Abstraction

$^*R\text{-}C\text{-}C\text{-}\beta_j \rightarrow R\text{-}C\text{-}C\text{-}C^*\text{-}\beta_j$ 2-3

β - Scission $M^* \rightarrow n\text{-}R_2^* + \text{Olefin}$ 2-4

Radical addition $R_i^* + C{=}C\text{-}R_k \rightarrow R_i\text{-}C\text{-}C^*\text{-}R_k$ 2-5

Termination

Recombination $R_i^* + R_j^* \rightarrow R_iR_j$ 2-6

Disproportionation $M^* + M^* \rightarrow MH + \text{Olefin}$ 2-7

Where M and M* are the parent alkane and the parent radical, R_1^* and R_1H are the methyl or R_i^* can be the butyl or higher radical.

Table 2-1. Bond dissociation energies (19)

Chemical Bonds	Energy, kJ/mol
H-H	436
H-O	464
H-S	368
H-N	390
C-C (aliphatic)	355
C=C	611
C≡C	837
C-H (n-alkanes)	410
C-H (aromatic)	462
C=O	805
C=N	615
C-S	322
C-N (in amine)	351
O=O	498
N-O	631
C-O (in methoxy)	343
H-Cl	432
C-Cl	330
N-Cl	200
O-Cl	200
S-Cl	250
N≡N	945
S-O	265
N-N	160
O-O	204

The use of a free radical chain reaction for a complex hydrocarbon mixture like bitumen is much more complicated. Poutsma (23) reviewed the behavior of chain reactions in the cracking of crude oils. He explained that chain reactions could describe the cracking of a

wide range of aromatic components attached to two or more alkyl carbons, but non-chain reactions could only describe the cracking of unsubstituted and methyl-substituted aromatics. A major difference between chain and non-chain cracking is the reaction rate. In non-chain cracking, bond breakage involves only homolytic scission without the existence of the chain reaction and termination reactions; as a result, the reactions are very slow due to the relatively high bond dissociation energies, as shown in Table 2.1. Whereas in chain reactions, lower energy propagation steps create a remarkable decrease in the energy required for reaction; consequently, it increases the rate (21). Liquid phase cracking generally proceeds faster than gas phase cracking due to the higher density of molecules in the liquid compared to that of the gas phase, so the chance of liquid phase molecules interacting with radicals is higher than for lower density gas phase molecules. Wu et al. (24) investigated the reaction behavior in the liquid phase and in the vapor phase for the thermal cracking of n-hexadecane. He showed that hydrogen abstraction is faster in the liquid than in the gas phase. This difference in the propagation step decreases the tendency of β – scission in the vapor phase; as a result, the yield of olefins and alkanes in the vapor is equal to the yield of olefins and alkanes in the liquid.

Blanchard and Gray (20) considered the role of free radical chain reactions in the cracking of vacuum residue. Athabasca vacuum residue (524 +℃) was dissolved in 1-methyl-naphthalene at an approximate molar concentration of 1.2%. Following the above mechanism, hydrogen is abstracted from the solvent, 1-methylnaphthalene, by free radical bearing vacuum residue fragments to produce benzylic radicals. This phenomenon has two traceable effects: first, it reduces the rate of cracking of the vacuum residue, and secondly, the rate of radical recombination in the residue is also reduced because the majority of radicals are residing on solvent molecules. The average conversion of Athabasca residue after the reaction in an autoclave at 400 ℃ under 13.8 MPa hydrogen

pressure for 30 min was 48.6%, but the conversion of the diluted residue in 1-MN reduced to an average of 35.7%. These data support the above mechanism and showed that homolytic scission reactions generated from radical stabilization would not solely explain the cracking mechanism of the residue (20).

2.3: Kinetic Models of Vacuum Residue Cracking

2.3.1: Open Reactor Modeling

The mechanistic modeling of heavy oil cracking is very difficult due to its complex and heterogeneous chemical composition. The number of individual molecules in a vacuum residue has been measured by modern analytical measurements in the order of 10^5-10^6 (27). As a result, most kinetic studies involve lumped models. Ho Young Park et al. (1) have considered the properties of vacuum residue to investigate the utilization of this material as a fuel for commercial boilers. He performed non-isothermal pyrolysis of the VR in a thermogravimetric analyzer (TGA) at heating rates of 2, 5, 10 and 20 ℃/min from room temperature to 800 ℃ in a nitrogen atmosphere. The pyrolysis had two steps of mass loss, which was perfectly modeled by two first-order reaction models in series. The reaction occurred in a quartz tube (34 mm inside diameter and 300 mm length) surrounded by heating elements. Nitrogen as the purge gas was passed through the inside of the tube with a flow rate of 300 ml/min. The VR was heated to 800 ℃ at heating rates of 2, 5, 10 ℃/min. Yue and Watkinson (28) used a two-step first-order reaction model to describe the pyrolysis process of two residue samples. Based on this model, for an nth-order reaction the Arrhenius equation would be:

$$\frac{dV}{dt} = k_0 \exp^{-\frac{E}{RT}} (V^* - V)^n \qquad 2\text{-}8$$

Where k_0 is frequency factor, E is the activation energy, n is the reaction order, R is the gas constant, T is the reaction temperature, V^* is the final yield of the gaseous phase and V is the gaseous phase yields at time. Temperature at any time t in the non-isothermal TGA experiment is presented by:

$$T=mt + T_0 \qquad 2\text{-}9$$

Where T_0 is the starting temperature, and m is the heating rate. With substitution of the equation dT=mdt, Eqn. 2-8 becomes (1):

$$\frac{dV}{dT} = \frac{k_0}{m}\exp^{-\frac{E}{RT}}(V^* - V)^n \qquad 2\text{-}10$$

The integration of Eqn. 2-8 for the first order, n=1, of the above equation gives:

$$V = V^*\left\{1-\exp\left[-\frac{k_0 RT^2}{mE}\exp^{-\frac{E}{RT}}\left(1-\frac{2RT}{E}\right)\right]\right\} \qquad 2\text{-}11$$

$$\frac{dV}{dT} = \frac{k_0 V^*}{m}\exp\left[-\frac{E}{RT}-\frac{k_0 RT^2}{mE}\exp^{-\frac{E}{RT}}\left(1-\frac{2RT}{E}\right)\right] \qquad 2\text{-}12$$

A non-linear least squares method was used to fit the predicted result with the experimental data. Finally, the kinetic parameters, k_0 and E were derived (1).

The following equation was used to calculate the standard deviation (SD) (1):

$$SD = \left[\sum_i^N (V_{i-\exp} - V_{i-calc})^2 \Big/ (N-p)\right]^{1/2} \qquad 2\text{-}13$$

Where $V_{i\text{-}calc}$ is the predicted volatile yield, $V_{i\text{-}exp}$ is the experimental volatile yield at data point I, p is the number of parameters to fit the data and N is the number of data points.

Yue and Watkinson (28) concluded that based on their results from the vacuum residues during the pyrolysis, the reaction behavior of the VR changes continuously. Therefore, they concluded that the two-step first-order reaction model is more reliable than the one-step method (1, 28, 29).

Olmstead and Freund (22) studied the thermal cracking of Arab Heavy and Cold Lake residues. They utilized an isothermal process by TGA to calculate the kinetic parameters. In their work, the effect of evaporation could be ignored in their calculation because they used a high boiling point vacuum residue. TGA shows only the weight loss as a function of time or temperature. Therefore, the simple evaporation of light molecules cannot be differentiated from those molecules produced by reactions. To determine the evaporation and reaction regions, Olmstead and Freund (22) heated three distillate fractions using a linear temperature program. They observed that light fractions of oil exhibit significant weight loss starting at 225 ℃, and reached a maximum rate at 375 ℃. Using a flame ionization detector, Olmstead and Freund showed that the samples of vacuum residues used in their experiments did not contain any light fractions and therefore evaporation of preexisting light materials would not impact their results. On the other hand, the weight loss of intermediate distillation fractions begins at 330 ℃, and reaches a maximum rate at 430 ℃. In their experiments, Olmstead and Freund observed a maximum peak for the detected gas. It was deduced that the intermediate boiling fraction accounted for a large portion of reactions in vacuum residues. Later work showed that the mass loss of the highest boiling fraction was mainly due to thermal reactions. This mass loss started at 390 ℃ and reaches a maximum rate at 475 ℃. As a result, the highest boiling fractions of vacuum residue were used as an appropriate feed to study heavy oil pyrolysis reactions in a TGA. In order to obtain good kinetics, isothermal measurements have measured over the temperature range of 400-530 ℃ (22). Rate constants of the isothermal process have

been plotted as a function of the experiment temperature following the classical Arrhenius law (22).

$$k = A\exp(-\frac{E}{RT}) \qquad 2\text{-}14$$

$$\ln k = \ln A + \frac{-E}{RT} \qquad 2\text{-}15$$

Where k is the reaction constant, A is the pre-exponential factor, E is the activation energy, R is the gas constant and T is the isothermal temperature. Based on the above equations, the activation energy and pre-exponential factor can be calculated with the slope and intercept of the plot of ln(k) versus 1/T, respectively.

Table 2-2. Arrhenius Parameters for thermal conversion (22)

Isothermal TGA	Arab Heavy Oil 698 ℃ residue
Log A, sec^{-1}	13.33
E_a, kJ/mol	216.7

Generally, there are some advantages for non-isothermal thermogravimetric analysis compared to the classical isothermal method. First, the non-isothermal method omits the errors produced by the thermal induction period, and secondly, the non-isothermal process covers a wide temperature range of interest (30). The following expression describes the decomposition of a first-order reaction:

$$\frac{dX}{dt} = k(1-X) \qquad 2\text{-}16$$

By substituting Arrhenius activation energy and pre-exponential factor, Eq. 2-16 becomes:

$$\frac{dX}{dt} = A\exp(-\frac{E}{RT})(1-X) \qquad 2\text{-}17$$

For a non-isothermal process, Eq. 2-17 can be changed by presenting the heating rate as (30):

$$\frac{dX}{dT}\frac{dT}{dt} = A\exp\left(-\frac{E}{Rt}\right)(1-X) \qquad 2\text{-}18$$

or

$$\frac{dX}{dT} = (A/b)\exp\left(-\frac{E}{Rt}\right)(1-X) \qquad 2\text{-}19$$

Where b is dT/dt .

The Chen-Nuttall model is one of the popular models used for the non-isothermal process. In this model, Eqn. 2-19 is rearranged and integrated to become (30):

$$1-X = \exp\left\{-(A/b)\int_0^T \exp(-\frac{E}{RT})dT\right\} \qquad 2\text{-}20$$

or

$$1-X-\exp\left\{-\frac{A}{b}\frac{RT^2}{E+2RT}\exp\left(-\frac{E}{RT}\right)\right\} \qquad 2\text{-}21$$

Rearranging Eqn. 2-21 gives:

$$\ln\left\{\frac{E+2RT}{T^2}\ln\frac{1}{1-X}\right\} = \ln\frac{AR}{b} - \frac{E}{RT} \qquad 2\text{-}22$$

This equation can be written as a linear equation:

$$y=mx + c \qquad 2\text{-}23$$

Where

$$y = \ln[\frac{E + 2RT}{T^2} \ln \frac{1}{1 - X}] \quad 2\text{-}24$$

$$m = \frac{-E}{R} \quad 2\text{-}25$$

$$c = \ln(\frac{AR}{b}) \quad 2\text{-}26$$

$$x = \frac{1}{T} \quad 2\text{-}27$$

With a trial and error method, the values of slope and intercept can be obtained. First, y (Eqn. 2-24) is calculated by the initial guess of E. Secondly, y is validated by the obtained values of E from Eqn. 2-25, and m and c are recalculated from the regression at different temperatures. This process is iterated until the required accuracy of E and A is attained (30).

The Coats and Redfern method is another method, which Ahmarruzzaman (31) used to model the kinetic behavior of Basra vacuum residue. In this model, the reaction rate of the solid component A is presented by:

$$A \rightarrow gas + oil + char$$

The general rate expression for decomposition of a solid material is:

$$\frac{dX}{dt} = k(1 - X)^n \quad 2\text{-}28$$

According to the Coats and Redfern method, the above equation for an n^{th}-order reaction is given by:

$$\ln\left[\frac{1 - (1 - X)^{1-n}}{(1 - n)T^2}\right] = \ln\left\{\left(\frac{AR}{bE}\right)\left(\frac{1 - 2RT}{E}\right)\right\} - \frac{E}{RT} \quad 2\text{-}29$$

Where b is dT/dt. This method requires establishing an initial value for n (order of reaction) and then iterating to find the optimal parameter values that satisfy Eqn. 2-29. Therefore, the left hand side can be plotted for different temperatures as a linear function of 1/T, and activation energy and pre-exponential factor can be found from the slope and the intercept of the line, respectively (31).

2.3.2: Closed Reactor Modeling

Non-catalytic thermal racking processes are broadly used in the upgrading of vacuum residue and bitumen and include fluid coking, visbreaking and delayed coking. The main purpose of these processes is to increase and maximize liquid yield and minimize coke and gas yield. The yield coke depends on the carbon residue content of the initial feed, for instance, 28 wt% coke is produced by a carbon residue content of 20 wt% in a delayed coker (69). From the starting time of commercialization of fluid coking, the objective for several new thermal cracking processes has been to reduce both the vapor phase and liquid phase residence times of the products. Shorter residence time in the vapor phase decreases light ends formation, which removes hydrogen from the liquid products. In the meantime, long residence time (high severity) is favorable for the high boiling point material in the liquid phase to make maximum yield of vaporized products and to reduce fouling by viscous unreacted liquid. In fluid coking the liquid is retained in a liquid fluid bed for a residence time much longer the vapor phase. Higher reaction temperatures are required, with concurrent transport of vapor and liquid, above the highest point of the fluid coking range, which is 550 ℃ (68). As the temperature increases and the reactions in the liquid phase accelerate, the variety of products is more controlled by the rate of heat transfer into the liquid feed and the rate of transport of cracked liquid products out of the liquid phase. The liquid phase residence time of the cracked products should be as

short as possible. For instance, when the liquid phase reactions are complete, the length of diffusion path of the cracked products in the liquid phase changes the product distribution and the coke yield at long reaction times.

Gray et al (32) have tested the hypothesis that reduction of the liquid film thickness, and therefore the diffusion resistance, would result in a decrease in the coke yield and an increase in the liquid film products. They found that the coke yield at long reaction times decreased monotonically with a reduction in the liquid film thickness between from 50 to 20 μm. McCaffrey et al (69) have hypothesized that the coke yield at a given reaction temperature can be minimized by reducing the liquid film thickness to below 20 μm, by minimizing addition reactions of the cracked products in the liquid phase. Thus, they designed an experiment to minimize the effect of the liquid phase mass transfer resistance in thermal cracking of vacuum residue. An average diameter size of coke particles, less than 190 nm, was generated; therefore, the average particle size of feed was estimated to be less than 550 nm. The high ratio of surface to volume of feed particles could promote vaporization. The insensitivity of the coke yield to conversion and reaction temperature indicates that all the components with a chemical structure which can have thermal cracking reactions were evaporated and leave only the fractions behind which can not undergo non-catalytic thermal cracking reaction and form intrinsic coke. As a result, as the ratio of hydrogen to carbon reduces in the collected liquids, the aromaticity increases significantly with increase in conversion (69).

The role of the coking processes in the production of lighter, desired, products from heavy fractions of oil is significant. Many complicated reaction phenomena, including phase behavior and transport of heat, mass, and momentum are involved in this process. Despite the extensive use of coking processes, a significant number of fundamental issues are not well understood (32). Lumped kinetic schemes are effective to describe the

transformation of complex materials by collecting and defining a large number of molecules into individual lumps. Gray et al. (33) suggested a reaction plot for the devolatilization and cracking of the bitumen films, based on a lumped scheme for conditions up to 530 ℃. In their lumped reaction mechanism, Figure 2-1, the mass transfer parameters have been simplified in the overall kinetic model, and mass transfer was only considered for the release of vapor phase products from the liquid phase. Gray et al. (33) showed that the ultimate coke yield does not depend on temperature ranging from 475 ℃ to 530 ℃ at low film thicknesses (=$20 \pm 2\mu m$). They also demonstrated that, as the initial film thickness of vacuum residue grows from 20 to 80 μm, the coke yield increases because of components trapped in the coke phase. The key role of mass transfers inside the reacting liquid phase is described by the coke yield and the film thickness. Wiehe (34) described that coke formation during the pyrolysis process is caused by two different mechanisms. These two cokes are called intrinsic and extrinsic cokes. Intrinsic coke originates from large aromatic cores in the feed, which are not involved with reaction and vaporization. Those molecules, which have aromatic species with more than five rings, have a high boiling point and the required energy for bond scission is pretty high. According to this theory, heavy residue has a high tendency to form intrinsic coke. Polymerization and recombination of the lighter fractions are responsible for extrinsic coke formation (34). Dutta et al. (35) showed that as the residence time of the cracked products in the liquid film increases the amount of extrinsic coke formation would increase due to recombination reactions. Following the above descriptions, Radmanesh et al. (27) proposed a lumped reaction mechanism including both types of coke formation from the thermal cracking of heavy oil (+650 ℃), Figure 2-1. All the reactions were hypothesized to be first order reaction except for the recombination reactions leading to extrinsic coke formation, which were assumed to be

second order (27). From these results, it is clear that the final coke yield is dependent on the reaction path.

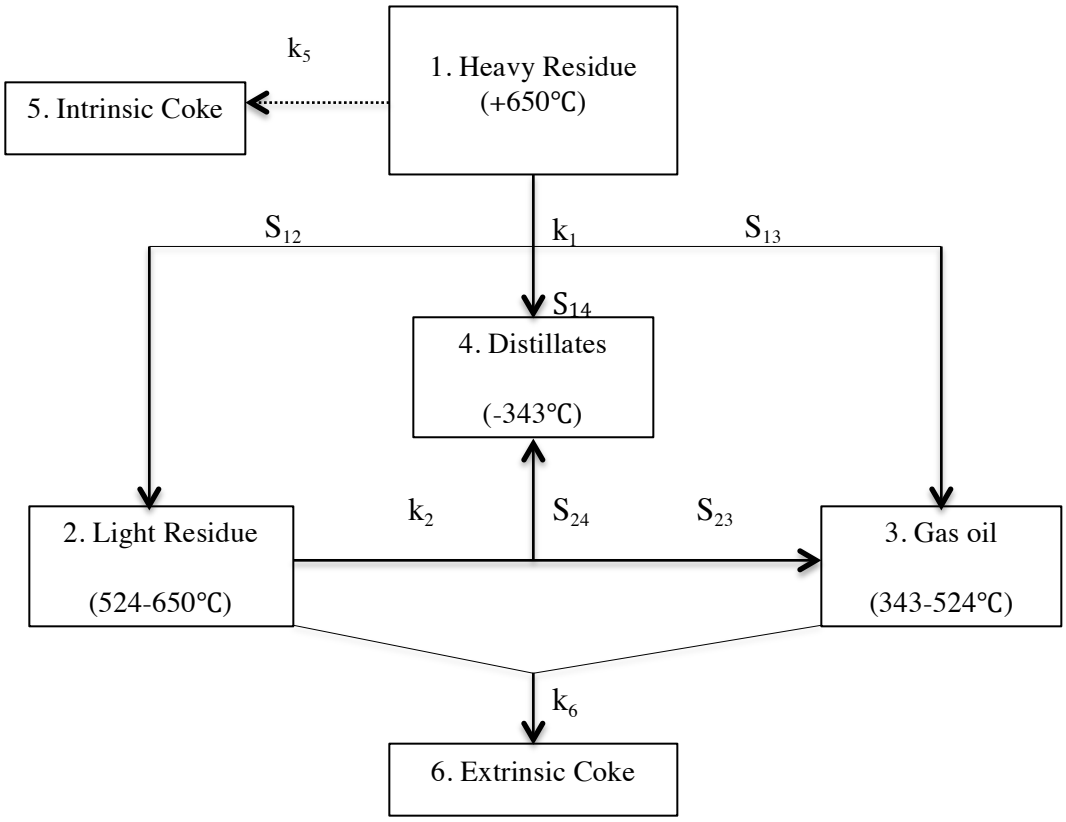

Figure 2-1. Reaction diagram for thermal cracking of heavy residue (27)

S is the selectivity coefficient for different reactions. As the reaction proceeds, the dominance of the internal mass transfer inside the sample was determined by the estimates of the mass transfer Biot number of thermal cracking of the ingredient in the liquid film:

$$\frac{\partial \omega_i}{\partial t} = \frac{\partial}{\partial}\left(D_i \frac{\partial \omega_i}{\partial z} \right) + r_i \qquad 2\text{-}30$$

Where i is the lumped fractions in the model, ω_i is the mass fraction of component i in the liquid phase and D_i is the diffusivity of component i in the solution, r_i is the net rate of component i formation and is evaluated at the reaction temperature. The following diffusivity data can be calculated from viscosity data and the estimated Wilke-Chang equation (36) of the liquid bitumen:

$$D_{AB} = 7.4 \times 10^{8} \frac{(M)^{2/3} T}{\mu^{2/3} V_A^{0.6}} \qquad 2\text{-}31$$

As more coke is created, viscosity and diffusivity change. The following empirical correlation was used to make a relation between the viscosity of the solution and coke concentration in the liquid phase:

$$\eta_r = \frac{\mu}{\mu_0} = 1 + [\eta] X_c^{\alpha} \qquad 2\text{-}32$$

Where μ and μ_0 represent viscosity at any coke concentration and at X_c=0, respectively. X_c is the coke concentration, and $[\eta]$ and α are constants (37). Evaporation occurs at the interface of the liquid and gas phases. The mass flux of the products, which are removed from the film at the interface, is given by (27):

$$N_i = K_{Gy}(y_i^* - y_i) \qquad 2\text{-}33$$

Where y_i is the mole fraction of component i in the nitrogen stream which is nearly equal to zero, y_i^* is the concentration of the component i at the interface of the liquid and gas phases, and K_{Gy} is the coefficient of mass transfer in the gas phase approximated from the correlation of Tosun (38). The equilibrium constant, which determines the volatility of each lump, is given by:

$$K_i = \frac{y_i^*}{x_i^*} \qquad 2\text{-}34$$

After rearranging Eqn. 2-33 with Eqn. 2-34 and converting the units to a mass basis, the boundary condition is simplified to Eqn. 2-35 for a flux at z=δ:

$$F_{i,z=\delta} = \rho D_i \frac{\partial \omega_i}{\partial z} = K_{Gy,i} K_i \omega_i M_i \qquad 2\text{-}35$$

An average mass fraction can be obtained by solving the above equation with Eqn. 2-35 in parallel. Finally, the kinetic parameters may be estimated by minimizing the square of errors between the experimental and predicted results. This objective function was defined as follows:

$$SSQ = \sum_i \left(\frac{\omega_i^{model} - \omega_i^{exp}}{Max(\omega_i^{exp})} \right)^2 \qquad 2\text{-}36$$

Table 2-3 (27) shows the calculated parameters, which estimated the best fit of the predicted and experimental results (33).

Table 2-3. Estimated kinetic parameters (27)

Reaction	Apparent activation energy $E_{a,I}$ (kJ/mol)	Apparent pre-exponential factor, log (A_i), (s^{-1})
Cracking of heavy residue (1)	230 ± 1	14.00 ± 0.5
Cracking of light residue (2)	188 ± 1	11.00 ± 0.5
Intrinsic coke formation (5)	33.7 ± 0.4	1.0 ± 0.2
Extrinsic coke formation	99.6 ± 1	5.0 ± 0.2

2.4: Oxidation of Vacuum Residue

Oxidation of vacuum residue is generally used to produce high softening point asphalt for paving applications. The extent of oxidation depends on the blown air quantity, time,

and operation temperature. Researchers have proposed a serial reaction for the change among different components of the residue in continuous oxidation processes (39). In asphalt producing processes, a wide range of reactions occurs during the oxidation of short residue, such as oxidative dehydrogenation, dealkylation, oxidative polymerization and polyconsolidation. Hydrogen loss is involved in the residue consolidation process during oxidation. The residue consolidation process and cyclization reactions bring about the formation of asphaltenes, including high molecular weight products with high aromaticity(41). The number of compounds with short alkyl chains $(CH_2)_n$ ($n \leq 4$) during oxidation increases because of the dealkylation reactions; the C:H ratio and the quantity of benzene rings in the cycles in the oxidized residue increase as well. The following figure shows the change of chemical components during oxidation.

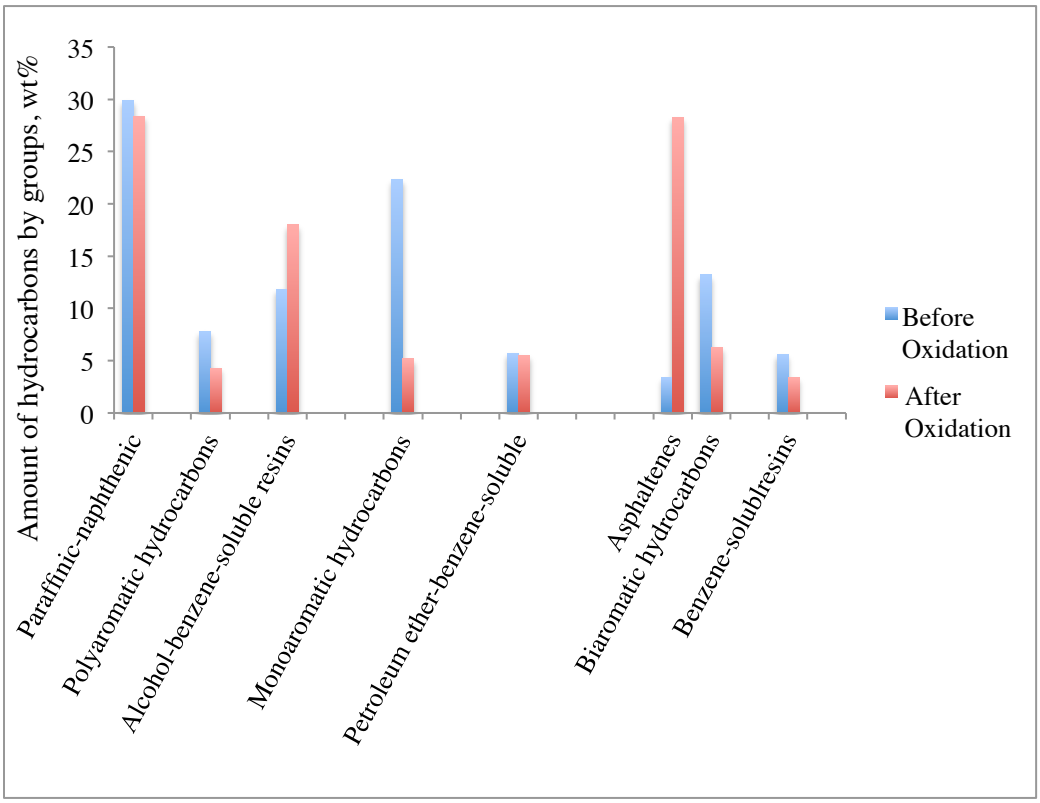

Figure 2-2. Change in the chemical constituents of petroleum residue during oxidation (41)

Aromatic hydrocarbons in petroleum have been shown to have the highest reactivity towards oxidation when compared to the other components in petroleum. The primary products of oxidation are alcohol-benzene-extractable heavy resins and asphaltenes.(41). S. V. Kotov et al. (41) also showed that an increase in the specific viscosity of the residue causes an increase in the oxidation rate constant. As a result, the oxidation rate constantly increases as the concentration of paraffin-naphthene hydrocarbons decreases and aromatic hydrocarbons increases due to an enhancement in the specific viscosity (41). Mukesh Kumar Suha et al. (3) used ozone (O_3) as a strong oxidizing agent. Ozone can oxidize benzene and other aromatic components of the vacuum residue including PAHs. They exposed the liquid phase of vacuum residue to ozone at temperatures ranging from 100℃ to 150 ℃, and reported the production of oxygenated hydrocarbons. It was indicated that hydroxyl groups are the first formed which consequently convert to carbonyl or alkoxy groups. They used the Fourier transform infrared spectroscopy (FTIR) to show that the weight percentage of carbon, hydrogen, nitrogen, sulfur, nickel and vanadium reduced while oxygen content increased. Therefore, ozonation partially oxidized vacuum residue (3). Qi Yutai (8) has considered the serial reaction kinetics and variations of the amount of different constituents of Daquing vacuum residue and Huansalian vacuum residue during continuous oxidation reactions at temperature ranging from 210 ℃ to 310 ℃. He tested 150 g of the residue in a 500ml stainless steel reactor. He showed changes of the constituents of residues with oxidation, and the differences between the effect of oxidation on two various residues. The amount of saturates and aromatics of the two residues decreased gradually, and the amount of asphaltenes and toluene insoluble increased. On the other hand, the amount of resins increased at first, and then reduced as the oxidation time increased at a given temperature. Qi Yutai (8)

proposed a macroscopic description for the variation of constituents of the vacuum residue in continuous oxidation by a serial reaction, which is presented as follows:

Saturates → aromatics → resins → asphaltene → toluene insoluble

As is shown in the above serial reaction, the saturates and the toluene insoluble are the first and the final constituents, respectively. It is obvious that the saturates content always reduces, and toluene insoluble content increases with increased oxidation at any temperature. As the oxidation time proceeds, the values which are converted from saturates to aromatics or from aromatics to resins are less or more than those converted from aromatics to resins or from resins to asphaltenes. The amounts of aromatics or asphaltenes reduce or enhance with the oxidation residence time. The amounts that are converted from resins to asphaltenes are always more than those that are converted to toluene insoluble from asphaltenes; therefore, the amount of asphaltenes always increases during oxidation, and these changes are more significant at higher oxidation temperatures (8). Azfar Hassan et al. (40) investigated the effect of the concentration of oxygen on microcarbon residue (MCR). They showed that at a given oxygen concentration, the MCR may increase or reduce compared to the results in an inert atmosphere. For a given sample, the threshold oxygen concentration (THO) quantity may vary. THO is dependent on the experimental setup (whether TGA or muffle furnace). THO also varies depending upon the sample size. The TGA data clarify that besides pyrolysis occurring at all times during the heating of the sample, there are two challenging reactions called partial oxidation and combustion. These two reactions overcome each other depending upon the oxygen concentration where the sample is exposed. There would be an increase in MCR if the oxygen content worked as a free radical initiator and caused polymerization. If the

sample size is limited, then it leads to a low MCR value because the oxygen concentration would be sufficient for the combustion to dominate partial oxidation (40).

2.5: α-FeO(OH) as an Oxidation Catalyst

Iron based catalysts have been shown to have a low level of activity towards hydrocarbon reactions (67). The goal of this thesis is to evaluate waste streams from the aluminum industry that are rich in iron. The Bayer process produces a large amount of iron-rich red mud during alumina production. This waste can be characterized as either goethite or hematite rich. Hematite is the mineral form of iron(III) oxide Fe_2O_3, and goethite is an iron bearing oxide mineral. Goethite is an iron oxyhydroxide with the mineral form of α-FeO(OH). About 6×10^7 tons of red mud per year is produced and stored in a variety of locations all over the world (43). Based on the experimental results, it is understood that the alumina recovery of Bayer red mud may approach 89.71%. However, under the best conditions, Fe recovery rate and the grade of magnetite concentration are 60.67% and 61.78%, respectively. (44). Jorge Alvarez et al. (45) showed that major constituents of red mud are as follows: Rutile (TiO_2), Hematite (Fe_2O_3), Goethite (FeO(OH)), Iron Hydroxide ($Fe(OH)_3$), Hallosite($Al_2Si_2O_5(OH)_4$) and Byerite ($Al(OH)_3$). Goethite, α-FeO(OH), is one of the most popular forms of iron oxy-hydroxides in soil, sediment and red mud. The purpose of this study is to investigate the use of goethite in the upgrading of heavy oil. Goethite particles have a high specific surface area, more than 200 m^2/g, and a high propensity to oxyanions and heavy metals (44). Recently, the utilization of goethite and hydrogen peroxide showed that they would highly oxidize organic components. Ming-chun Lu (47) considered the effect of goethite particle size, goethite concentration, Fe^{2+} and Fe^{3+} on 2-chlorophenol oxidation. Hydrogen peroxide was used as a chemical oxidant. Hydrogen peroxide, however, is not

a suitable oxidant; therefore, it is incorporated with UV light, iron salts or ozone to produce more hydroxyl radicals. The reaction of hydrogen peroxide with ferric ions is called a Fenton-like reaction. Ferrous ions can be produced by the reduction of goethite, which is shown as below (47):

$$\alpha - FeOOH_{(s)} + 3H^+ + e^- \Leftrightarrow Fe^{2+} + 3H_2O \qquad 2\text{-}37$$

Regarding to the following equation, hydrogen peroxide provides electrons:

$$H_2O_2 \rightarrow 2H^+ + O_2 + 2e^- \qquad 2\text{-}38$$

Combining Eqs. 2-42 and 2-43, the following equation is derived:

$$\alpha - FeOOH_{(s)} + 2H^+ + \frac{1}{2}H_2O_2 \rightarrow Fe^{2+} + \frac{1}{2}O_2 + H_2O \qquad 2\text{-}39$$

Finally hydrogen radicals are generated by Fenton reaction:

$$Fe^{2+} + H_2O_2 \rightarrow Fe^{3+} + OH^- + OH^- \qquad 2\text{-}40$$

The effect of goethite particle size on the oxidation reaction was investigated using four different sizes: 021-0.177 mm, 0.177-0.149 mm, 0.149-0.074 mm and 0.074-0.044 mm. As the particle size of goethite decreased, the rate of oxidation increased. The effect of particle size on the oxidation was significant after 120 min residence time; before 120 min, the effect was negligible (47). It was found that the rate of deactivation of goethite increases at high concentration of goethite due to the higher oxidation rate. Based on Ming-Chun Lu's experiments, Fe^{2+} and Fe^{3+} can improve the efficiency of oxidation in the presence of goethite and hydrogen peroxide better than that in the Fenton system (47).

Based on these previous studies, it may be possible that goethite could act as an oxidation catalyst for heavy oil.

Chapter 3: Experimental

3.1: Materials

3.1.1: Solvents and Vacuum Residue

Athabasca vacuum residue (524 +℃) provided by Suncor was used as the model compound for these experiments. Chung et al. (48) used the SFE (Supercritical Fluid Extraction) method to determine the properties of Athabasca vacuum residue (AVR). it was reported that 60 wt% of the AVR was comprised of small molecules (500-1500 g/mol) and the remainder was bigger molecules including asphaltenes with an average molecular weight of 1500 to 4200 g/mol. Table 3-1 shows all of the specifications of the AVR derived by the SFE method. Toluene was obtained from Fisher Scientific and used as received.

Table 3-1. Characteristics of Athabasca vacuum residue by SFE (48)

Feed	Athabasca vacuum residue
Density, kg/m^3 at 20 ℃	1087
Average molecular weight	1191
Sulfur, wt%	6.5
Nitrogen, ppm	4600
Carbon, wt%	82.7
Hydrogen, wt%	9
H/C (atomic)	1.305
Aromatic carbon wt%	0.41
Nickel, ppm	148
MCR, wt%	26.7
Saturates, wt%	6.3
Aromatics, wt%	33
Resin, wt%	29.4
Asphaltenes, wt%	31.4

3.1.2: Goethite

Goethite is a ferric oxide with the following composition: α-FeO(OH). The goethite used in this work was provided by Aldrich in a powder form (LOT1291343V). Based on the information received from the supplier, this sample contains approximately 35 wt% iron. It has a diameter range between 0.04 to 0.2 mm with molecular weight of 88.85 g/mol, and the density is from 4.6 to 4.0 kg/m^3. The surface area varies from 215 to 195 m^2/g according to the diameter. The following is the molecular structure of goethite:

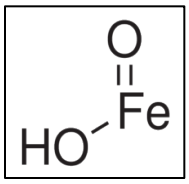

Figure 3-1. Molecular structure of goethite

3.2: Equipment

3.2.1: Thermogravimetric Analysis (TGA)

The TGA was used to heat vacuum residue from room temperature to 700 ℃ using nitrogen and oxygen at various heating rates. TG 409A NETZSCH (Figure 3-2) was used in this project. This TGA can heat the sample up to 1600 ℃ at maximum heating rate of 50 K/min. It has two sample holders, one for the reference pan and the other for the sample pan. The sample was put on an open pan made from Al_2O_3 with a nominal diameter (6.8 mm). The capacity of crucible is 85 μl and the maximum tolerant temperature is around 1650 ℃. The flow rate of purge gas on the sample is 100 ml/min.

Figure 3-2. Thermogravimetric analysis

3.2.2: Rotary Evaporator

A rotary evaporator is used to lower the pressure above a bulk liquid in order to decrease the boiling point of the component liquids in it. In this work, a solution of gas oil and toluene should be extracted. Solvents with a high boiling point such as toluene (110.6 ℃ at standard atmospheric pressure) can be evaporated at lower temperatures if the unit's vacuum system is utilized. A Buchi R-200 rotary was operated at vacuum pressure to extract toluene from the gas oil liquid. This type of evaporator, as shown in Figure 3-3, has a spherical distillation flask to hold the solution; the distillation flask is attached to a motor, which can produce a rotation of 20-280 rpm. A condenser is attached above the flask to recover the vapor produced from the flask. This equipment has a bath with a 4 L volume to heat the sample to the desired temperature; it can work at a temperature ranging from 20 to 180 ℃ with ±2 ℃ accuracy.

Figure 3-3. Rotary evaporator

3.2.3: Sand Bath Agitator and Micro-Reactor

A stainless steel micro-reactor with a 15 ml internal volume, assembled using Swagelok fittings, was used to perform all of the batch reactions. The reactor was connected to 1/4" (ID: 6.35 mm) diameter stainless steel tubing that was terminated with a 6.35 mm stainless steel bonnet noodle valve. The micro-reactor was fixed to the agitating device by a steel plate connected to the valve.

The agitator (Figure 3-4) produces a rotation of 350 rpm, which is attached to a gear by a 6 cm diameter cam. A 2.5 cm diameter, 36 cm long steel rod is attached to a rear end bearing. The rear end bearing is linked to the cam at a 1 cm offset. The minimum length of the reactor tubing to let the micro-reactor be immersed completely in the sand bath is 177.8 mm long.

Figure 3-4. Sand bath agitator

3.2.4: Filtration Glassware

The filtration glassware used in this work, as shown in Figure 3-5, has two flasks. The upper glassware contains the sample including solids, and the lower glassware contains the filtrate after passing through a filter paper. The receiver flask is connected to a vacuum pump to reduce the pressure and allow the liquid pass through the filter paper faster than would occur at ambient conditions. The filter paper used to separate the solids from the liquid is 44 mm diameter, and includes porous holes with 0.22 μm diameter.

Figure 3-5. Filtration glassware

3.3: Procedure

3.3.1: Vacuum Residue Cracking in the TGA

The TGA was run for each reaction with different heating rates and set point temperatures to make a special baseline with empty crucibles. Athabasca vacuum residue was crushed by a small hammer to increase the contact surface area with the crucible. A pure nitrogen (grade#: 4.8, 99.998 purity) cylinder was provided by Praxair Company. The cylinder was attached to the TGA to provide an inert purge gas. The pressure and the flow rate of the purge gas were atmospheric and 100 ml/min above the sample, respectively. After establishing a baseline, different amounts of Athabasca vacuum

residue were weighted and run with the TGA to determine the best sample size with the lowest deviation and error. The manufacturer's recommended amount of sample mass regardless of the type of the sample for the TGA is between 5 to 10 mg. To verify this amount, samples of various sizes (5, 10 and 20 mg) were heated to 700 ℃ ., A concern in thermogravimetry is temperature lag which occurs when the samples do not have enough time to reach thermal equilibrium with the apparatus. Usually, temperature lag occurs only at high heating rates. To investigate the impact of heating rate, 10 mg samples were run at various heating rates (2, 5, 10, 15, 20 and 25 K/min) to compare the amount of mass loss at different heating rates. Eventually, the temperature shown on the screen of the TGA is the actual sample temperature. After cooling the TGA, the crucible containing the reacted sample was put in a furnace to burn the coke, which is produced after the thermal cracking in the TGA. Finally, the heated crucible was washed by toluene to remove all of the particles remaining in.

3.3.2: Cracking and Oxidation of Vacuum Residue in the Closed Reactor

The 10 mg of Athabasca vacuum residue was loaded in the TGA to investigate the effects of the set point temperature and the duration of isothermal oxidation period on cracking kinetics. Samples were heated to 160, 180, 200 and 220 ℃, and at each time they were held for 10and 20 min at the set-point temperatures. In all of these experiments, air at a flow rate of 100 ml/min was used to purge the TGA. The samples were heated to the set-point temperatures at the heating rate of 10 K/min, and maintained for the set-point isothermal period for each holding-time. After the isothermal oxidation period, the purge gas was switched to nitrogen and the sample was cooled. Afterwards, the samples were heated to 700 ℃ with a nitrogen purge gas to determine the mass loss at different extents of pre-oxidation.

In the closed reactor studies, 3.0 g of Athabasca vacuum was accurately weighted in a micro-reactor. The micro-reactor was sealed and pressurized to 1000 kPa with nitrogen, and leak tested. The micro-reactor was then purged by nitrogen five times to 1000 kPa, at room temperature and then sealed at initial reaction pressure, which is 100 kPa in air or nitrogen. To start the reaction, the reactor was attached to the agitator and completely submerged in the sand bath. For pre-oxidation of the residue, reactions were conducted at 180 ℃. The micro-reactor was continuously mixed at reaction temperature for 20 min and then cooled. Afterwards, the sand bath was set at 400 ℃. For experiments using nitrogen in the first stage, the cooled micro-reactor re-heated to 400 ℃ for either 30 or 60 min. For pre-oxidation experiments in which the first stage was purged with air, the cooled reactor was vented and then purged with nitrogen once before re-heating.

The sand bath heater has two parameters which can be manipulated, bed temperature and fluidization rate. The airflow rate needed in the sand bath to ensure a uniform thermal environment is 75 ml/min at 180 ℃. This flow rate must be 45 ml/min when the bed is controlled at 400 ℃. The second set point temperature for cracking has been repeated at three other temperatures such as 420, 430 and 440 ℃ as well.

Catalytic experiments were also conducted using the micro-reactor system. In each case, the initial sample is reacted with 10 wt% goethite. The initial charge to the micro-reactor was 3.0 g of Athabasca vacuum residue and 0.333 g of goethite. Experiments were conducted following the same methods as previously describe for the thermal and pre-oxidation studies.

After the cracking reactions, the reactor was cooled to room temperature using flowing air for 10 min. The reactor was opened, contents emptied and then washed with a brush and toluene. The amount of toluene used to wash the reactor was approximately a 40:1

ratio of toluene to feed. The reactor contents and toluene were transferred into a 250 ml beaker. The walls of the reactor were scraped to remove all of the remaining coke using a steel brush. The washed materials were then mixed in an ultrasonic bath for 15 min to ensure that the whole liquid product was dissolved in the toluene. The coke and catalyst (goethite) were separated from the liquid product (gas oil and toluene) by filtering through a 0.22 μm PVDF filter paper. The remaining solids on the filter paper were washed with toluene until the liquid that passed through the filter paper was clear. The separated solids were then dried in a vacuum oven at 70 ℃ for 12 hours. The amount of the solids, the produced coke and the liquid were calculated using the following equations. The liquid filtrate was separated into toluene and heavy gas oil fractions using rotary evaporator operated at 70 ℃ and 77mbar for 50 min.

$$m_{filter+solids} - m_{filter} = m_{solids} \quad 3\text{-}1$$

$$m_{solids} - m_{goethite} = m_{solids} \quad 3\text{-}2$$

$$m_{liquid+flask} - m_{flask} = m_{liquid} \quad 3\text{-}3$$

Chapter 4: Kinetic Modeling

4.1: Kinetic Modeling of Open Reactor

4.1.1: Overview of Continuous Probability Distribution

Probability distributions are primarily used to predict the possibility of the incidence of a special occurrence. Based on the number of the possible incidences, they can be discrete or continuous functions. In this project, the continuous distributions are applied to predict this possibility. The probability distributions are characterized with parameters to formulate the calculation of the mean, mode, variance, standard deviation and the skewness parameter. They have two major forms: the probability density function (PDF) and the cumulative distribution function (CDF). The PDF is the most generally used form of the probability distributions, and a popular example of this type of function is the classical Gaussian bell. The CDFs generally used to explain the same type of behavior that is shown by a distillation curve (49). Many distribution functions have been used to calculate parameters of importance to the petroleum industry. Whitson et al. (50) suggested a method for the characterization of C_7^+ fraction of petroleum based on a three-parameter γ distribution function. Dhulesia (51) described the ASTM distillation curves of petroleum fractions using the Weibull distribution function; he tested distillation results of the feed and products of a fluid catalytic cracking unit with the Weibull equation. He showed that the obtained curves fitted the experimental results. William and Teja (49) characterized the composition of the mixtures involved during phase equilibrium calculations using the bivariate log-normal distribution function. Characterization of petroleum fractions in state equation calculations has been done by the β distribution function. A family of equations, called "extreme value distributions", has been used in applications that are considering natural phenomena such as rainfall, air

pollution, floods and corrosion. The Gumbel, Frechet and Weibull functions are sometimes described as the members of a single family of extreme value distribution functions that have been communalized. The extreme value distribution functions have one additional parameter to predict the possibility of incidence with a higher precision. Among all distribution functions existing in the literature, the 10 most important functions are shown in Table 4-1 and three of them (Gaussian, Weibull and Gamma) were considered in this project.

Table 4-1. Definition of Continuous Probability distribution Functions, $t = (y - A)/B$ (49)

Distribution	Probability density function (PDF)	Cumulative distribution function (CDF)
1. α (normalized) (C, D)	$\frac{D}{y^2\Phi(C)\sqrt{2\pi}}\exp\left[-\frac{1}{2}\left(C-\frac{D}{y}\right)^2\right]$	$\frac{\Phi\left(C-\frac{D}{y}\right)}{\Phi(C)}$
2. β (A, B, C, D)	$\frac{\Gamma(C+D)}{\Gamma(C)\Gamma(D)(B-A)^{C+D-1}}\frac{(y-A)^{C-1}}{(B-y)^{1-D}}$	$\mathrm{I}(\frac{y-A}{B-A},C,D)$
3. χ (A, B, C)	$\frac{t^{C-1}\exp\left(-\frac{1}{2}t^2\right)}{(2^{(C/2)-1}B)\Gamma\left(\frac{C}{2}\right)}$	$1-\Gamma\left(\frac{C}{2},\frac{1}{2}t^2\right)$
4. Generalized extreme value (A, B, C)	$\frac{1}{B}(1+Ct)^{-1-(1/C)}\exp\left[-(1+Ct)^{-1/C}\right]$	$\exp\left[-(1+Ct)^{-1/C}\right]$
5. Fréchet (A, B, C)	$\frac{C}{B}t^{-C-1}\exp(-t^{-C})$	$\exp(-t^{-C})$
6. γ (A, B, C)	$\frac{1}{B\Gamma(C)}t^{C-1}\exp(-t)$	$\Gamma(C,t)$
7. Log-normal (A, B)	$\frac{1}{By\sqrt{2\pi}}\exp\left[-\frac{1}{2}\left(\frac{\ln(y)-A}{B}\right)^2\right]$	$\Phi\left(\frac{\ln(y)-A}{B}\right)$
8. Normal (A, B)	$\frac{1}{B\sqrt{2\pi}}\exp(-\frac{1}{2}t^2)$	$\Phi(t)$
9. Weibull (A, B, C)	$\frac{C}{B}t^{C-1}\exp(-t^C)$	$1-\exp(-t^C)$
10. Weibull extreme (A, B, C, D)	$\frac{CDt^{C-1}}{B}\exp(-t^C)\left[1-\exp(1-t^C)\right]^{D-}$	$\left[1-\exp(-t^C)\right]^D$

4.1.2: Kinetic Modeling of Vacuum Residue Using Distribution of Activation Energy Model

A simple pseudo-nth-order equation with a single activation energy cannot always be adequate to describe the pyrolysis reactions and the kinetic parameters of complex materials such as coal, oil sand and vacuum residue. A single activation energy for a complex organic or inorganic component does not work over a wide temperature range because only one parameter is used to extrapolate laboratory pyrolysis results to a geological time frame (55). A limitation of using an nth-order rate expression is that it cannot precisely fit the behavior of a complex reaction over a wide spectrum of conversion rates (56).

$$-\frac{1}{\omega_0}\frac{d\omega}{dt} = k\left(\frac{\omega}{\omega_0}\right)^n \qquad 4\text{-}1$$

Where ω is the concentration at time t, ω_0 is the initial concentration, k is the reaction rate coefficient, and n is the reaction order. If there is a single activation energy, it will result in Eqn. 4-2. Integration of Eqn. 4-1 for n=1 and an arbitrary history time gives:

$$\omega = \omega_0 \exp\left[\int_0^t k\,dt\right] \qquad 4\text{-}2$$

or, for $n \neq 1$

$$\omega = \omega_0\left[1-(1-n)\int_0^t k\,dt\right]^{1/(1-n)} \qquad 4\text{-}3$$

As mentioned above, the reactions cannot be sufficiently explained by these simple equations However for the case in which there is a distribution of kinetic parameters, Eqn. 4-2 can be rearranged using distribution function in a time interval. Anthony and Howard (55) have developed Pitt's model to solve this problem. The Anthony and Howard model defines a complex reaction as a number of parallel first-order reactions, in

which each first-order reaction occurs with a specific and individual rate coefficient. To reduce the complexity of the problem, it was assumed that the k_i's differ solely in activation energy and that the number of reactions during a wide temperature range is large enough to permit the E to be described as a continuous distribution function D(E). Eventually integrating Eqn. 4-2 over all energies becomes:

$$\omega = \omega_0 \int_0^{\infty} \exp\left[-\int_0^t k\,dt\right] D(E)\,dE \qquad 4\text{-}4$$

Where

$$\int_0^{\infty} D(E)\,dE = 1 \qquad 4\text{-}5$$

The suitable distribution D(E) is unknown. In this project, the most important distribution functions of describing heavy oil were tried and the three most appropriate ones were identified. By differentiation of Eqn. 4-4 with respect to time, the rate of reaction becomes:

$$-\frac{d\omega}{dt} = \omega_0 \int_0^t k \exp\left[-\int_0^t k\,dt\right] D(E)dE \qquad 4\text{-}6$$

In this work ω_0=1 (because it is similar to the initial concentration before reaction), and the integral limits for the above equation were set at $E_0 \pm 3\sigma_E$ to cover 99.7% of the reaction set. The number of reaction steps varies based on the heating rate, at the higher heating rates the number of energy spaces (first-order reaction steps) are less and at the lower heating rates the number of energy spaces is higher. For evaluation of a time integral I_t in Eqn. 4-6:

$$I_t = \int_0^t k\,dt \qquad 4\text{-}7$$

The Arrhenius form is assumed for the reaction rate coefficient:

$$k = A\exp\left(-E/RT\right) \tag{4-8}$$

Where E is the activation energy, A is the frequency factor, R is the ideal gas constant and T is the absolute temperature. At each of the discrete energy intervals that are investigated in a distribution of activation energy, the time integral has to be evaluated. *I* is usually approximated by the following equation at a constant heating rate (H_r) (55):

$$I_t \approx \frac{ART^2}{H_r}\exp\left(-E/RT\right) \tag{4-9}$$

There are several important conditions that are required for the validation of the above equation: the presence of a constant heating rate, a high value of E/RT, and a primary (or ultimate) T that is low enough where a short reaction occurs. To solve this problem, Eqn. 4-7 is capable to be numerically integrated for an arbitrary temperature history:

$$\Delta I_i = \int_{t_{i-1}}^{t_i} A\exp\left(-E/RT\right)dt \tag{4-10}$$

By using a logical approximation for the exponential integral (57) and linear interpolation of T between t_{i-1} and t_i, ΔI_i can be calculated as:

$$\Delta I_i \approx \left(\frac{t_i - t_{i-1}}{T_i - T_{i-1}}\right)\left\{\begin{array}{l} T_i A\exp\left(-E/RT_i\right)\times\left[1-\dfrac{\left(E/RT_i\right)^2 + a_1\left(E/RT_i\right)+a_2}{\left(E/RT_i\right)^2 + b_1\left(E/RT_i\right)+b_2}\right] - T_{i-1}A\times \\ \exp\left(-E/RT_{i-1}\right)\times\left[1-\dfrac{\left(E/RT_{i-1}\right)^2 + a_1\left(E/RT_{i-1}\right)+a_2}{\left(E/RT_{i-1}\right)^2 + b_1\left(E/RT_{i-1}\right)+b_2}\right] \end{array}\right\} \tag{4-11}$$

Where $a_1 = 2.334733$, $a_2 = 0.250621$, $b_1 = 3.3305657$, and $b_2 = 1.681534$. If T is constant or the difference between T_i and T_{i-1} is sufficiently low then:

$$\Delta I_i = A\exp\left(-E/RT\right)(t_i - t_{i-1}) \qquad 4\text{-}12$$

The value of the frequency factor can be obtained by using the Braun and Burnham equation (54). Mass loss data collected at different heating rates can be employed to calculate an approximate value of A.

$$\ln\left(\frac{H}{T_{\max}^2}\right) = -\frac{E_0}{RT_{\max}} + \ln\left(\frac{AR}{E_0}\right) \qquad 4\text{-}13$$

A straight line result from the plot of $\ln\left(H/T_{\max}^2\right)$ versus $1/T_{\max}$ with a slope of $-E_0/R$ and an intercept of $\ln\left(AR/E_0\right)$ is expected. Therefore, for different heating rates the values can be calculated.

In this work, three of the distribution functions were considered, Gaussian, Weibull and Gamma. The Gaussian distribution function with a mean activation energy, E_0, and a standard deviation σ_E is described by the following equation, 4-14:

$$D(E) = \frac{1}{\sigma_E\sqrt{2\pi}}\exp\left[-\frac{\left(E - E_0\right)^2}{2\sigma_E^2}\right] \qquad 4\text{-}14$$

The Weibull distribution function with mean activation energy, E_0, a scale parameter B and shape parameter C is described by the following equation, Eqn. 4-15:

$$D(E) = \frac{C}{B}\left(\frac{E - A}{B}\right)^{C-1}\exp\left[\left(\frac{E - A}{B}\right)^{C}\right] \qquad 4\text{-}15$$

The relation of parameters in the Weibull distribution function is as follows:

$$E_0 = B\Gamma\left(1+\frac{1}{C}\right) \tag{4-16}$$

and

$$Variance = B^2\left[\Gamma\left(1+\frac{2}{C}\right)-\left(\Gamma\left(1+\frac{1}{C}\right)\right)^2\right] \tag{4-17}$$

The values of B and C are always positive, and the value of C for a bell shape figure is between 1 to 10. A MATLAB program was written to fit the distribution functions to the experimental data. Using an initial guess for the fitting parameters, the MATLAB program was run to obtain optimized values of A, B and C for each data set. The Gamma distribution function with shape parameter B, scale parameter C and shift parameter A is presented in the following equation, Eqn. 4-18:

$$D(E) = \frac{1}{B\Gamma(C)}\left(\frac{E-A}{B}\right)^{C-1}\exp\left(-\frac{E-A}{B}\right) \tag{4-18}$$

The relation of parameters for Gamma distribution function is as follows:

$$E_0 = B\times C \tag{4-19}$$

and

$$Variance = C\times B^2 \tag{4-20}$$

The values of B and C for the Gamma distribution function are always positive, so based on the above relations, the Gamma distribution can be rearranged as:

$$D(E) = \frac{C}{E_0\Gamma(C)}\left(\frac{E-A}{E_0/C}\right)^{C-1}\exp\left(-\frac{E-A}{E_0/C}\right) \tag{4-21}$$

With the above transformation, the number of unknown parameters was reduced from 3 to 2.

Eventually, by putting the above distribution functions in Eqn. 4-6, and fitting the left and right hand sides of this equation by running the MATLAB program (MATLAB codes can be found in the Appendix), the values of the mean activation energy and standard deviation for each function were determined

4.1.3: Optimization of Kinetic Parameters and Selection the Best Distribution Function

A genetic (algorithm) optimization method was used to obtain the optimal set of parameters for the probability distribution functions. The minimization of the residual sum of square (RSS) was applied for the optimization criterion, which is defined by Eqn. 4-21:

$$RSS = \sum (y_{\exp,i} - y_{cal,i})^2 \qquad 4\text{-}21$$

Where $y_{exp,I}$ and $y_{cal,I}$ are the experimental and predicted weight fraction with respect to time, respectively.

In a genetic algorithm, a population of candidate solutions, which are called individuals, is randomly varied to generate an optimum solution. Each candidate solution is like a package with a set of traits, which can be modified during the optimization process. A population of randomly generated individuals creates a discrete evolution and which is described as a generation. The fitness of every individual is measured in each generation, the individuals that make a better fit is selected from the current population and the other individuals are altered to form a new population; and the new population is utilized in the next iteration of genetic algorithm. Generally the algorithm is terminated when either a maximum number of generations have been produced or the fitness level has been

reached a desired value (58). The block diagram of optimization method can be plotted as follows:

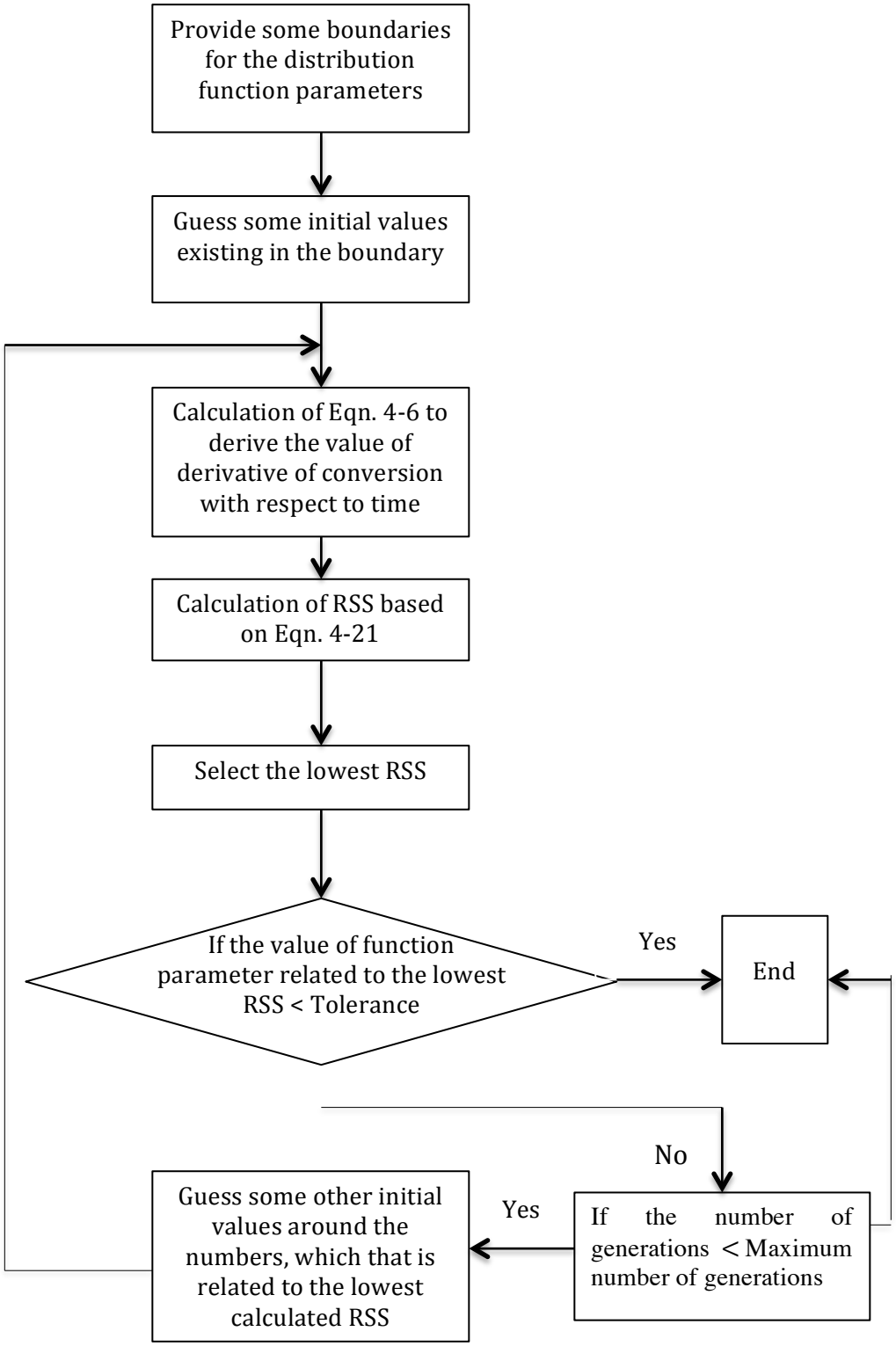

Figure 4-1. Schematic of the genetic optimization method indicating the calculation steps

The comparison of the various functions and their ability to fit the data were described based on their statistical indicators. At first, the main criterion to determine the best function is standard deviation as calculated by Eqn. 4-22:

$$SD = \sqrt{\frac{RSS}{n-2}} \qquad 4\text{-}22$$

The other basic methods used to determine the best distribution function are the correlation coefficient (R^2) and, slope, and intercept.

Selection of the best model to explain a given data set should never be based only on goodness of fit or R^2. It is well known that goodness of fit can usually be improved by increasing the number of free parameters, but on the other hand this improved fit is associated with a reduction in the confidence of the model parameter estimates. As a result, using standard deviation data to rank the models with different numbers of parameters may not be sufficiently acceptable. Another type of approach used to compare the fit of the distribution functions is the Akaike and Bayesian information criteria (AIC and BIC, respectively). The number evaluates the complexity of a model and how fine it correlates and fits the data (59). The AIC methodology can be used to identify the model and function that best describes the data with a minimum number of free parameters. The formula for calculation of the AIC is given by (55):

$$AIC = 2k + n\ln\left(\frac{RSS}{n}\right) \qquad 4\text{-}23$$

Where n is the number of observation in each experiment, k is the number of parameters and RSS is the residual sum of square. AIC contains a penalty term (2k), according to this term; this criterion is highly beneficial to compare different models with various numbers of parameters. In this case, the model with the lowest AIC value best balances the

goodness of fit of the model with the magnitude of the confidence interval associated with each estimated parameter (56). The following equation is the expression to calculate the Bayesian information criterion for distribution models with RSS:

$$BIC = k\ln(n) + n\ln\left(\frac{RSS}{n}\right) \qquad 4\text{-}24$$

The procedure for employing the BIC is similar as that for using the AIC; the preferred model is referred to the one having the lowest BIC value. AIC is highly dependent on sample size; therefore it is recommended to use comparative values like the AIC differences (Δ_i) among various models to select the best fitting model. Those models with $\Delta_i > 10$ should be omitted due to a significant variation in the data (55).

$$\Delta_i = AIC_i - AIC_{\min} \qquad 4\text{-}25$$

4.2: Kinetic Modeling of Closed Reactor

4.2.1: Selection of a Multi-lump Model

In this project, first, four types of products were assumed after batch reaction in the mirco-reactor. These products can be characterized for modeling purposes as belonging to four lumps; gas product (IBP-150 ℃), light and heavy gas oil or liquid product (150-426 ℃), Resid (+426℃) and Coke. The schematic of the batch reaction in the micro-reactor based on four lump model is illustrated in Figure 4-2:

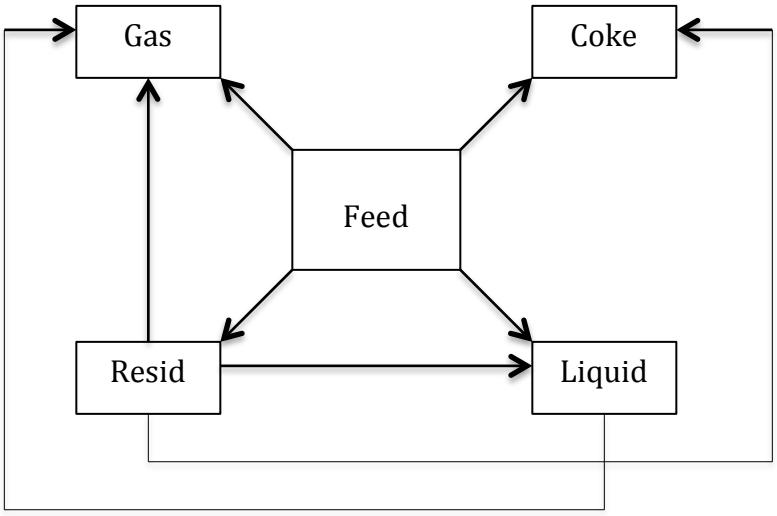

Figure 4-2. Schematic of reaction network in a closed reactor for heavy oil

In the above reaction network, the filtrated solid product of the reaction has been divided into two separate products (Coke and Resid). The Coke and resid cannot produce any lighter products in this model but the Resid can potentially produce lighter products at high temperature ranges. This detailed network reaction has a high precise view on the procedure of the reaction. But, because of some constraints on the obtained product conversions in the laboratory and the complexity of many equations in the network reaction, the Coke and Resid lumps come into a new single lump. This new lump is exactly the same as the solid (including coke and asphaltenes) which is filtrated after the reaction. With respect to the transformation from the first reaction network to the second one, the initial conditions of the new three lump model is explained as Eqn. 4-26. This model can be simplified to a new three lump model as follows in Figure 4-3:

[Feed]=1

[Coke + Resid] or [C+R]=1

[Liquid]=0

[Gas]=0

Where

[Coke]=[C+R] – [Resid]

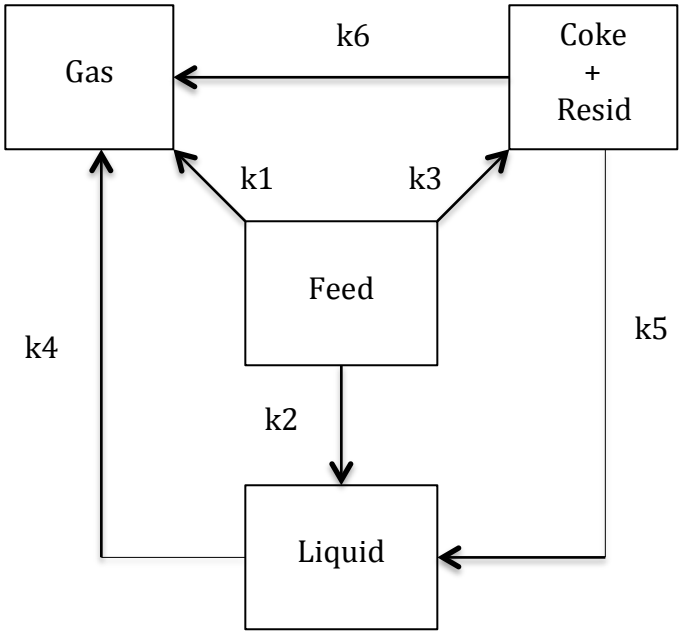

Figure 4-3. Schematic of reaction network based on three lump model in a closed reactor for heavy oil

The above reaction network was used to calculate the six kinetic parameters. The value of k6 in this model is very low compared to the other values of k_i because the reaction of k6 needs a very high temperature to occur. Therefore, in this model, k6 was omitted to simplify the network to the following Figure 4-4:

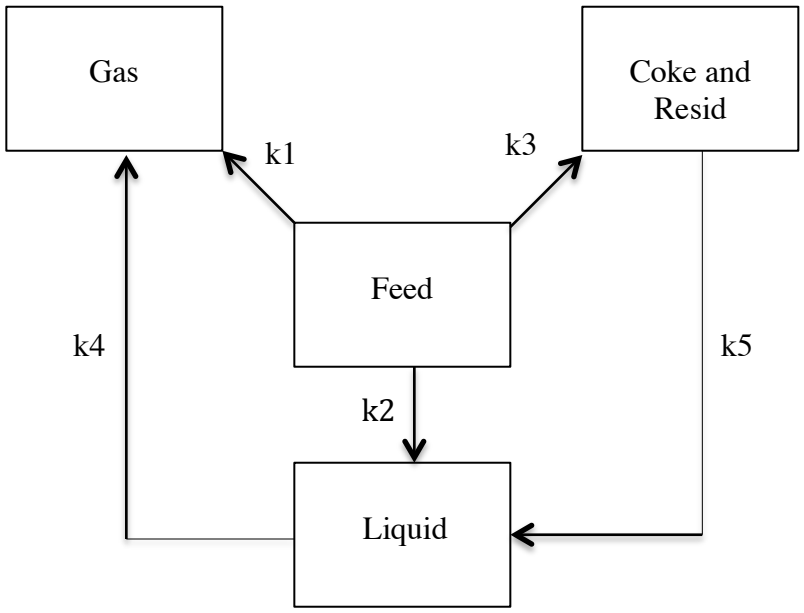

Figure 4-4. Schematic of simplified reaction network in a closed reactor for heavy oil

Based on the simplified model, the results did not change a lot. This small change showed that the ignorance of k6 was reasonable, and it even made better statistical numbers for results.

4.2.2: Mathematical Development of Model

In the three lump model, all the reactions and conversions were hypothesized to be based on first-order reaction kinetics. The kinetic equations for the reaction network can be presented as follows:

$$\frac{dF}{dt} = -(k_1 + k_2 + k_3)[F] \qquad 4\text{-}26$$

$$\frac{d[C+R]}{dt} = k_3[F] - k_5[C+R] \qquad 4\text{-}27$$

$$\frac{d[Liquid]}{dt} = k_2[F] + k_5[C+R] - k_4[Liquid] \quad 4\text{-}28$$

$$\frac{d[Gas]}{dt} = k_1[F] + k_4[Liquid] \quad 4\text{-}29$$

Initial conditions

At t=0, [F]=F_0, [C+R]=1, [Liquid]=[Gas]=0.

The square brackets in the rate equations represent the weight fraction of the different fractions at time t. The mentioned equations are homogeneous differential equations and can be solved by the mentioned initial conditions. For a first order homogenous differential equation which is defined as:

$$\frac{dy}{dx} + p(x) = q(x) \quad 4\text{-}30$$

By using a variable change as presented below:

$$u = \exp\left(\int p(x)\,dx\right) \quad 4\text{-}31$$

The solution will be as follows:

$$y = \frac{\int u(x)q(x)\,dx + c}{u(x)} \quad 4\text{-}32$$

The above rate equations can be solved according to the mentioned mathematical solution of the first order homogenous differential equation. The final equations of weight fraction of the products are as follows:

If

$$k_A = k_1 + k_2 + k_3 \quad 4\text{-}33$$

then

$$[F] = F_0 \exp(-k_A t) \tag{4-34}$$

$$[C+R] = \frac{F_0 k_2}{k_5 - k_A}[\exp(-k_A t) - \exp(-k_5 t)] \tag{4-35}$$

$$\begin{aligned}[Liquid] = {} & \frac{F_0 k_1}{k_4 - k_A}\left[\exp(-k_A t) - \exp(-k_4 t)\right] + \frac{F_0 k_2 k_5}{(k_5 - k_A)(k_4 - k_A)} \\ & \left[\exp(-k_A t) - \exp(-k_4 t)\right] - \frac{F_0 k_2 k_5}{(k_5 - k_A)(k_4 - k_A)}\left[\exp(-k_5 t) - \exp(-k_4 t)\right]\end{aligned} \tag{4-36}$$

$$\begin{aligned}[Gas] = {} & \frac{F_0 k_3}{k_A}\left[1 - \exp(-k_A t)\right] + \frac{F_0 k_1 k_4}{(k_4 - k_A)k_A}\left[1 - \exp(-k_A t)\right] - \frac{F_0 k_1}{(k_4 - k_A)} \\ & \left[1 - \exp(-k_4 t)\right] + \frac{F_0 k_2 k_4 k_5}{(k_5 - k_A)(k_4 - k_A)k_A}\left[1 - \exp(-k_A t)\right] - \frac{F_0 k_2 k_5}{(k_5 - k_A)(k_4 - k_A)} \\ & \left[1 - \exp(-k_4 t)\right] + \frac{F_0 k_2 k_4 k_5}{(k_5 - k_A)(k_4 - k_5)k_5}\left[1 - \exp(-k_5 t)\right]\end{aligned} \tag{4-37}$$

All the above equations have been written in MATLAB programming (Appendix B) to optimize and calculate the kinetic parameters.

4.2.3: Estimation of Reaction Constants

All of the kinetic equations for three lumps were written in MATLAB software for estimation and optimization of parameters including k_1 through k_5. The genetic algorithm was used to optimize the parameters with the lowest error. As shown below, the sum of the fractional errors E_f in the parameter optimization method was minimized based on the Eqn. 4-38:

$$E_f = \sum_i \frac{\left|(Y_i^{\exp} - Y_i^{cal})\right|}{Y_i^{cal}} \qquad 4\text{-}38$$

Where $Y_i^{\exp}$ and Y_i^{cal} are the experimental and calculated values of the product yield. Optimization of the sum of squares of the errors was also used, but the minimization of E_f had a better result with a lower error.

Chapter 5: Results and Discussion

5.1: Why do we care about the Activation Energy?

Accurate estimates of kinetic parameters of heavy oil thermal cracking are required for the design, optimization and development of processes related to heavy oil upgrading. Each analytical tool available for measuring the chemical kinetics in a laboratory setting has a unique reaction path. A variety of methods are available in the published literature that can be used to analyze the resulting data. In this project, the Arrhenius parameters will be compared to a closed reactor studies operation in an isothermal mode with data from open reactor studies operated in a non-isothermal mode. Closed reactor studies involve time-consuming experiments in the laboratory but isothermal data analysis is relatively straightforward. Conversely, open reactor studies using a TGA are relatively quick but data analysis is more complicated due to the non-isothermal operating regime. In TGA, the determination of an appropriate value of the heating rate is one of the big concerns in running a non-isothermal process correctly. Several analytical methods are also available for the calculation of the activation energy that best fits the non-isothermal analytical rate data. For Athabasca vacuum residue, a reliable method is needed to rapidly determine the best Arrhenius parameters for thermal cracking. Therefore, in this study, different ways for calculating activation energy of heavy oil cracking were tested to select the best method to verify the validation of the heating rate and the procedure to estimate the kinetic parameters. In this method, one kinetic parameter is only calculated for the sample, including the heat value that is needed for evaporation and the thermal cracking reaction. The work by Olmstead et al. (22) showed that the weight loss at higher than 390 ℃ is mostly chemically reacting; Thus, the calculated numbers of kinetic parameters mainly imply the chemical reactions. A flame ionization detector may be used to detect

the produced gas downstream of the TGA to determine, for future studies, the boundary between evaporation and the chemical reaction.

5.2: Closed reactor – isothermal operation

This approach is good as long as the heating time to reaction temperature is short compared to the total time it takes for the reaction to be completed. Closed reactor always takes a while to attain the operation temperature; this period should be short compared to the total isothermal reaction time to cover the deviation of the reaction at the beginning of the isothermal time. As the temperature of an isothermal operation increases, the duration of this isothermal reaction should be longer to make the data more reliable for the Arrhenius equation. In this method, the experiments must be run at different isothermal temperatures and times to provide sufficient data for the Arrhenius equation to calculate the kinetic parameters. As it was mentioned, all of these tests are time-consuming, but it is worth the time; the final results are reliable because the derived results involve the behavior of the respective sample at different conditions including time and temperature. Jazvinder Singh et al (60) have considered the reaction of vacuum residue in a closed reactor and modeled the feed and the products in a five-lump model. They defined four products such as gas (-C_5), gasoline (IBP-150 ℃), light gas oil (150-350 ℃) and vacuum gas oil (350-500 ℃). All of the reactions in their model were assumed to be first-order reactions from the feed to the products, and the derived activation energies of these reactions were obtained as follows:

Table 5-1. The derived activation energies for proposed reaction network (60)

Product	Activation Energy* (kJ/mol)	Pre-exponential factor* (1/min)
Gas	194.69	1.41E+12
Gasoline	494.79	2.45E+34
Light gas oil	202.52	2.32E+13
Vacuum gas oil	157.34	1.33E+10

* Five-lump model

In this project, a three lump model with a slight similarity to the previously mentioned reaction network was utilized to model the thermal cracking of Athabasca vacuum residue in a closed reactor with and without a catalyst.

5.3: Open Reactor – Non-isothermal operation

5.3.1: The Simplest Way to Calculate the Kinetic Parameters

It is generally accepted that thermal cracking of petroleum residues will follow a first-order reaction expression. With respect to the above assumption and the mentioned mathematical equations, in chapter two, the activation energy and pre-exponential factor can be obtained with slope and intercept of the line, respectively. Figure 5-1 shows the trend of this line at 10 K/min. As is illustrated below, this line is derived by the plot of $\ln[(dX/dT)/(1-X)]$ versus $1/T$ for thermal cracking.

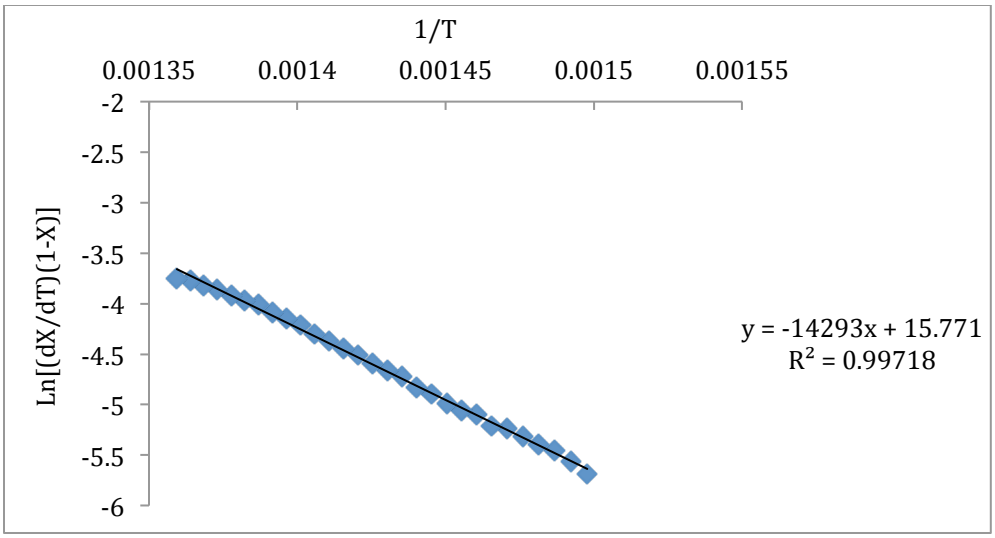

Figure 5-1 Plot of ln[(dX/dT)/(1−X)] versus 1/T for thermal cracking of the AVR at 10K/min

The following table shows the values of kinetic parameters and the coefficient of determination based on this assumption:

Table 5-2. The obtained kinetic parameters based on the first-order reaction

Heating Rate (K/min)	E* (kJ/mol)	A* (min^{-1})	R^2
0.5	90.49	9.7E+4	0.994
2	101.1	1.5E+6	0.988
5	110.7	1.2E+7	0.994
10	118.8	7.1E+7	0.997
15	119.1	8.4E+7	0.994
20	126.1	3.0E+8	0.997
25	126.4	3.4E+8	0.990
35	139.4	3.3E+9	0.995

* Simple first-order reaction method was used to calculate the parameters

The following table shows the temperature range of weight loss during the thermal cracking reactions at each heating rate. These ranges were used to linearize the kinetic parameters with respect to the conversion of the sample.

Table 5-3. Temperature range of first-order reaction at each heating rate

Heating Rate (K/min)	Temperature Range (℃)
0.5	380 - 402
2	381 - 437
5	381 - 453
10	394 - 462
15	381 - 477
20	382 - 477
25	385 - 480
35	389 - 480

The obtained kinetic parameters determine that the first assumption (first-order reaction) is not qualified to explain the behavior of Athabasca vacuum residue. Comparison of the kinetic parameter values with the derived values of vacuum residue in the literature indicates a big difference between these two numbers. Ho Young Park (1) obtained the activation energy 239.82 kJ/mol for vacuum residue; as a result, the above-calculated values are not reliable based on the first-order reaction.

In addition to the aforementioned method, another method was tested to derive the parameters; Chen-Nuttal has been used in several articles to derive the kinetic parameters. In this technique, a first-order reaction is assumed for the thermal cracking of vacuum residue, but as was explained in chapter two, the approach is different from that of the previous method. The following table shows the final results after the trial and error technique in this method.

Table 5-4. The obtained kinetic parameters from Chen-Nuttal method

Heating Rate (K/min)	First guess for E(kJ/mol)	Second Answer E (kJ/mol)	Final Answer E (kJ/mol)	A (min^{-1})
0.5	90.00	89.34	89.35	8.4E+4
2	90.00	93.01	93.00	3.8E+5
5	90.00	96.53	96.48	1.1E+6
10	100.0	98.12	98.15	2.1E+6
15	100.0	105.3	105.2	7.9E+6
20	100.0	111.6	111.5	2.7E+7
25	100.0	104.4	104.4	8.3E+7
35	100.0	113.8	113.7	4.7E+7

* Chen Nuttal Method

As shown in Table 5-4, the final results have a significant error compared to the literature review results. Furthermore, the Chen-Nuttal method works even worse than the previous method. With respect to Figure 5-2, another negative point of both methods is cleared when a percentage of the temperature range of a thermal cracking reaction is cut to linearize the correlation. In fact, the temperature ranges mentioned in Table 5-3 do not represent the entire range of the cracking reaction at each heating rate, so although this method works for some samples, it can't be used for Athabasca vacuum residue. In the next section, the obtained results from the distribution method are presented in a new way.

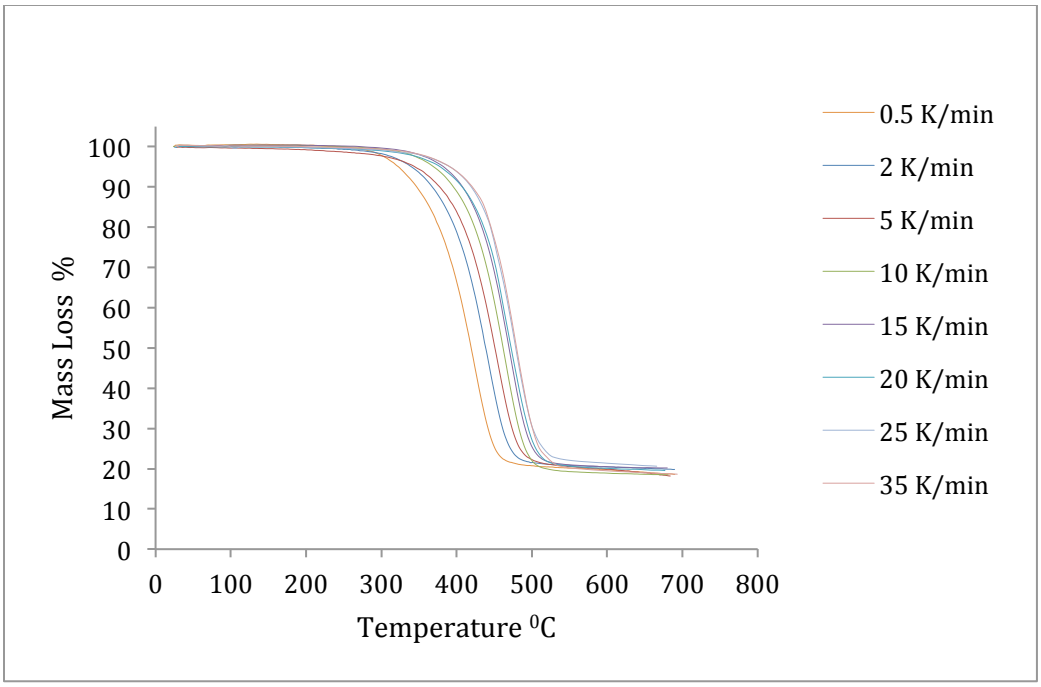

Figure 5-2. Mass loss curves of Athabasca vacuum residue at different heating rates

Furthermore, there is one more thing about the TGA data and that is the reliability. In order to have accurate data, it is necessary to repeat each experiment at least two times with the TGA to obtain the same results. If the results are different, the experiment must be repeated until the TGA must yield reliable results. In this section of this project each test with the TGA was repeated at least twice. The following figure shows that two data series confirm the accuracy of the TGA data for mass loss versus temperature at 10 K/min.

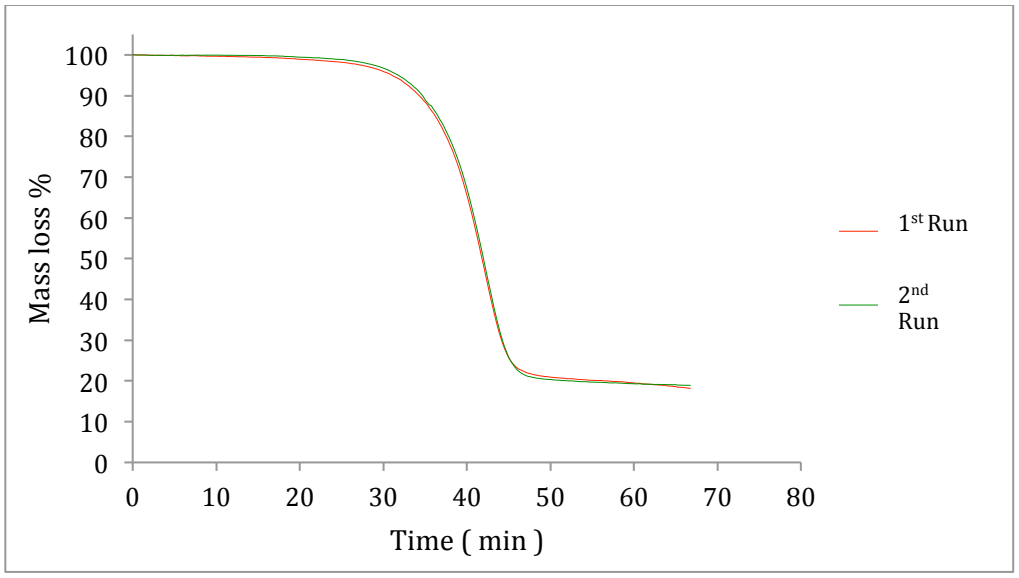

Figure 5-3. Repetition of the TGA run shows a good consistency at 10 K/min

Some TGA data had a minor deviation from each other; in these cases the experiment was repeated four times to obtain reasonable data with a good average and deviation. One of the tests that was repeated for four times had been run at 2 K/min. The following figure shows the repetition of this test and indicates the deviation in its results.

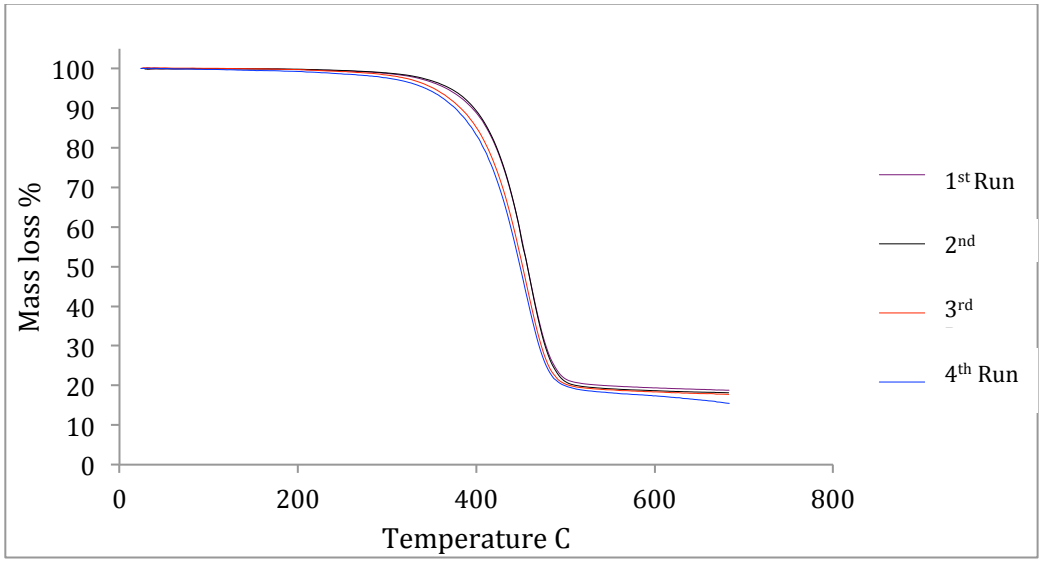

Figure 5-4. Repetition of the TGA run for four times at 2 K/min

As Figure 5-4 indicates, the lack of consistency in the data means that the experiments must be repeated more times than what is shown in Figure 5-3. As a result, the four data series at 2 K/min deviated slightly from each other.

5.3.2: Comparison of Distribution Functions in an Open Reactor:

Three main distribution functions were selected based on the work by Sergio (49). Gaussian, Weibull and Gamma are the most common functions used to fit the experimental and modeling results together for Athabasca vacuum residue. Based on the Anthony Howard method explained in chapter four, in the following equation the left-hand side is determined by the experimental results, that is, the derivative of concentration with respect to time. The right-hand side is modeled with the mentioned distribution functions to be equal to the left hand side at each time step.

$$-\frac{d\omega}{dt} = \omega_0 \int_0^t k \exp\left[-\int_0^t k\,dt\right] D(E)dE \qquad 5\text{-}1$$

However, prior to developing the above equation in MATLAB programming software, the experimental results were tested with ten different distribution functions without the kinetic part of Eqn. 5-1. This was carried out in order to verify whether or not the functions are capable of fitting data. The distribution functions were solely fitted with the experimental data by EasyFit software, and the functions were selected as the best options to establish the model. MATLAB software (Appendix A-1) was used to calculate the right-hand side of the above equation. Furthermore, three different heating rates, 0.5, 10 and 25 K/min, were used for each distribution function to determine the appropriate heating rate that would provide the best fit for the experimental results. In addition, the temperature ranges at three heating rates of 0.5, 10 and 25 K/min were separated into 59, 65 and 29 first-order reaction steps for each distribution function. These steps are based

on the points derived from the TGA data between the initial and final temperatures. The temperature range considered when fitting the experimental and modeling results at 0.5 K/min was between 569.9 K and 710.6 K; the main reaction at this heating rate occurred within this range. The temperature ranges at heating rates of 10 and 25 K/min were between 612.5 K to 769.5 K, and 625.7 K to 802.7 K, respectively. As mentioned, as the heating rate increases, the range of reaction temperatures is elevated to a higher magnitude. The reason for this behavior is explained by a temperature difference between the furnace and sample. As the heating rate increases, the temperature increases more quickly for the TGA furnace, so the sample cannot attain the furnace temperature; this is a common problem with the TGA. This project investigates and shows the effect of this problem on calculating kinetic parameters of the reaction.

The Gaussian function was the first distribution function utilized to model the reaction. Eventually, rearranging Eqn. 4-14 in Eqn. 4-6 and using a linear interpolation of Eqn. 4-11 results in Eqn. 5-2. The following equation is solely related to one temperature step between the i-th and (i+1)-th steps. With respect to the MATLAB code in appendix A-1, the following equation is repeatedly calculated, in a loop, for the whole range of temperatures.

$$\left(\frac{d\omega}{dt}\right)_{i,calc} = A\exp(-\frac{E}{RT_i})\exp(\Delta I_i)\left(\frac{1}{\sigma_E\sqrt{2\pi}}\right)\exp\left(-\frac{(E-E_0)^2}{2\sigma_E^2}\right) \qquad 5\text{-}2$$

The Genetic optimization method was used to fit together the experimental and calculated results. Prior to starting to use the genetic method, fmincon optimization method was a popular method to solve these types of problems; it was used to converge the experimental and modeling results. However, this method could not have acceptably optimized the function parameters. Therefore the genetic method was replaced as a

stronger algorithm to develop the distribution method. Lower bound and upper bound were defined in this method to use as initial guesses to start the optimization process. The population size for the optimization was 3000 individuals and the maximum number of generations allowable was set at 10000 with a tolerance for the solution of 1×10^{-100}. Equation 5-2 was integrated with the activation energy steps to calculate the derivative of conversion with respect to time for the whole period of the reaction, and the Gaussian distribution of results was obtained. The interval of activation energy was set between zeros to 400000 J/mol. The pre-exponential factor is the only thing that is unknown in the above equation. In the Anthony Howard method it is assumed that this factor is constant during the reaction. This factor can be calculated by the Braun and Burnham (54) equation mentioned in chapter four. To use this equation, the thermal cracking of vacuum residue was run at nine different heating rates to calculate the pre-exponential factor. The plot of $\ln\left(H/T_{\max}^2\right)$ versus $1/T_{\max}$ with a slope of $-E_0/R$ and an intercept of $\ln\left(AR/E_0\right)$ results in this factor. As Figure 5-5 illustrates, there is a linear line, which confirms the pre-exponential factor's accuracy.

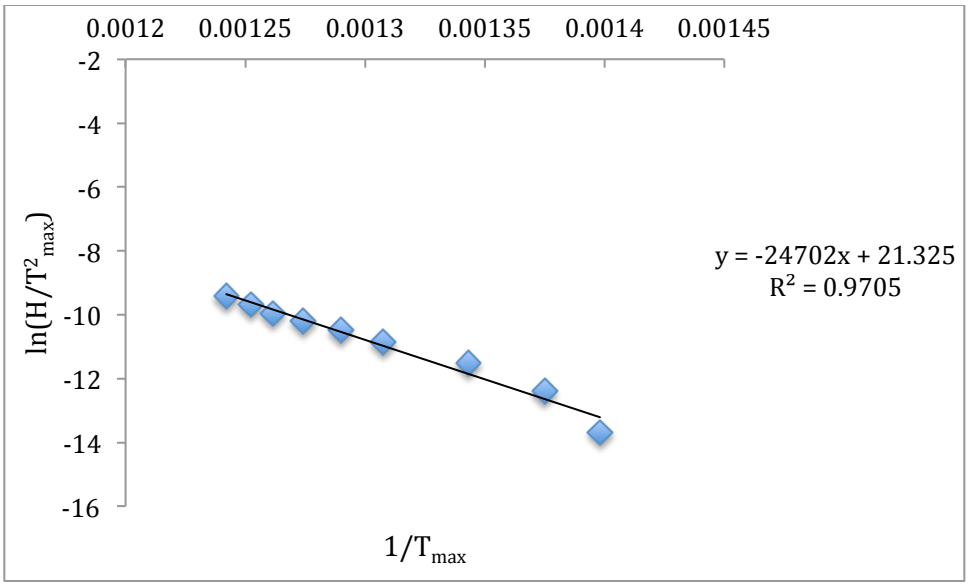

Figure 5-5. Regression for the nine points at nine various heating rates

As shown in the above figure, the last point has caused a little deviation compared to the other points. So, this point was deleted and another figure was drawn without the last point to compare the results. Figure 5-6 shows a better regression than Figure 5-5.

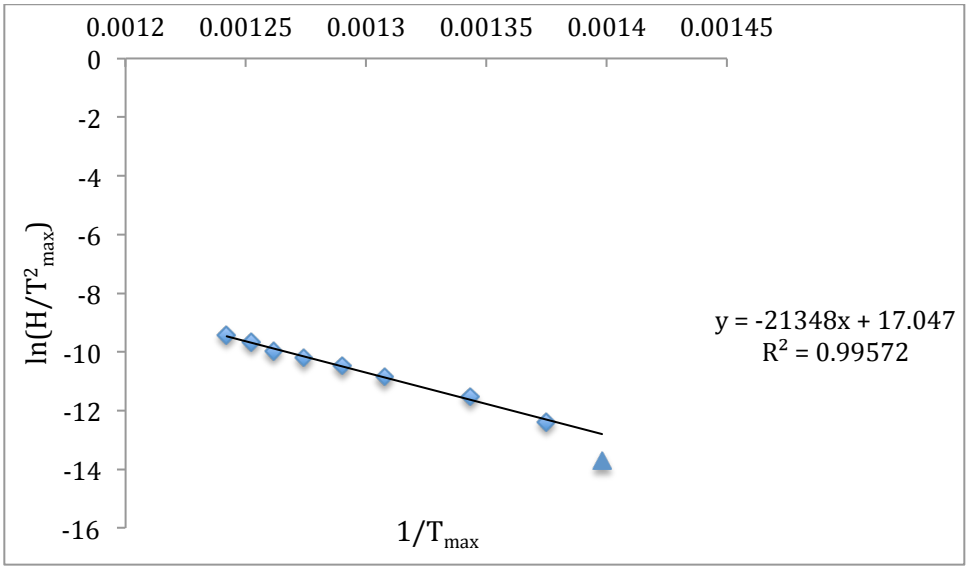

Table 5-6. Regression for the eight points at eight various heating rates

PolyMath software was used to do a statistical analysis. Table 5-5 and Table 5-6 compare the statistical coefficients of these two figures.

Statistics

Table 5-5. Statistical coefficients for Figure 5-5

R^2	0.97
Adjusted R^2	0.96
Rmsd (Root-mean-square deviation)	0.075
Variance	0.066

Statistics

Table 5-6. Statistical coefficients for Figure 5-6

R^2	0.99
Adjusted R^2	0.99
Rmsd (Root-mean-square deviation)	0.021
Variance	0.049

Using this method results in the amount of pre-exponential factors, and the mean activation energies with 95% confidence interval shown in Table 5-7 and Table 5-8 as an initial guess to start optimizing the calculation of standard deviation.

Table 5-7. Kinetic parameters derived from Braun and Burnham equation for nine points

Pre-exponential factor (1/s)	Mean activation energy (kJ/mol)
1.1 E+11 ± 7.2 E+6	205.4 ± 32.1

Table 5-8. Kinetic parameters derived from Braun and Burnham equation for eight points

Pre-exponential factor (1/s)	Mean activation energy (kJ/mol)
1.5 E+9 ± 1.2 E+7	177.487 ± 11.6

Based on the above tables, there is not a major difference between statistical coefficients. Furthermore, the adjusted determination coefficient is not too much less than R^2, so both of the figures are reliable to calculate the kinetic parameters. On the other hand, the value of pre-exponential factor (A) in this step is used in the distribution method to calculate the activation energy, but these two different numbers for A have a really small and negligible effect on the value of obtained activation energy in the distribution method. As a result, the obtained activation energy for both of the A values is around 220 kJ/mol, which is closer to the obtained mean activation energy in the Braun and Burnham method at nine different heating rates. Therefore, not only does the last point in the nine-point figure not make an error, it also corrects the slope of the line to derive a better value for the pre-exponential factor and activation energy. Eventually, the values of Table 5-7 were used in the distribution method to fit the experimental and modeling results with each other.

The fitness of experimental and calculated results is illustrated in the following figures, which were obtained after running the MATLAB.

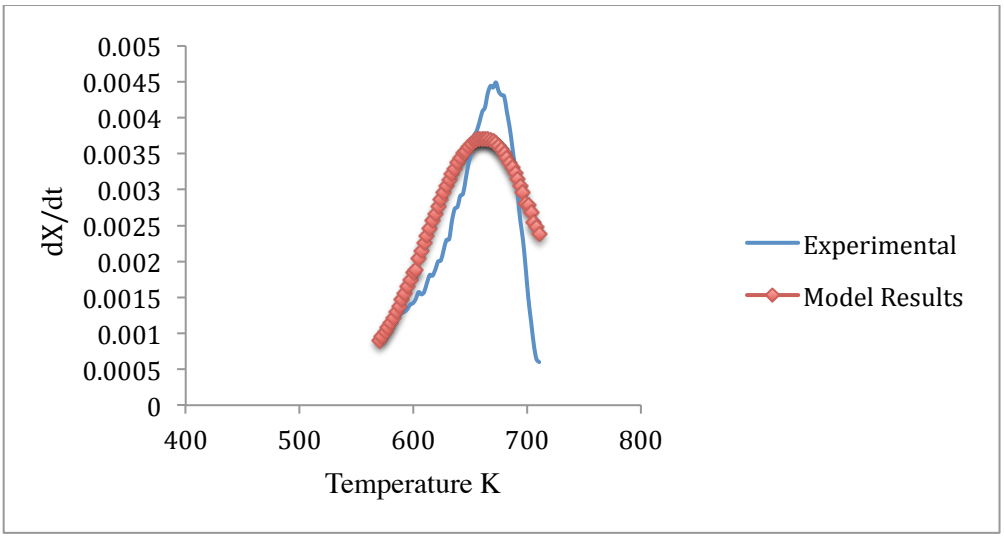

Figure 5-7. Comparison of experimental and Gaussian model results at 0.5 K/min

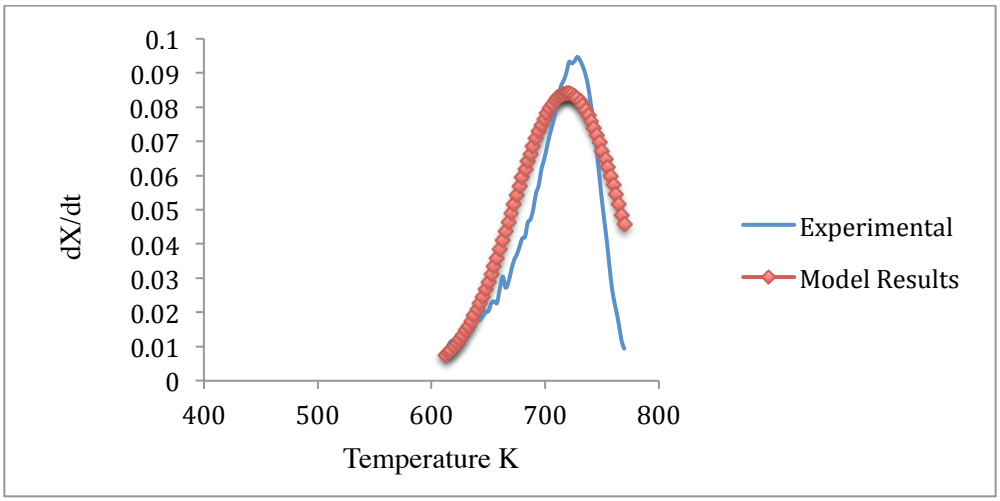

Figure 5-8. Comparison of experimental and Gaussian model results at 10 K/min

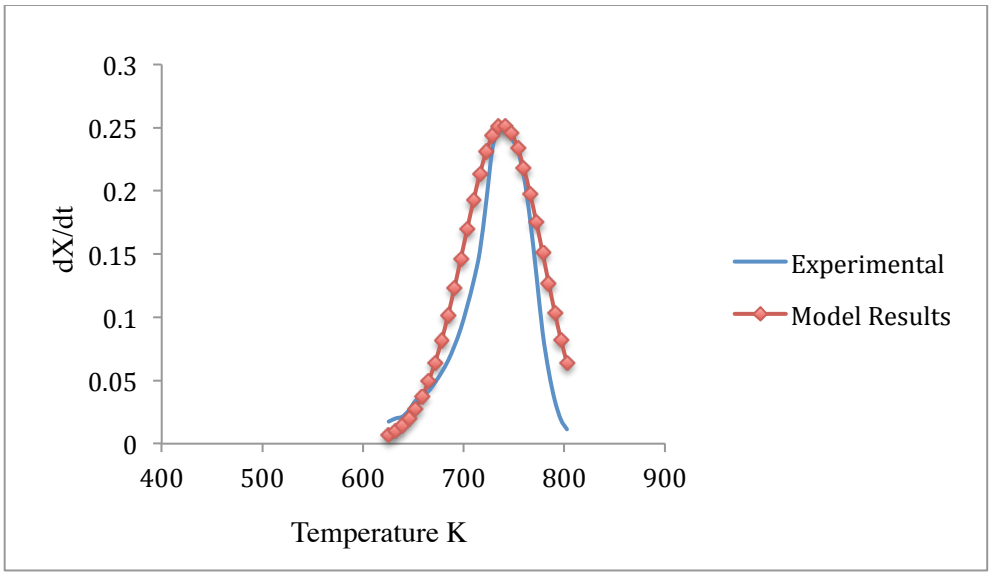

Figure 5-9. Comparison of experimental and Gaussian model results at 25 K/min

The second distribution function was the Weibull function used to model the reaction. Eventually, rearranging Eqn. 4-15 in Eqn. 4-6 and using linear interpolation of Eqn. 4-11 results in Eqn. 5-3. The following equation is solely related to the one step between the i-th and (i+1)-th steps. With respect to the MATLAB code in appendix A-1, the following equation is repeatedly calculated for the whole range of temperatures in the loop presented in Figure. 4-1.

$$\left(\frac{d\omega}{dt}\right)_{i,calc} = A\exp(-\frac{E}{RT_i})\exp(\Delta I_i)\frac{C}{B}\left(\frac{E-A}{B}\right)^{C-1}\exp\left[-\left(\frac{E-A}{B}\right)^{C}\right] \qquad 5\text{-}3$$

The mathematical relation between the Weibull function parameters (Eqn. 4-16) was used to make a better initial guess for parameter B, since there is not a big difference between the amount of B and E_0. Lower bounds and upper bounds were indicated to use as initial guesses to start the optimization process. The population size for the optimization was 3000 individuals and the maximum number of generations allowable was set at 10000 with a tolerance for the solution of 1×10^{-100}. The integration of Eqn. 5-3 on activation

energy steps was applied to calculate the derivative of conversion with respect to time for the whole period of the reaction and, finally, the Weibull distribution of results was obtained. The interval of activation energy was set between zeros to 400000 J/mol as well. As with the previous model presented in Figure 5-5, the Braun and Burnham (54) equation was used to determine the value of the pre-exponential factor. The fitness of the experimental and calculated results is illustrated in the following figures:

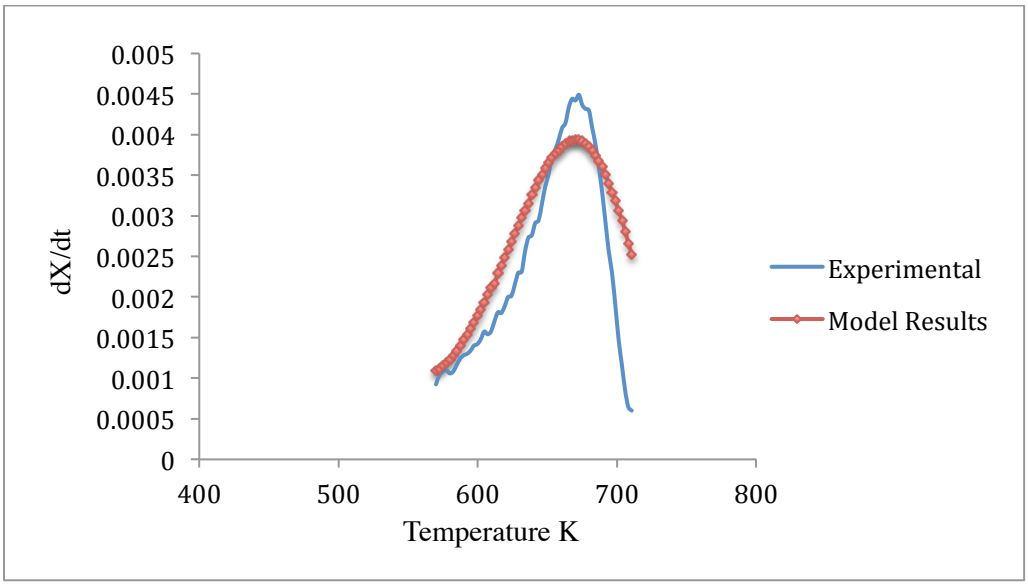

Figure 5-10. Comparison of experimental and Weibull model results at 0.5 K/min

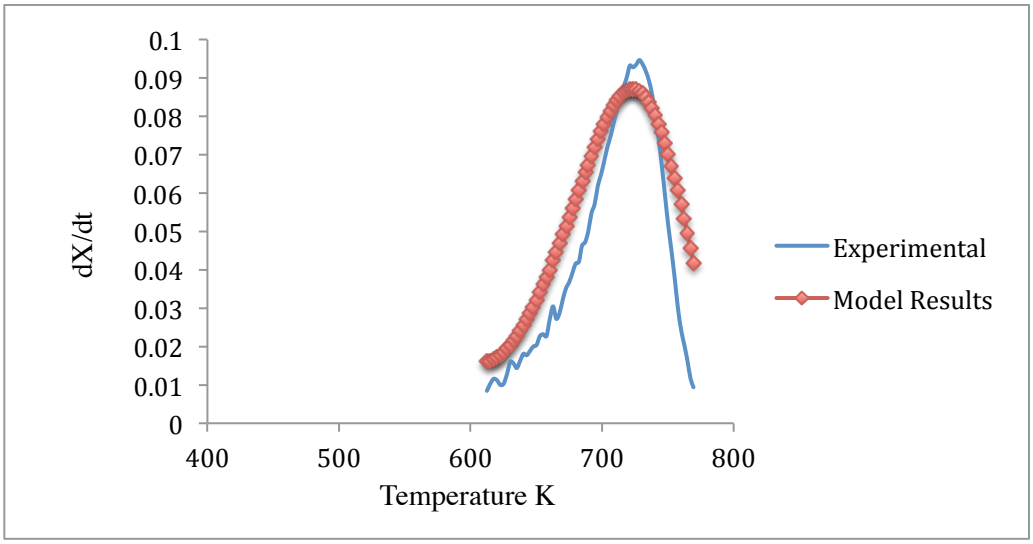

Figure 5-11. Comparison of experimental and Weibull model results at 10 K/min

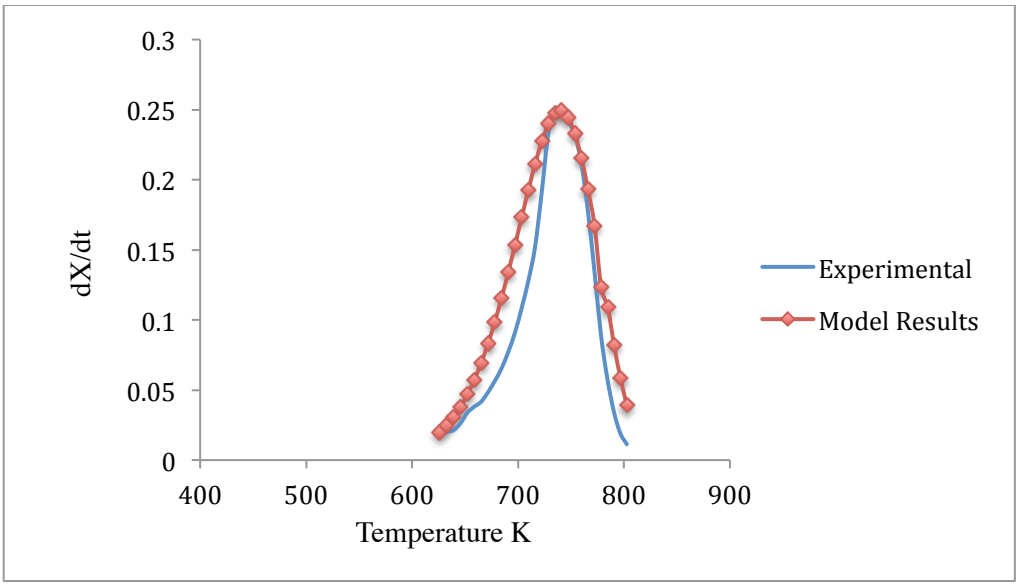

Figure 5-12. Comparison of experimental and Weibull model results at 25 K/min

The third distribution function was the Gamma function used to model the reaction. Eventually, rearranging Eqn. 4-18 in Eqn. 4-6 and using a linear interpolation of Eqn. 4-11 results in Eqn. 5-4. The following equation is solely related to the one step between the i-th and (i+1)-th steps. With respect to the MATLAB code in the appendix, the following equation is repeatedly calculated for the whole range of temperatures in a loop.

$$D(E) = \frac{1}{B\Gamma(C)}\left(\frac{E-A}{B}\right)^{C-1}\exp\left(-\frac{E-A}{B}\right) \qquad 5\text{-}4$$

The mathematical relation between Gamma function parameters (Eqn. 4-19 and 4-20) was used to decrease the number of unknown parameters by one (A and C), as shown in Eqn. 5-5.

$$D(E) = \frac{C}{E_0\Gamma(C)}\left(\frac{E-A}{E_0/C}\right)^{C-1}\exp\left(-\frac{E-A}{E_0/C}\right) \qquad 5\text{-}5$$

All of the criteria including population, generations and the interval of integrals were set exactly the same as in the previous models. As a result, the fitness of experimental and calculated results is illustrated in the following figures after running the MATLAB for the Gamma function.

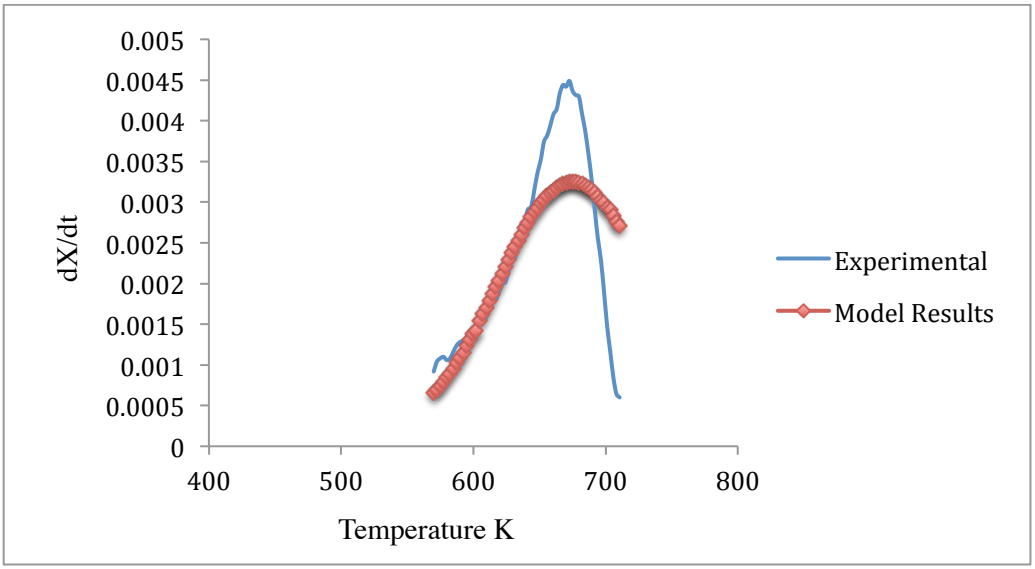

Figure 5-13. Comparison of experimental and Gamma model results at 0.5 K/min

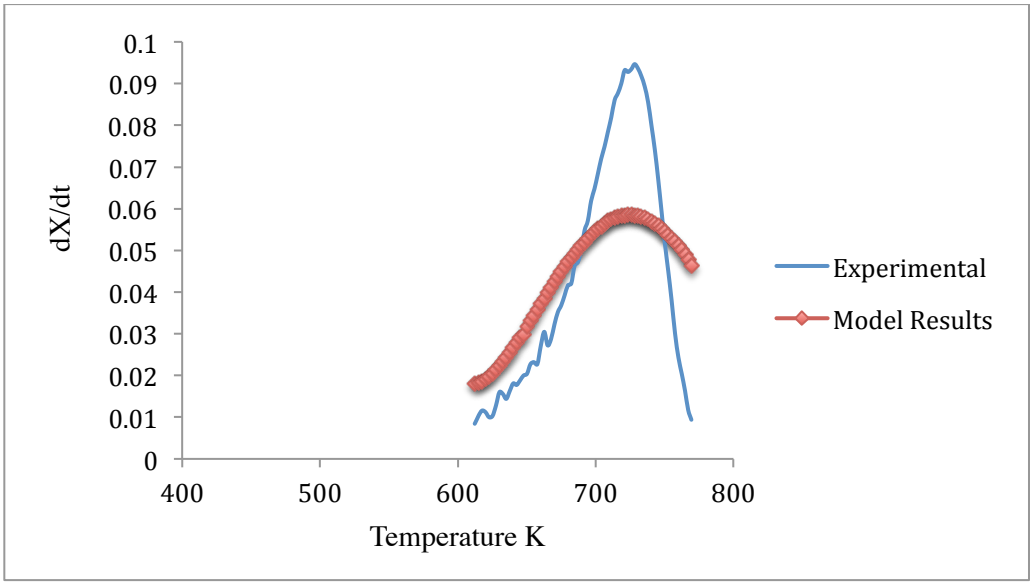

Figure 5-14. Comparison of experimental and Gamma model results at 10 K/min

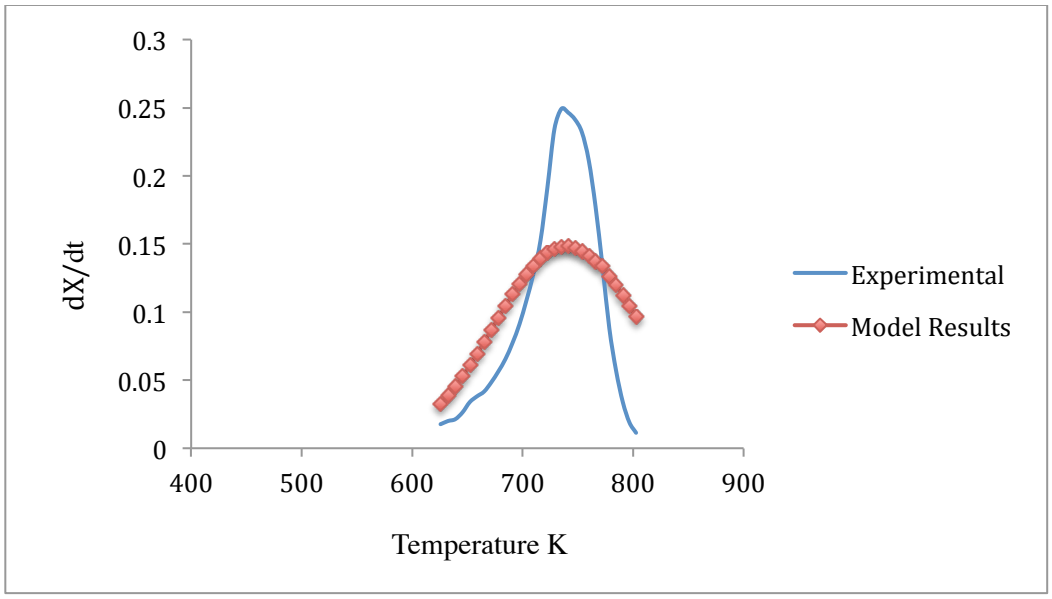

Figure 5-15. Comparison of experimental and Gamma model results at 25 K/min

As shown in the above figures, there is a big difference among the various distribution functions to explain the behavior of thermal cracking of the vacuum residue. In the next section of this chapter the statistical issues and derived kinetic parameters are considered and compared with each other to select the best one as a mathematical model.

5.3.3: Selection of the Best Distribution of Activation Energy Model

Selection of the best function is based on several statistical criteria. The residuals figure is the most important and basic statistical figure to show the priority between the models. In the residuals figure the differences between experimental and modeling results can be illustrated, which indicates the errors. Figure 5-16 shows the residuals of the models from the experimental data at 10 K/min in the TGA. It demonstrates that the Gamma results have the largest deviation from the experimental results, but the Weibull and Gaussian data estimate the real data with a better approximation and more accuracy. Inspection of the residuals shows that none of the models provide an exact fit to the data. These results are consistent the other published studies (1, 2, 4 and 49). With comparison between the

Weibull and Gaussian data, it seems the Gaussian works a little better than the Weibull at 10 K/min. The other figures for comparison of results at 0.5 and 25 K/min have been illustrated in Appendix B. However, in the next section, some more statistical parameters will be discussed and evaluated to make a stronger judgment among the models.

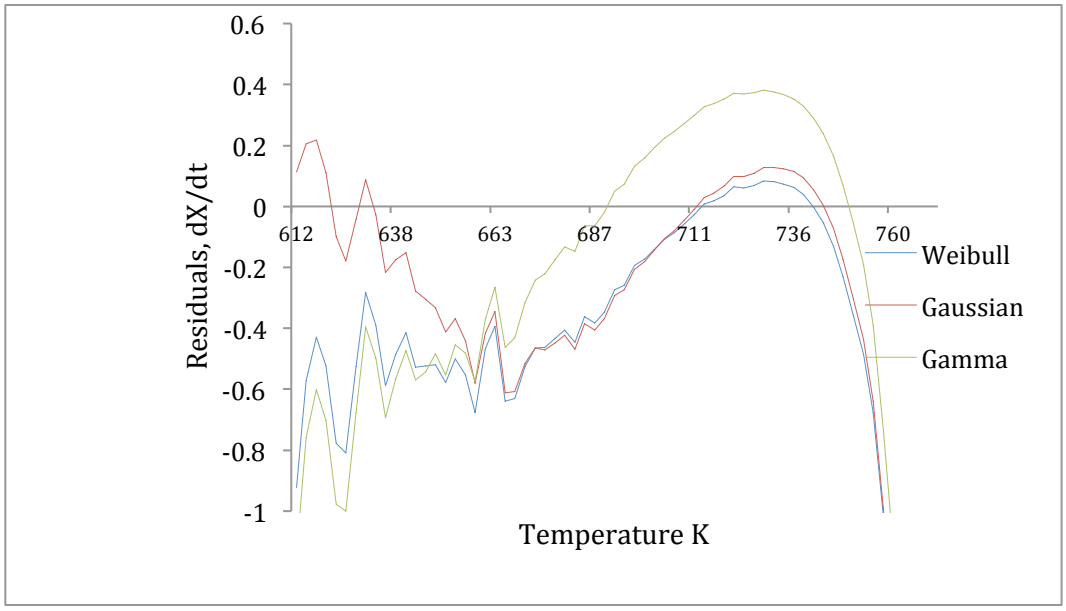

Figure 5-16. Residuals of model versus different distribution functions at 10 K/min

Figure 5-17 compares the behavior of the Weibull function at different heating rates. In this figure, the temperature range of thermal cracking changes at different heating rates. As a result, this residuals figure cannot help to effectively judge the trend of the function's behavior at different heating rates; therefore, in the next part, by using some effective statistical parameters, the priority of the functions would be recognized. Meanwhile the behavior of the other functions has been shown in Appendix B.

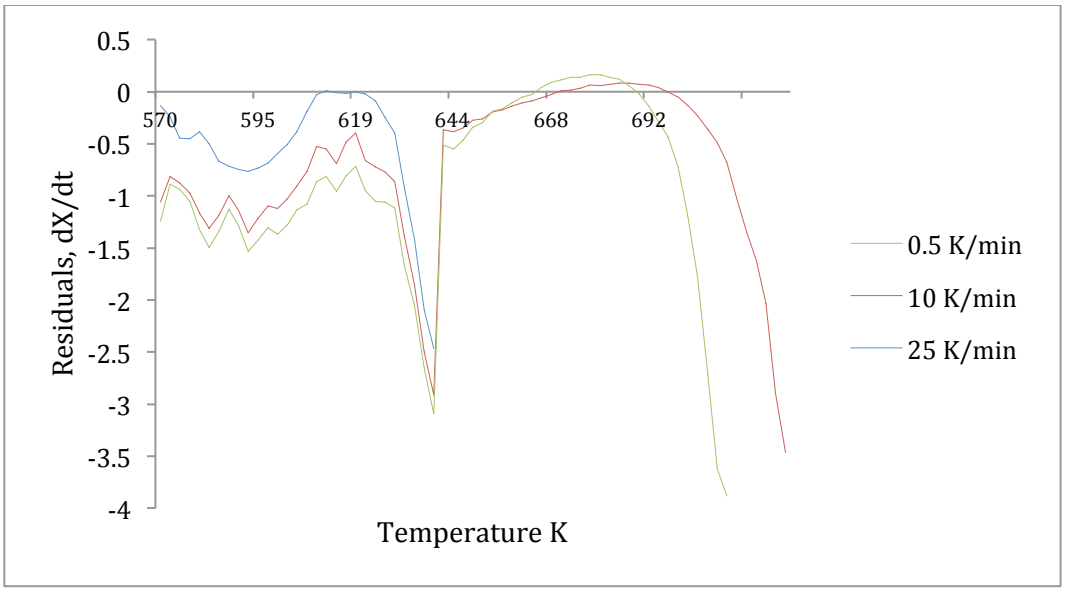

Figure 5-17. Residuals of Weibull model versus different heating rates

The calculation of standard deviations is part of the initial steps to evaluate the models mathematically. The model with the lowest standard deviation is on priority compared to the others. The following table and figure show the values and trend of the standard deviation as the heating rate and function change.

Table 5-9. Standard deviations at different heating rates for the distribution functions

Standard deviation (%) / Heating rate (K/min)	Weibull	Gaussian	Gamma
0.5 K/min	7.33%	7.33%	7.33%
10 K/min	5.94%	5.75%	8.77%
25 K/min	5%	4.5%	8.7%

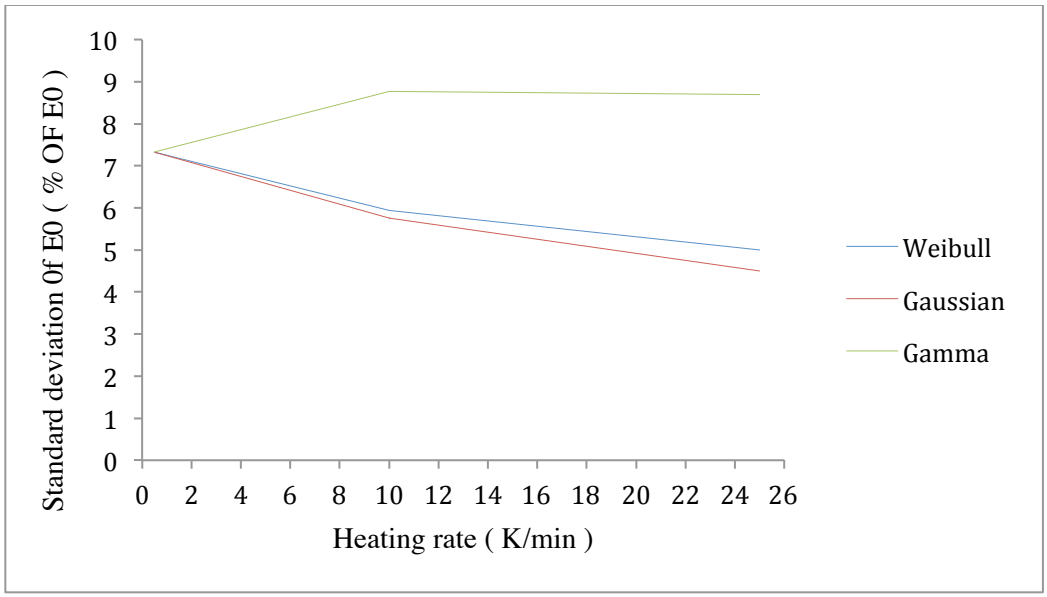

Figure 5-18. Comparison of standard deviations for different heating rates and functions

With respect to the values of standard deviations, the Gaussian function has the lowest SD among the others. However, this statistical criterion is not adequate to explain the priority because among those functions the number of parameters and observations at different heating rates are different; these complex conditions are not solely investigated by standard deviation.

The RSS, AIC, BIC and Δ_i have to be considered to determine the best function fitting the figure of derivative of the conversion with respect to time. Based on the formulas that were indicated in the last chapter, the values of those statistical parameters at heating rates of 0.5 K/min are as follows:

Table 5-10. Statistical parameters for the distribution functions at 0.5 K/min

Distribution Functions / Statistical Parameters	Weibull	Gaussian	Gamma
RSS	2.86E-05	2.91E-05	3.56E-05
AIC	-851.7	-852.8	-838.9
BIC	-845.5	-848.6	-832.7
Δ_i	1.0	0	13.8

Statistical parameters at heating rate of 10 K/min are as follow:

Table 5-11. Statistical parameters for the distribution functions at 10 K/min

Distribution Functions / Statistical Parameters	Weibull	Gaussian	Gamma
RSS	1.45E-02	1.46E-02	2.33E-02
AIC	-540.5	-542.1	-522.3
BIC	-533.9	-537.7	-503.1
Δ_i	1.5	0	19.8

Statistical parameters at heating rate of 25 K/min are as follow:

Table 5-12. Statistical parameters for the distribution functions at 25 K/min

Distribution Functions / Statistical Parameters	Weibull	Gaussian	Gamma
RSS	3.73E-02	4.35E-02	9.05E-02
AIC	-187.0	-184.6	-161.3
BIC	-182.9	-181.8	-157.2
Δ_i	0	2.5	25.7

Regarding the above tables and numbers, the Weibull and Gaussian functions are working significantly better than the Gamma function. The RSS, AIC and BIC numbers of the Weibull and Gaussian are much less than those of the Gamma. It shows that these functions are working well compared to the Gamma. On the other hand, Δ_i of the Gamma function at all heating rates is more than ten; it means that this function is not working well and this status is clearly determined by the above fitting figures. At heating rates of 0.5 and 10 K/min, the values of AIC and BIC of the Gaussian are slightly less than the Weibull's and at the heating rate of 25 K/min, the Weibull works a little better than the Gaussian. This fact shows that at 25 K/min, the skewness of the figure is more than that at 10 and 0.5 K/min. Thus, the Weibull, which has a skewness or shift parameter, can work better than the Gaussian.

By using the distribution method, the mean activation energy and standard deviation of activation energy were determined after optimizing the function parameters. Table 5-13 shows the mean activation energies at various heating rates and Figure 5-19 illustrates the trend of changing activation energy versus the heating rate.

Table 5-13. Mean activation energy at different heating rates

Heating rate (K/min)	Weibull (E_0, mean activation energy)	Gaussian (E_0, mean activation energy)	Gamma (E_0, mean activation energy)
0.5 K/min	217.5	220.4	226.3
10 K/min	218.7	221.6	225.1
25 K/min	219.0	222.0	224.8

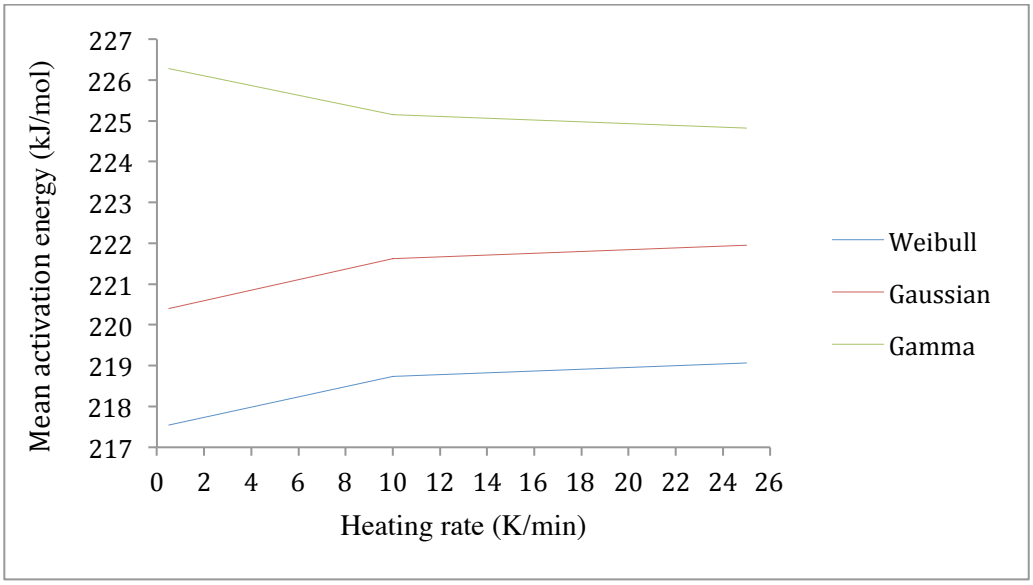

Figure 5-19. Trend of mean activation energy with the increase of heating rate

Referring to the statistical parameters, the Weibull and Gaussian results are reliable. Thus, with the increase of the heating rate, the activation energy increases because as the heating rate goes up, the difference of temperature between the sample and furnace increases. Therefore, the sample temperature is much less than the furnace temperature and the calculation is going to be done at the temperature which is higher than the sample's. As a result, activation energy has been calculated at a higher temperature and results in a higher value of activation energy. On the other hand, the trend of activation

energy at each function is nearly constant; this fact shows that there are no heating and sample size resistances to make a temperature gradient in the sample; consequently, these results are reliable. As indicated by statistical parameters, the region of Gaussian and Weibull functions in the above figure is more reliable than the Gamma function.

The Weibull and Gaussian functions are both efficient for use in the Anthony Howard method to model the thermal cracking reaction of Athabasca vacuum residue and calculate the kinetic parameters, but at low heating rates the Gaussian works better than the Weibull, and at high heating rates the Weibull can work better because this function has a skewness factor handling the skewness of the figure. At the end, the Anthony Howard method can work with those distribution functions to derive the kinetic features of the AVR.

5.4: Closed Reactor

5.4.1: Selection of the Best Temperature and Extent of Oxidization

The purpose of this study is to investigate the effect of pre-oxidation on the conversion of vacuum residue to products. To achieve this goal, a TGA was used to study both the oxidation of vacuum residue and the subsequent thermal conversion of oxidized feed. The feed was oxidized by loading a 10.0 mg sample of vacuum residue into the TGA and run at different temperatures and durations in air at a flow rate of 100 ml/min. The sample was heated to four various temperatures, including 160, 180, 200 and 220 ℃, held at reaction temperature for 10, 15, 20 and 45 minutes, and then cooled to room temperature. Thermal conversion of the pre-oxidized samples were conducted immediately after oxidation by purging the TGA with nitrogen and then heating the oven to around 700℃ in nitrogen at a flow rate of 100 ml/min. Figures 5-20 and 5-21 show the trend of mass loss in nitrogen after pre-oxidation at different temperatures and durations. Figure 5-20

presents the thermal cracking of the feed at different conditions with and without oxidation. This figure can be divided into 3 temperature ranges including room temperature to 350 ℃, 350 ℃ to 550 ℃ and 550 ℃ to 700 ℃. At the first curve related to without oxidation curve, in the first range, there is a little mass loss due to evaporation and reaction. In the second range, there is a big mass loss due to the bond cleavage of molecules and production of lighter molecules in the gas phase. In the third range, the formed coke has a very small mass loss at high temperatures up to 700 ℃, and it is because of the lack of coke gasifying. On the other hand, Figure 5-20 presents the thermal conversion data for the samples that were pre-oxidized for 10 minutes in air. Pre-oxidation causes the free radicals to cross-link which results in tougher material and enrichment of low-temperature bonds. These pre-oxidized feed have nearly the same behavior at the first temperature range, because at this range there is mostly evaporation, which is not highly involved with thermal cracking reactions. At the second temperature range, cross-linking (stronger bonds) from the pre-oxidation in the feed can stop mass loss. Therefore, thermal cracking are not breaking all the existing bonds. As a result, there is a higher amount of the produced coke and resid for the pre-oxidized feed. At the third range, as it is shown in the Figure 5-20, the remained coke at 700 ℃ is less than that for the sample without the oxidation. The penetrated oxygen at pre-oxidation process can gasifies the coke at high temperatures to carbon dioxide, and the higher temperature increases this disappearance. The effect of oxidation on the sample at 180 ℃ is the maximum compared to the other temperatures, therefore, chemisorption, polymerization and cross linking of bonds have the biggest effect at this temperature and it seems that this temperature can show the changes better than the other low temperatures.

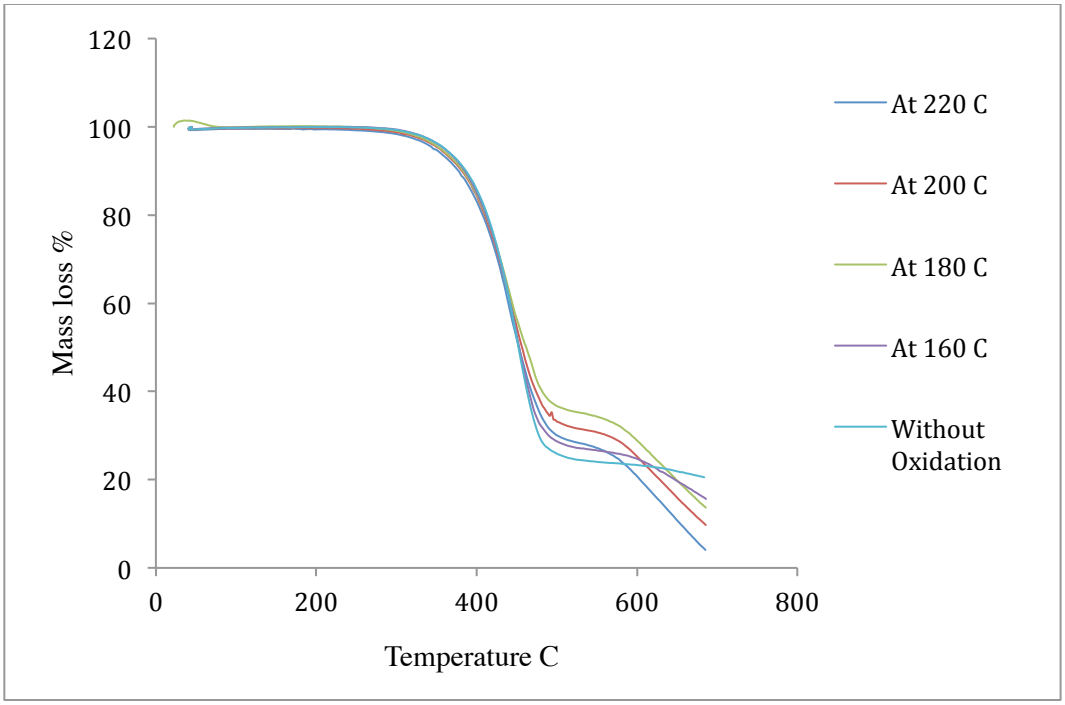

Figure 5-20. Mass loss of the oxidized Athabasca vacuum residue at various temperatures for 10 min

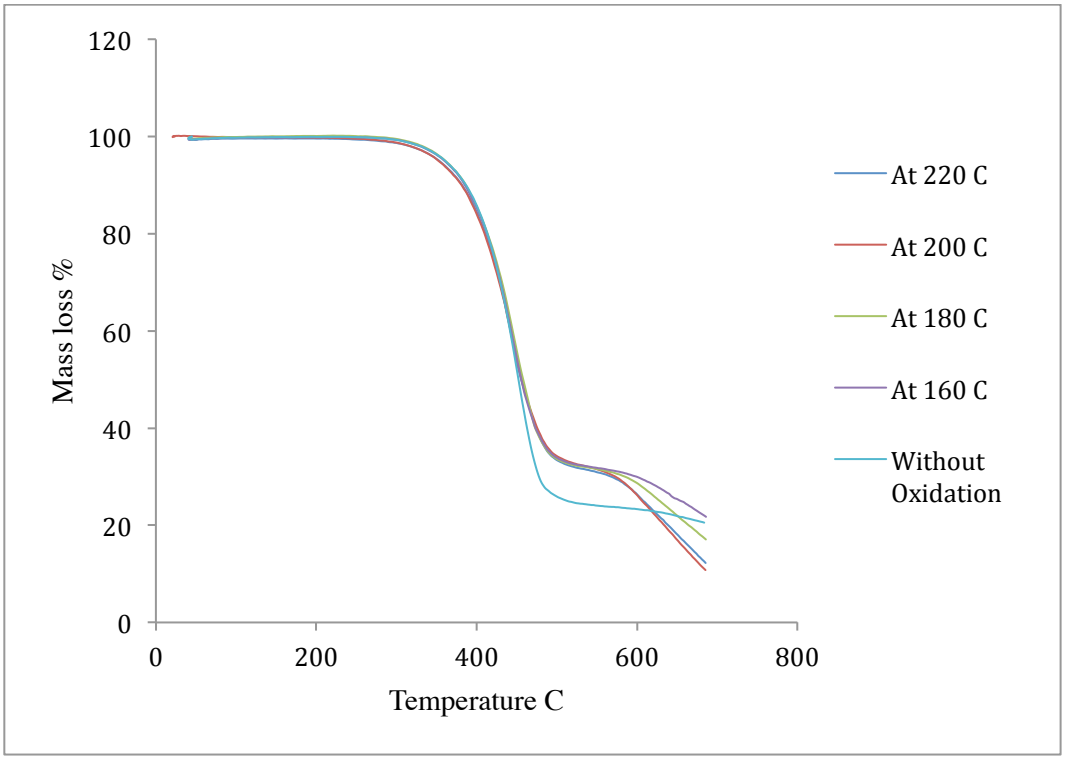

Figure 5-21. Mass loss of the oxidized Athabasca vacuum residue at various temperatures for 20 min

Based on the work by Azfar Hassan et al. (42), the type of petroleum and the concentration of oxygen affect the molecular structure of oxidized samples. They investigated the oxidation of Athabasca bitumen below and above 400℃, and they figured out two different behaviors arising from the oxidation. They showed that the tendency of this sample in coke formation during pyrolysis varies at different oxygen concentrations (42). In this study, Athabasca vacuum residue was heated to 180 ℃ and maintained for different durations at this temperature to see the change of mass loss and oxidized molecules in those conditions. Figure 5-22 shows the effect of duration on oxidation. With respect to that, the greatest change to the heavier molecular formation occurs during the 20-minute duration, because the lowest mass loss occurs during the temperature range of thermal cracking reaction.

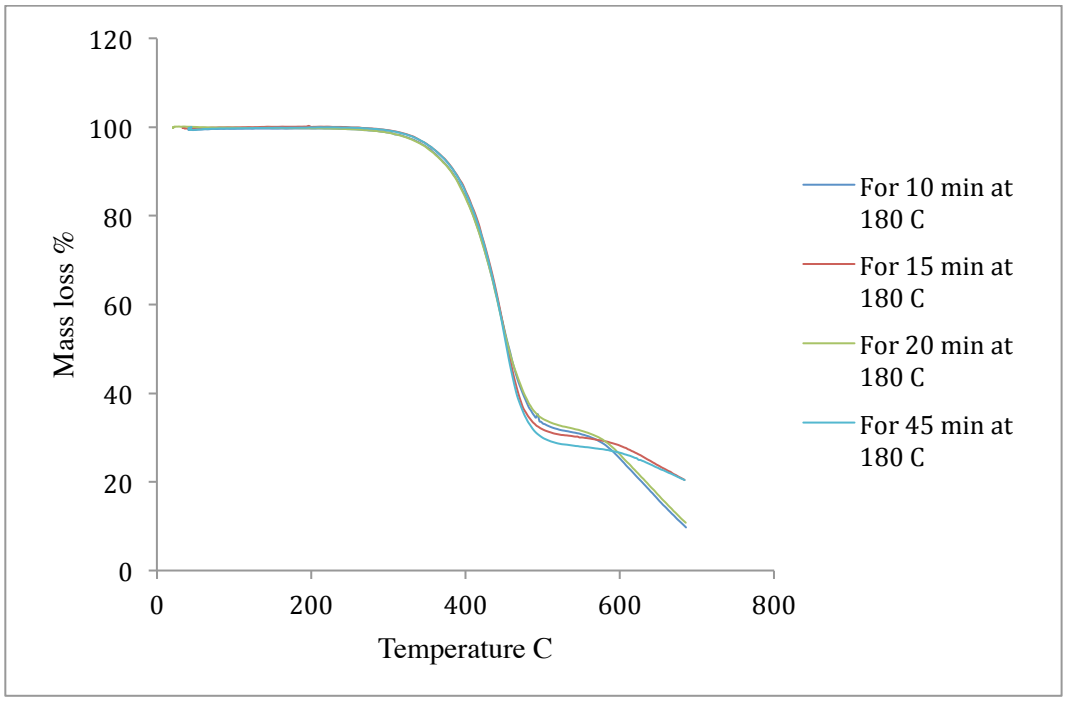

Figure 5-22. Mass loss of oxidized Athabasca vacuum residue at 180 ℃ for different periods

As a result, at such a high concentration of oxygen (21% O_2) at 180 ℃, this sample is capable of creating more strong bonds like –OH and carbonyl bonds (-C=O) to make the oxidized sample more insistent.

In conclusion, in order to indicate the oxidation effect at low temperatures, these temperature and period are appropriate for oxidation of the sample to show the maximum alteration from the pure thermal cracking.

5.4.2: Effect of Oxygen and α-FeO(OH) on Kinetic parameters and Oxidation of Athabasca Vacuum Residue

Using the optimal temperature and duration obtained from the previous section, samples of Athabasca vacuum residue were pre-oxidized with oxygen or with oxygen and an oxidation catalyst, goethite (10% wt%), at 180 ℃ for 20 min. The pre-oxidized samples were subsequently reacted in an inert atmosphere, nitrogen, at 400, 410, 420, 430 and 440 ℃ for either 30 or 60 min. Micro-batch reactors were charged with 3 g of feed and heated to reaction temperature using a sand bath. Four different conditions were tested to see the effect of goethite as a catalyst for oxidation of the vacuum residue:

1) Reactor was heated to 180 ℃ in nitrogen, maintained for 20 min, cooled to ambient conditions, re-heated to the set-point temperature (400, 410, 420, 430 and 440 ℃) and maintained for either 30 or 60 min at the set-point. These experiments are identified as N_2-N_2 Non-catalyst in the tables and figures.

2) In this set, the conditions are similar to set (1) with the exception that the purge gas existing in the micro-reactor at the first step of the heating process (heating to 180 ℃). In this set, oxygen was first purged to oxidize the vacuum residue at 180 ℃ for 20 min; these experiments are identified as O_2-N_2 Non-catalyst in the tables and figures.

3) In this set, a 3 g of the vacuum residue with a 0.33 g of goethite (10% wt) were added to the micro-reactor and the same procedures as mentioned above were repeated to see the effect of goethite in the oxidation without oxygen. These experiments are identified as N_2-N_2 catalyst.

4) In this set, a 3 g of the vacuum residue with a 0.33 g of goethite (10% wt) were added to the micro reactor and the same procedures as mentioned above were repeated to see the effect of goethite in the oxidation with. These experiments are identified as O_2-N_2 catalyst in the tables and figures.

Work by Blake Olson (66) showed that it takes about 20 seconds for a sample to attain a temperature of approximately 200 ℃ and 60 seconds to attain a temperature of around 400 ℃. Therefore, these time lags were added to the isothermal periods. The final products such as gas, liquid and coke plus resid were separated and weighted. The following figures show yields of final products at each of the experimental conditions. The gas yields produced at 30 and 60 min are presented in Figures 5-23 and 5-24, respectively.

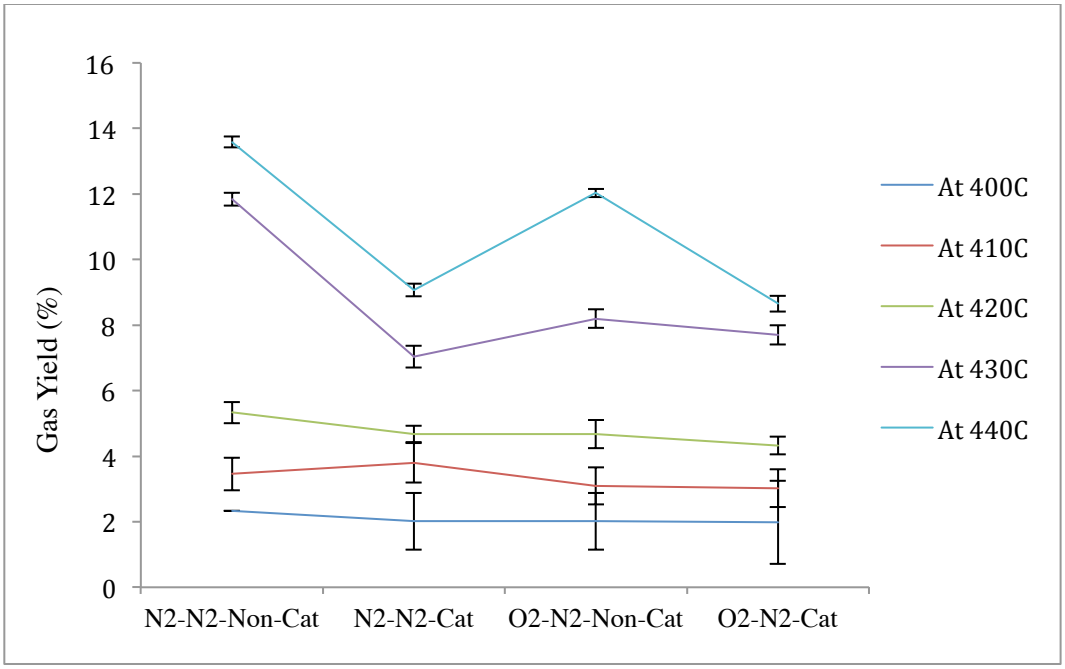

Figure 5-23. Gas yield in different condition for 30 min as a reaction residence time

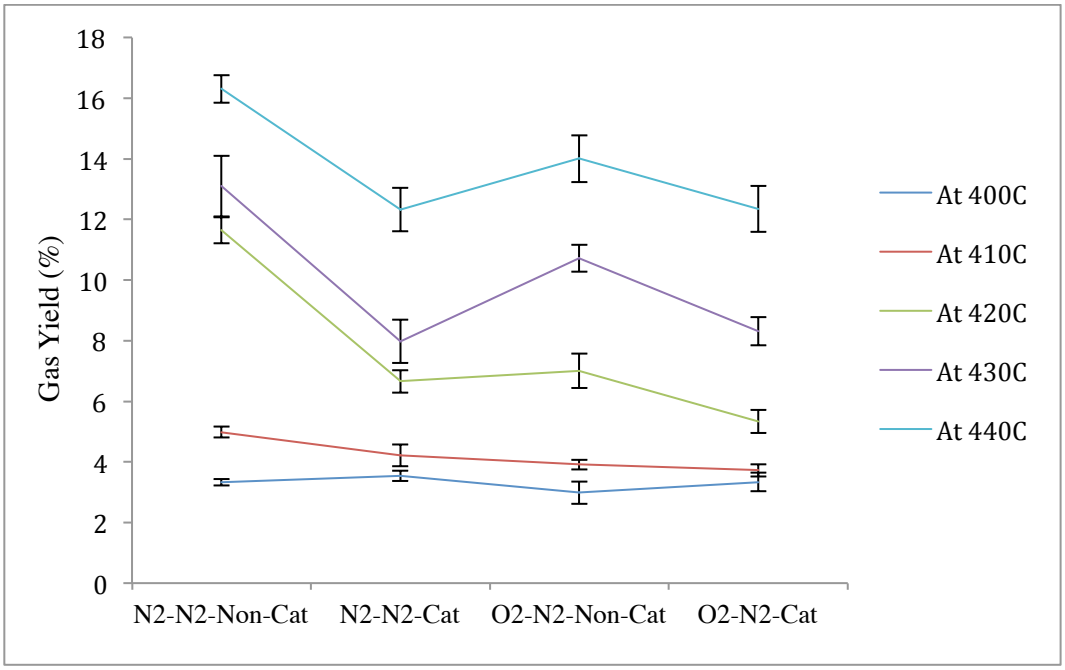

Figure 5-24. Gas yield in different conditions for 60 min as a reaction residence time

The combined coke plus residue yields produced at 30 and 60 min are presented in Figures 5-25 and 5-26, respectively.

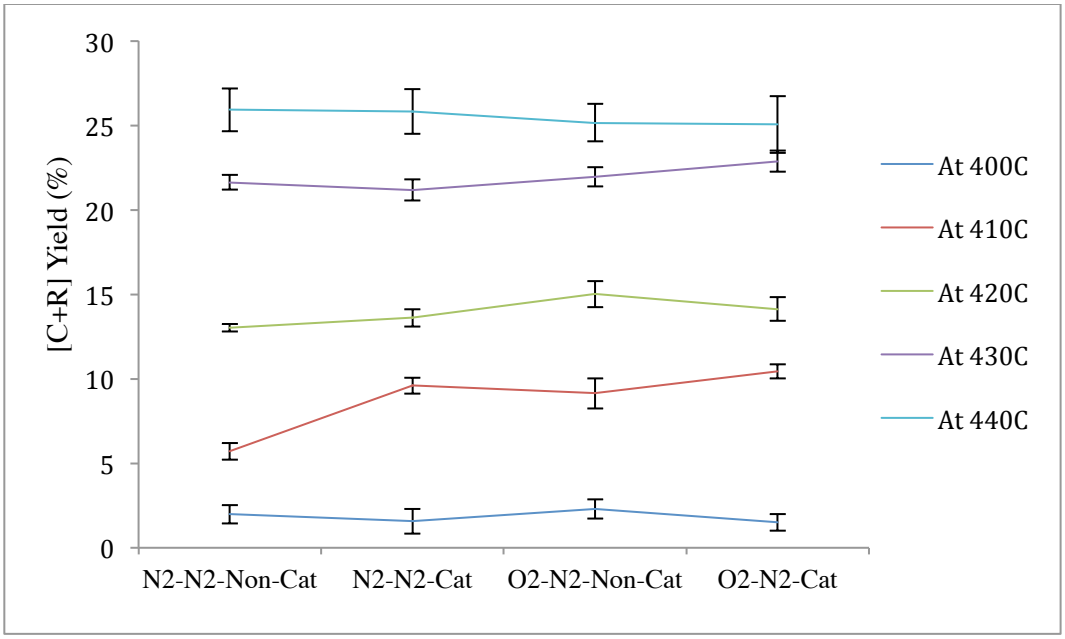

Figure 5-25. Coke plus resid yield in different conditions for 30 min as a reaction residence time

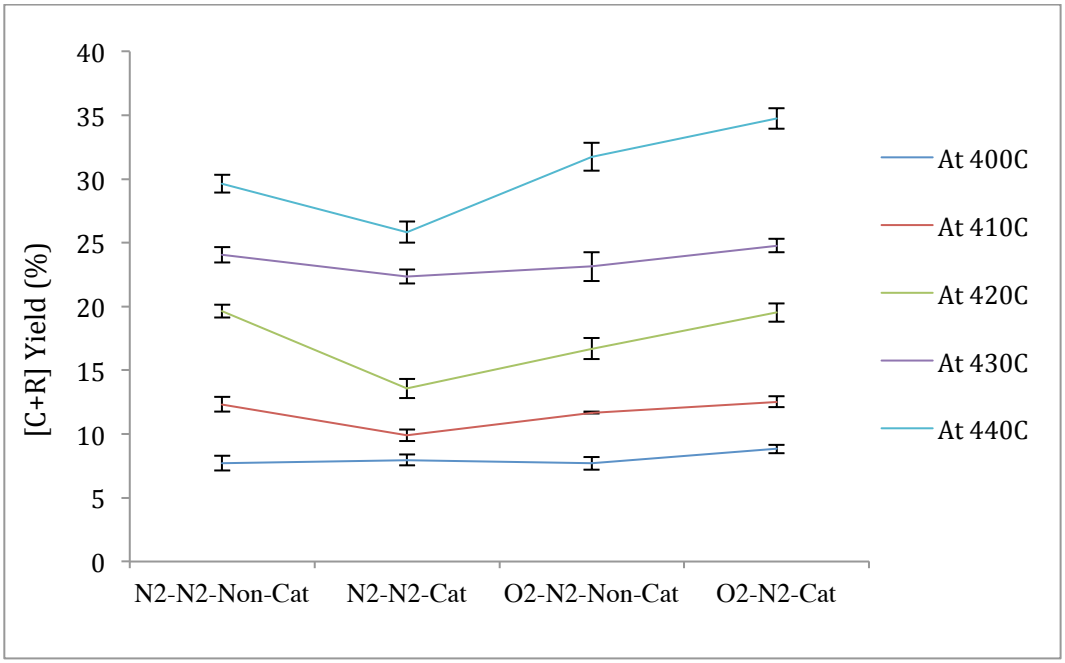

Figure 5-26. Coke plus resid yield in different conditions for 60 min as a reaction residence time

The liquid produced at 30 and 60 min are presented in Figures 5-27 and 5-28, respectively.

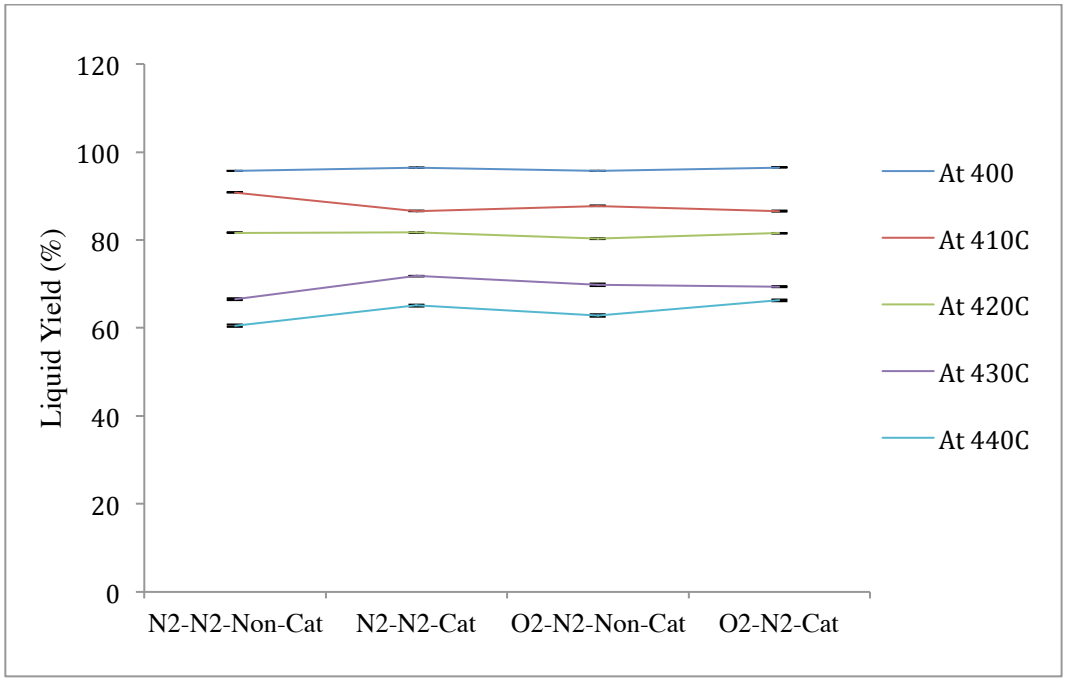

Figure 5-27. Liquid yield in different conditions for 30 min as a reaction residence time

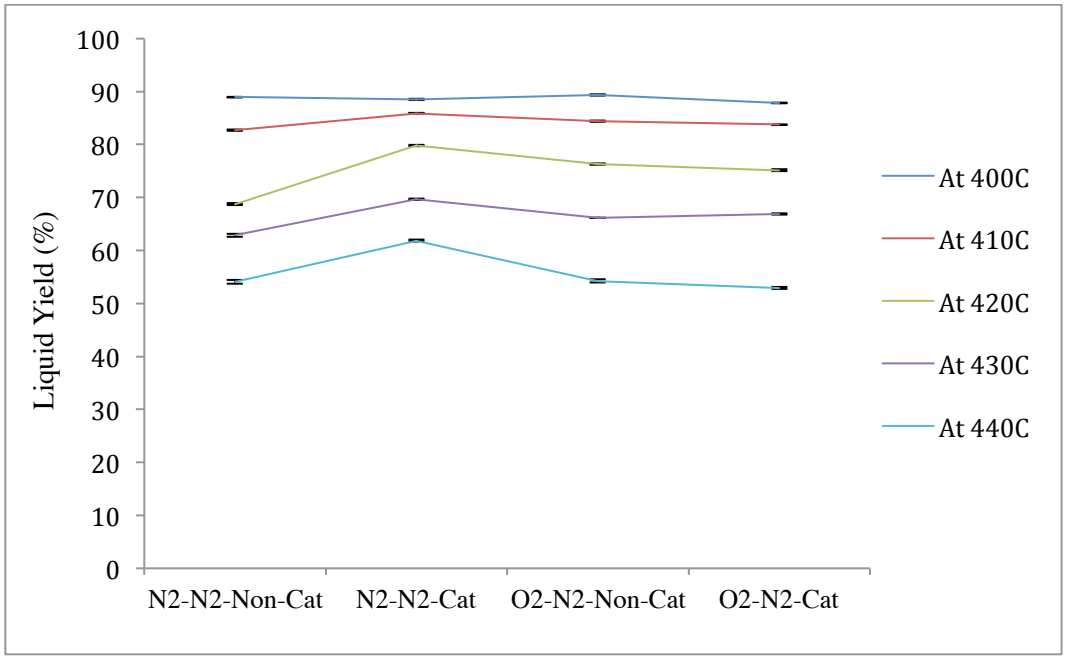

Figure 5-28. Liquid yield in different conditions for 60 min as a reaction residence time

With respect to the above figures, it is shown that when the sample is exposed in oxygen for oxidation, it produces lower gas and higher coke in the pyrolysis process. However, the effect of goethite in the oxidation with oxygen is negligible. The lack of the effect of goethite as a catalyst can be caused by the high amount of sulfur existing in Athabasca vacuum residue. Athabasca vacuum residue consists of big molecules, which can block the active sites of goethite. Ming-Chun lu (47) has used the goethite as a catalyst with hydrogen peroxide to oxidize organic compounds of 2-chlorophenol. Ferrous ions are the important products of reductive dissolution of goethite; this reaction, which produces hydroxyl radicals (–OH), is called the Fenton-like reaction. In this work, oxygen was used instead of hydrogen peroxide to oxidize Athabasca vacuum residue. However, as explained by the figures, oxygen does not change the amount of products too much at each temperature. The work of S. V.Koto et al has demonstrated that in the asphalt manufacturing process, there is a diversity of reactions, including oxidative dehydrogenation, dealkylation, oxidative polymerization and cracking, followed by the consolidation of the oxidization products. Progressive hydrogen loss occurs in the consolidation process during oxidation. The effect of the consolidation process appears in the formation of asphatenes, including high molecular weight products with a high degree of aromatic hydrocarbons. S.V. Kotov (47) indicated that the aromatic hydrocarbons in vacuum residue actively participate in oxidation reactions, the total conversion of aromatic hydrocarbons was more than 60 wt%, and the major eventual products of the oxidation process were resins and asphaltenes. Eventually, the results derived by the oxidation of Athabasca vacuum residue make sense with S.V. Kotov's analyzed results.

To calculate the kinetic parameters in a batch reactor, based on the model mentioned in the last chapter, the following schematic of the products and reactant was assumed:

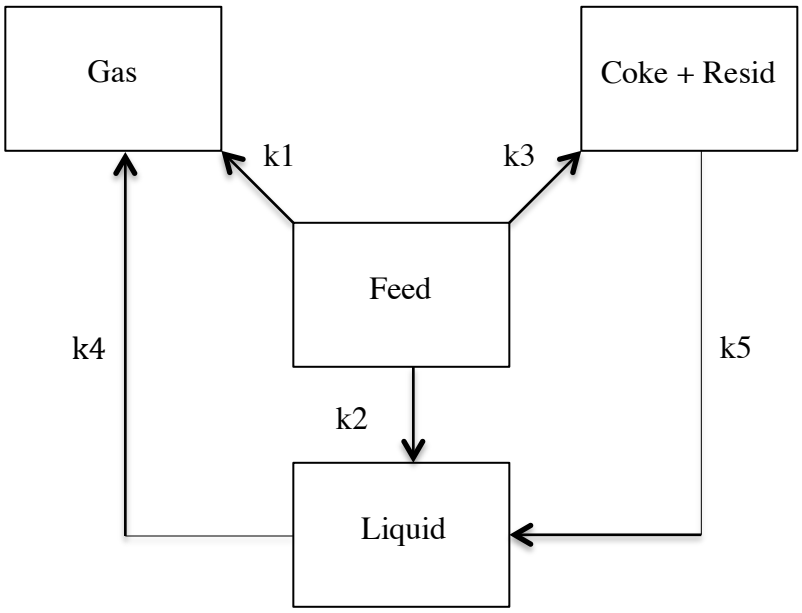

Figure 5-29. Schematic of products and reactant during cracking

All of the reactions are assumed to be first-order reactions. Based on the kinetic equation in the last chapter for this model, the reactions have to be done at different temperatures and durations so that these equations can be calculated in parallel. There are five reaction constant rates in each condition; so five independent equations are needed to calculate the constant with respect to the final conversions. On the other hand, some other temperatures should be reached to derive the pre-exponential and activation energy by using the Arrhenius equation. In this work, five various temperatures have been used, therefore regression among these temperatures results in the kinetic parameters for each reaction constant rate. The validity of this model for the batch reactor was eventually checked by a correlation coefficient of the Arrhenius equation at different temperatures. All of the kinetic parameters were written in MATLAB, and the genetic optimization method was used to calculate and converge the five kinetic parameters. In the genetic method, with respect to Jasvinder's results (60), the initial guess of the reaction constants was determined. All of the reaction constants were started with 0.01 as an initial guess.

The population size and generations were 1000 and 10000, respectively. The tolerance of the calculated reaction constant rate was set at 1×10^{-100}. The following table shows reaction constants obtained after running and converging by MATLAB for the N_2-N_2 Non-catalyst condition at each isothermal process.

Table 5-14. Reaction constants of Athabasca vacuum residue in the N_2-N_2 Non-catalyst condition

Constant / Temperature	k1	k2	k3	k4	k5
400 ℃	1.17E-3	1.15E-2	8.25E-3	2.0E-4	6.50E-3
410 ℃	1.85E-3	1.55E-2	1.71E-2	1.12E-3	1.13E-2
420 ℃	6.19E-3	3.81E-2	1.791E-2	2.66E-3	1.39E-2
430 ℃	7.56E-3	3.88E-2	4.51E-2	8.37E-3	2.87E-2
440 ℃	1.74E-2	7.49E-2	5.37E-2	1.18E-2	4.07E-2

The following table shows the reaction constants obtained after running and converging by MATLAB for the O_2-N_2 Non-catalyst condition.

Table 5-15. Reaction constants of Athabasca vacuum residue in the O_2-N_2 Non-catalyst condition

Constant / Temperature	k1	k2	k3	k4	k5
400 ℃	7.0E-4	8.88E-3	1.76E-2	1.80E-4	6.7E-3
410 ℃	9.7E-4	1.91E-2	2.19E-2	3.10E-4	1.43E-2
420 ℃	2.43E-3	3.29E-2	3.27E-2	2.51E-3	1.43E-2
430 ℃	4.16E-3	3.30E-2	6.99E-2	5.09E-3	3.89E-2
440 ℃	1.67E-2	8.63E-2	7.89E-2	7.99E-3	4.91E-2

The following table shows reaction constants obtained after running and converging the equations by MATLAB for the N_2-N_2 catalyst condition at each isothermal process.

Table 5-16. Reaction constants of Athabasca vacuum residue in the N_2-N_2 catalyst condition

Constant / Temperature	k1	k2	k3	k4	k5
400 ℃	9.2E-4	1.14E-2	1.08E-2	1.20E-4	7.35E-3
410 ℃	1.11E-3	1.91E-2	1.12E-2	2.0E-4	8.3E-3
420 ℃	2.94E-3	2.37E-2	2.25E-2	2.09E-3	1.57E-2
430 ℃	4.03E-3	4.01E-2	2.68E-2	2.10E-3	3.99E-2
440 ℃	1.67E-2	7.72E-2	6.55E-2	9.94E-3	4.37E-2

The following table shows reaction constants obtained after running and converging the equations by MATLAB for the O_2-N_2 catalyst condition at each isothermal process.

Table 5-17. Reaction constants of Athabasca vacuum residue in the O_2-N_2 catalyst condition

Constant / Temperature	k1	k2	k3	k4	k5
400 ℃	5.80E-4	7.68E-3	1.39E-2	9.00E-5	5.99E-3
410 ℃	7.50E-4	9.85E-3	2.47E-2	2.70E-4	1.19E-2
420 ℃	2.02E-3	3.14E-2	2.70E-2	1.76E-3	1.34E-2
430 ℃	3.45E-3	3.96E-2	6.08E-2	4.51E-3	2.47E-2
440 ℃	1.58E-2	7.06E-2	7.96E-2	6.09E-3	5.50E-2

By using Arrhenius equation and regression among the five temperatures in each condition, activation energy was obtained. Based on Arrhenius equation, the plot of ln(k) versus 1/T should results in a straight line with a slope of –E/R. The obtained activation energies are as follow:

Table 5-18. Activation energy for Athabasca vacuum residue reactions in a batch reactor

Condition	N_2-N_2 Non-catalyst	N_2-N_2 Catalyst	O_2-N_2 Non-catalyst	O_2-N_2 Catalyst
E_1 (kJ/mol)	276±82	282±61	310±57	323±52
E_2 (kJ/mol)	186±66	181±41	203±31	232±67
E_3 (kJ/mol)	188±69	177±58	165±38	174±39
E_4 (kJ/mol)	405±112	446±138	415±95	450±127
E_5 (kJ/mol)	183±42	204±75	199±46	205±47

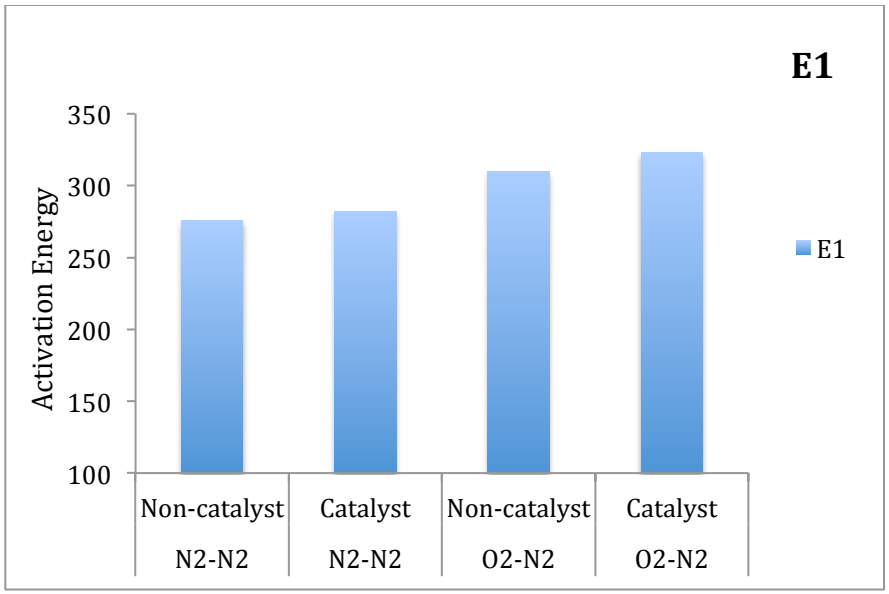

Figure 5-30. Change of E1 for reactions in each set

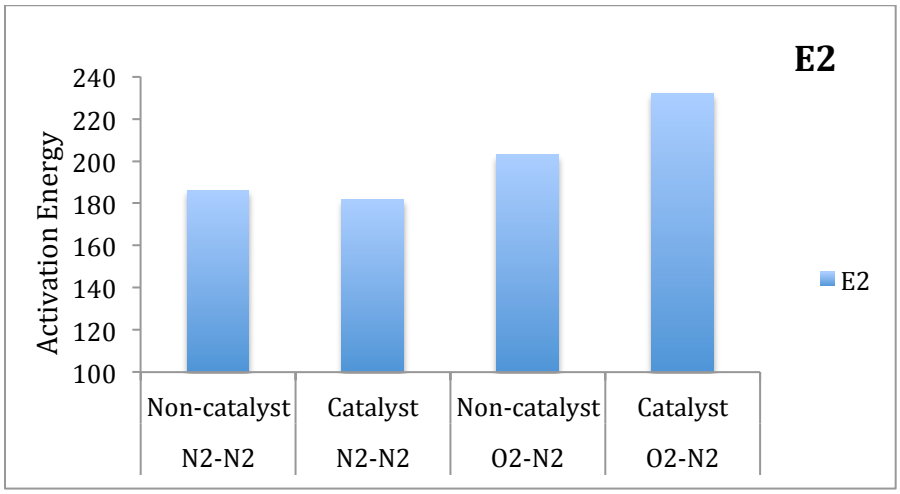

Figure 5-31. Change of E2 for reactions in each set

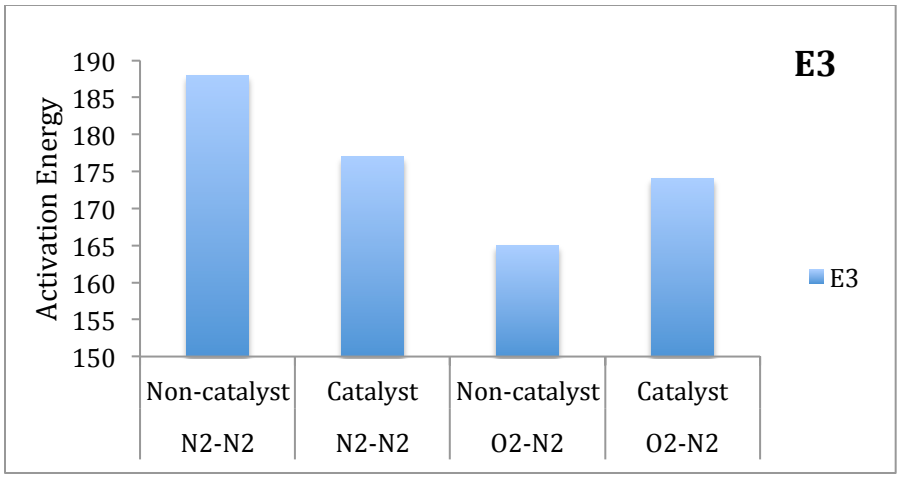

Figure 5-32. Change of E3 for reactions in each set

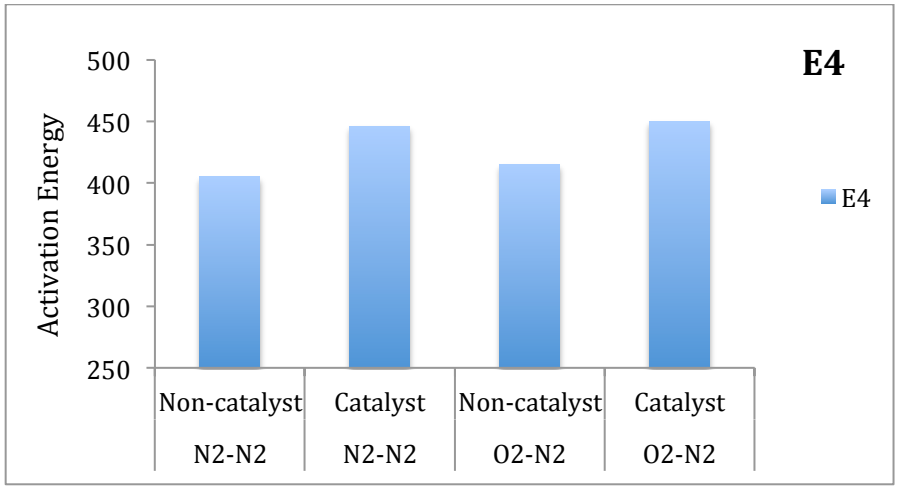

Figure 5-33. Change of E4 for reactions in each set

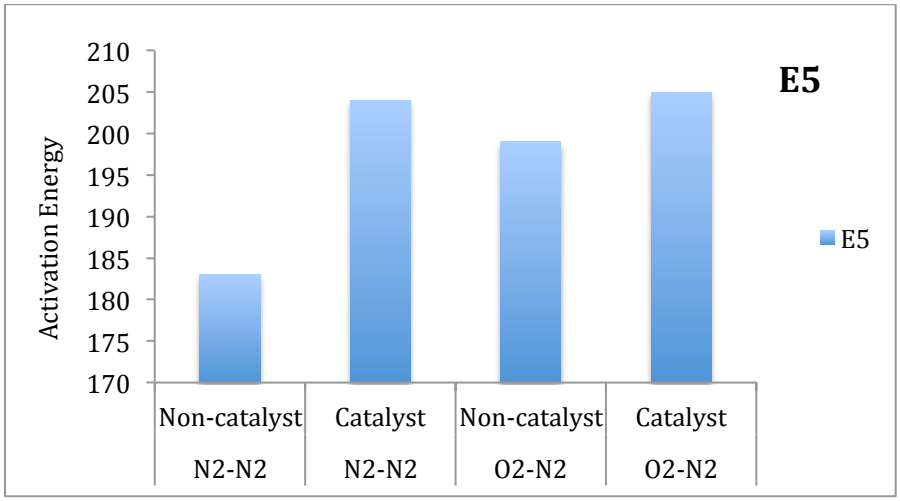

Figure 5-34. Change of E5 for reactions in each set

Regarding the above figures, goethite does not change the value of activation energy significantly, but the comparison of activation energies shows a big difference between the reaction categories. In the process schematic, the coke and residue are the heaviest products of cracking of Athabasca vacuum residue that have a high value of activation energy to produce the liquid product. The change of activation energies due to pre-oxidation shows the polymerization of radical. Ceiling temperature is a degree of the propensity of polymers to revert to their monomers (64). When a polymer is exposed at its ceiling temperature, the rate of polymerization and depolymerization of the polymer are equal. In this study, it indicates that the temperature of pre-oxidation process is less than the ceiling temperature of Athabasca vacuum residue because the amount of activation energy, from the heavier products to lighter products, has increased. Pre-oxidation of Athabasca vacuum residue is initiated with radical precursors (66):

Initiation $RH \rightarrow R^* + H^*$ 5-6

When oxygen is reacted with the recently formed radical (R*), a peroxy radical is created during the propagation step:

Propagation $R^* + O_2 \rightarrow ROO^*$ 5-7

Extremely reactive ROO* then abstracts an unstable hydrogen from another polymer molecule producing the hydrogen peroxide species, in addition to a polymer radical. Eventually, the process can continue:

$$ROO^* + RH \rightarrow ROOH + R^* \quad 5\text{-}8$$

Grassie and Scott (66) state that propagation step has a low activation energy, and creation of hydroperoxide in reaction 5-8 has an higher activation energy. Therefore, in most polymers the rate of this step plays the main role on the overall rate. Monomolecular degradation of hydroperoxide needs relatively higher activation energy due to an O=O bond in hydroperoxide. As a result, based on the obtained activation

energies in this study, the pre-oxidation temperature is less that the ceiling temperature of AVR, and it could not have provided the required energy to decompose the hydroperoxide (ROOH) (66). Reaction behavior of the pre-oxidized AVR can be explained based on the chain reactions presented in chapter two, reactions 2-1 to 2-7, just during the oxidation process the probability of the disproportionation step is higher than the recombination step, so the higher production of olefins can cause the higher production of coke in the products. In addition to the reactions presented in the propagation step (reactions 2-2, 2-3, 2-4 and 2-5), there may be anywhere from a few thousands of propagation steps depending on several factors such as radical and chain reactivity. The mechanism of this propagation can be as follows (65):

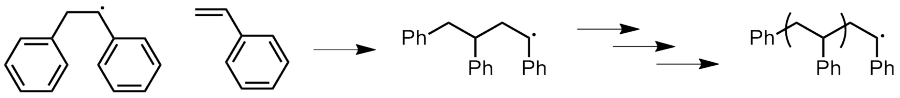

Figure 5-35. Propagation of polystyrene with a phenyl radical initiator

In this process, the direction of reaction from coke plus resid to gas has been omitted because the amount of gas produced by the coke and resid product is really negligible. In the meantime, the liquid product can produce the gas product in parallel with the initial sample, which has less activation energy compared to the initial sample. The concentration of heteroatom-containing molecules in the heaviest fractions is high, so coke plus resid products have a higher amount of heteroatoms than the other products; these heteroatoms have a significant influence during upgrading (10). Sulfur exists in several shapes in the vacuum residue. Some of the sulfur is in sulfide form, connecting two-ring structures that can be easily cleaved during the thermal cracking. These types of molecules create smaller and lighter molecules, which go into the liquid product. The nitrogen content in vacuum residue is lower than the sulfur content, but this nitrogen

content is even tougher than sulfur in thermal cracking. In addition, nitrogen compounds are inhibitors that are adsorbed on the catalyst surface, deactivating the catalyst (10). The coke plus resid product, which remains after the thermal cracking, consists of a high concentration of sulfur compared to the other products and even the initial sample. The thermal chemistry of heavy oils and bitumen is complicated because of wide variations in the chemical compositions. The most resistant components in bitumen are asphaltenes and resins, which make a major contribution to coke formation during the thermal cracking (10). In general, asphaltenes are believed to contain large polynuclear aromatic rings ranging from 6 to 20 rings (61). The aromatic compounds, which have been connected by sulfur (C-S-C), have already been dissociated to produce lighter products in the thermal cracking of the initial sample, and they have gone into the liquid fraction. However, those aromatics, which have been connected by C-C bonds, still exist in the coke and resid fraction of products. On the other hand, Sheu et al. (62) have shown that aggregating asphaltenes can hinder the conversion of heavy residue to the lighter products and it even can boost the propensity to coke formation. When the liquid fraction had a low concentration of asphaltenes, smaller aggregations were created that could be cleaved to monomers during the thermal cracking. During the oxidation process, asphaltenes creation would cause an increased in the value of activation energy for the reaction of the sample and heavier products to the lighter products. The following table shows the actual bond dissociation energies (actual activation energy) in thermal cracking.

Table 5-19. Bond dissociation energies (10)

Chemical Bonds	Energy, kJ/mol
H-H	436
H-O	464
H-S	368
H-N	390
C-C (aliphatic)	355
C=C	611
C≡C	837
C-H (n-alkanes)	410
C-H (aromatic)	462
C=O	805
C=N	615
C-S	322
C-N (in amine)	351
O=O	498
N-O	631
C-O (in methoxy)	343
H-Cl	432
C-Cl	330
N-Cl	200
O-Cl	200
S-Cl	250
N≡N	945
S-O	265
N-N	160
O-O	204

The coke and resid fraction often consists of C-C, C-H, C=C (in the aromatic rings). These strong bonds mostly remain intact after the cracking and go into the heaviest

fraction product. Rahimi et al. (10) has studied the deasphalted Athabasca bitumens; they have shown that the deasphalted bitumen produced a similar liquid yield, but a lower coke yield is obtained compared to the coking of Athabasca bitumen. On the other hand, the liquid product of the deasphalted bitumen has fewer olefin compounds, so it can be assumed that the coke product of the liquid fraction does not go into the coke and resid fraction product.

As a result, the small effect of oxidation and goethite on activation energy and final product concentrations come from the amount of asphaltenes and polymerized molecules leading to coke formation during the thermal cracking. However, ordinarily the components of vacuum residue are in a fine balance. Any physical or chemical treatments can change this balance and result in instability followed by asphaltenes precipitation, phase separation and sediment formation (63).

5.5: Comparison Between the Open and Closed Reactor Results

To investigate the effect of open and closed reactor during thermal cracking, Athabasca vacuum residue was exposed in the TGA with the same process as in the closed reactor. A 10 mg of Athabasca vacuum residue was loaded in the TGA's crucible for six different conditions, heated to 400, 420 and 440 ℃, and maintained for 30 and 60 min at these temperatures in nitrogen as an isothermal process (pyrolysis). The same processes were done with the closed reactor in the sand bath. A 3 g of Athabasca vacuum residue was loaded in the micro-reactor and purged with nitrogen, and put into the sand bath. In the open reactor (TGA) there are only two products, such as gas and coke, but in the closed reactor there are three products such as gas, liquid and coke. The K factor is defined as a Gas/Liquid ratio. The gas term is exactly the amount of gas produced in the TGA minus the amount of gas produced in the closed reactor. This term shows that how much gas has

been potentially capable to be produced in an open reactor unless it has not been produced in the closed reactor. The liquid term is the amount of liquid produced in the closed reactor minus the gas term in the K factor.

$$K = \frac{Gas}{Liquid} = \frac{y}{x} \qquad 5\text{-}9$$

The yield of gas in the TGA after each condition is as follows:

Table 5-20. Gas yield of Athabasca vacuum residue in TGA

Temperature / Duration	400℃	420 ℃	440 ℃
30 min	0.5156	0.7095	0.7688
60 min	0.5832	0.7255	0.7758

Using the following equation results in the K factor at 400 and 420 ℃:

$$\left(Yield_{gas}\right)_{batch} + \left(\frac{K}{1+K}\right)\left(Yield_{liquid}\right)_{batch} = \left(Yield_{gas}\right)_{TGA} \qquad 5\text{-}10$$

Not even the entire liquid product is equivalent to the produced gas in the TGA at 440℃, but also some portion of the coke in the closed reactor is equivalent to the produced gas in the TGA. Therefore, the following equation was used to calculate K' factor at 440 ℃:

$$\left(Yield_{gas}\right)_{batch} + \left(Yield_{liquid}\right)_{batch} + \left(\frac{K'}{K'+1}\right)\left(Yield_{coke}\right)_{batch} = \left(Yield_{gas}\right)_{TGA} \qquad 5\text{-}11$$

Regarding to the above equations K and K' factors are derived; Table 5-21 and 5-22 show the obtained factors in each condition:

Table 5-21. K factor at 400 and 420 ℃ and different durations

Temperature / Duration	400℃	420 ℃
30 min	1.060	4.093
60 min	1.620	7.780

Table 5-22. K' factor at 440 ℃ and different durations

Temperature / Duration	440 ℃
30 min	0.1072
60 min	0.3217

As shown at the above reactor, there are different numbers of K and K' factors; this is the reason for the different activation energy numbers between the open and closed reactor, because in the TGA there is not any thermodynamic equilibrium between the gas and the remaining sample in the crucible. In fact, all of the cracked products are blown away by purge gas after the thermal cracking. But in the micro reactor, there is another mechanism for products. In the closed reactor there is a thermodynamic equilibrium between the gas and remaining sample. As a result, as the temperature goes higher, the pressure increases and the permeation of cracked molecules into the gas phase becomes harder. In other words, the produced radicals in the liquid phase are going to be rearranged in the liquid phase again and will keep cracking the remained products in this phase. Eventually in the batch reactor, the gas phase is highly influenced by the closed ambient at high pressure.

As demonstrated by the change of K and K' factors in Table 5-21 and 5-22, K value increases in the liquid phase while temperature is going up; this indicates that residue molecules and radicals at higher temperature and pressure can be rearranged more, and they stay in the liquid phase to continue thermal cracking reactions.

Chapter 6: Conclusions

Accurate estimates of kinetic parameters of heavy oil thermal cracking are required for the design, optimization and development of processes related to heavy oil upgrading. In this study, thermal cracking of Athabasca vacuum residue was studied in both an open reactor (TGA) and a closed micro-batch reactor. Comparison of the results from both reactors with literature data showed that the thermal cracking reaction of the AVR in the TGA couldn't be modeled solely with a simple first-order reaction model. This conclusion is based on a significant error between the experimental and modeling results. In an attempt to improve the analysis of the TGA data, the thermal cracking reactions were modeled with a distribution model to describe the behavior of the sample during the reaction. In this model, the entire reaction was divided into several first-order reaction steps to separate the kinetic parameter of each step and make each step independent. It was found that models incorporating distributed reaction parameters following the Weibull or Gaussian distribution functions yielded average activation energies that were consistent with literature values. Additionally, the activation energies obtained in the micro-reactor study were consistent with the activation energies obtained from the TGA data processed using the probability distribution functions. As a result, it is recommended that researchers not to trust to simple methods of the TGA kinetics and work with the advanced methods to predict the kinetic parameters.

In the second part of this project, techniques were investigated to reduce the activation energies required for vacuum residue upgrading by modifying the reaction path. A low-level partial oxidation method was investigated to determine if it was possible to alter the reaction path. This method involved the thermal cracking and oxidation of the AVR either without or with α-FeO(OH) as a catalyst. Thermal cracking of the AVR was

modeled based on three products including coke plus resid, liquid and gas in the closed reactor. This division simplified the whole complicated reaction and caused to calculate activation energies by first-order reactions. The difference among the calculated activation energies indicated that rather than improving vacuum residue conversion, pre-oxidation makes heavier products that appear to be more stable against cracking. The net effect of pre-oxidation was a reduction in the production of gaseous and liquid products. In other words, it was indicated that the pre-oxidation of the AVR without catalyst at 180 ℃ reduces the reaction conversion of the liquid fraction of the AVR during thermal cracking. It is proposed that pre-oxidation resulted in the polymerization the vacuum residue molecules, The resulting pre-oxidized material was subsequently more resistant to thermal cracking than the unreacted feed. As a result, the data does not suggest the pre-oxidation of the AVR to improve the reaction conversion. On the other hand, upon the goal of research, pre-oxidation assists the produced coke to be thermally converted to gaseous products. Thus, this method might be useful for those projects that attempt to promote the gasification process. Goethite was not found to be an effective pre-oxidation catalyst. As a future work for the researchers, it can be recommended to investigate the effect of pre-oxidation of the AVR at higher temperatures, it might show the thermo-oxidative degradation against the recent results occurred at low temperatures.

Chapter 8: References

[1] Park, H. Y., & Kim, T. H. (2006). Non-isothermal pyrolysis of vacuum residue (VR) in a thermogravimetric analyzer. Energy Conversion and Management,47(15), 2118-2127.

[2] Park, Y. C., Paek, J. Y., Bae, D. H., & Shun, D. (2009). Study of pyrolysis kinetics of Alberta oil sand by thermogravimetric analysis. Korean Journal of Chemical Engineering, 26(6), 1608-1612.

[3] Sahu, M. K., Tewari, K., & Sinha, A. S. K. (2010). Oxidation of vacuum residue by ozone and nitrous oxide: FTIR Analysis. Indian Journal of Chemical Technology (Vol. 18). 91-98.

[4] Shih, S. M., & Sohn, H. Y. (1980). Nonisothermal determination of the intrinsic kinetics of oil generation from oil shale. Industrial & Engineering Chemistry Process Design and Development, 19(3), 420-426.

[5] Campbell, J. H., Koskinas, G. H., & Stout, N. D. (1978). Kinetics of oil generation from Colorado oil shale. Fuel, 57(6), 372-376.

[6] Torrente, M. C., & Galan, M. A. (2001). Kinetics of the thermal decomposition of oil shale from Puertollano (Spain). Fuel, 80(3), 327-334.

[7] Leavitt, D. R., Tyler, A. L., & Kafesjian, A. S. (1987). Kerogen decomposition kinetics of selected Green River and eastern US oil shales from thermal solution experiments. Energy & Fuels, 1(6), 520-525.

[8] Yutai, Q. (2000). Investigation of serial reaction kinetics and changes of group compositions of vacuum residues in continuous oxidization. Fuel, 79(14), 1815-1821.

[9] Trifirò, F., Carbucicchio, M., & Villa, P. L. (1998). Catalytic properties of iron-based mixed oxides in the oxidation of methanol and olefins. Hyperfine Interactions, 111(1), 17-22.

[10] Rahimi, P., & Gentzis, T. (2006). The chemistry of bitumen and heavy oil processing. Practical Advances in Petroleum Processing, 597-634.

[11] Wiehe, I. A. (1999). Tutorial on Resid Conversion and Coking. American Institute of Chemical Engineers.

[12] Wangen, E. S., McCaffrey, W. C., Kuznicki, S., Hoff, A., & Blekkan, E. A. (2007). Cracking of vacuum residue from Athabasca bitumen in a thin film.Topics in Catalysis, 45(1), 213-217.

[13] Whitehurst, D. D., Isoda, T., & Mochida, I. (1998). Present state of the art and future challenges in the hydrodesulfurization of polyaromatic sulfur compounds.Advances in Catalysis, 42, 345-471.

[14] Speight, J. G. (2006). The Chemistry and Technology of Petroleum (Vol. 114). CRC. 49, 134-145.

[15] Holmes, S. A. (1986). Nitrogen Functional Groups in Utah Tar Sand Bitumen and Produced Oils. AOSTRA J. Res, 2(3), 167.

[16] Boduszynski, M. M., & Altgelt, K. H. (1992). Composition of heavy petroleums. 4. Significance of the extended atmospheric equivalent boiling point (AEBP) scale. Energy & Fuels, 6(1), 72-76.

[17] Rahmani, S., McCaffrey, W., Elliott, J. A., & Gray, M. R. (2003). Liquid-phase behavior during the cracking of asphaltenes. Industrial & Engineering Chemistry Research, 42(17), 4101-4108.

[18] Wang, Z. X., Guo, A. J., & Que, G. H. (1998). Coke formation and characterization during thermal treatment and hydrocracking of Liaohe vacuum residuum. Prepr.□ Am. Chem. Soc., Div. Pet. Chem., 43, 530-533.

[19] Gray, M., (2011). Fundamentals of Oil Sands Upgrading. In Department of Chemical and Materials Engineering. Passed in Winter Term 2011. 100-112.

[20] Blanchard, C. M., & Gray, M. R. (1997). Free Radical Chain Reactions of Bitumen Residue. In Preprints of Symposia-Division of Fuel Chemistry American Chemical Society (Vol. 42), 137-141.

[21] Gray, M. R., & McCaffrey, W. C. (2002). Role of chain reactions and olefin formation in cracking, hydroconversion, and coking of petroleum and bitumen fractions. Energy & Fuels, 16(3), 756-766.

[22] Olmstead, W., & Freund, H. (1998). Thermal Conversion Kinetics of Petroleum Residua. In AIChE Spring Meeting, New Orleans, LA.

[23] Poutsma, M. L. (1990). Free-radical thermolysis and hydrogenolysis of model hydrocarbons relevant to processing of coal. Energy & Fuels, 4(2), 113-131.

[24] Wu, G., Katsumura, Y., Matsuura, C., Ishigure, K., & Kubo, J. (1996). Comparison of liquid-phase and gas-phase pure thermal cracking of n-hexadecane. Industrial & Engineering Chemistry Research, 35(12), 4747-4754.

[25] Shaw, J. M., Gaikwad, R. P., & Stowe, D. A. (1988). Phase splitting of pyrene-tetralin mixtures under coal liquefaction conditions. Fuel, 67(11), 1554-1559.

[26] White, J. L., Gopalakrishnan, M. K., & Fathollahi, B. (1994). A processing window for injection of mesophase pitch into a fiber preform. Carbon, 32(2), 301-310.

[27] Radmanesh, R., Chan, E., & Gray, M. R. (2008). Modeling of mass transfer and thermal cracking during the coking of Athabasca residues. Chemical Engineering Science, 63(6), 1683-1691.

[28] Yue, C., & Watkinson, A. P. (1998). Pyrolysis of pitch. Fuel, 77(7), 695-711.

[29] Schucker, R. C. (1983). Thermogravimetric determination of the coking kinetics of Arab heavy vacuum residuum. Industrial & Engineering Chemistry Process Design and Development, 22(4), 615-619.

[30] Thakur, D. S., & Nuttall Jr, H. E. (1987). Kinetics of pyrolysis of Moroccan oil shale by thermogravimetry. Industrial & Engineering Chemistry Research, 26(7), 1351-1356.

[31] Ahmaruzzaman, M., & Sharma, D. K. (2005). Non-isothermal kinetic studies on co-processing of vacuum residue, plastics, coal and petrocrop. Journal of Analytical and Applied Pyrolysis, 73(2), 263-275.

[32] Gray, M. R., Le, T., McCaffrey, W. C., Berruti, F., Soundararajan, S., Chan, E., ... & Thorne, C. (2001). Coupling of mass transfer and reaction in coking of thin films of an Athabasca vacuum residue. Industrial & Engineering Chemistry Research, 40(15), 3317-3324.

[33] Gray, M. R., McCaffrey, W. C., Huq, I., & Le, T. (2004). Kinetics of cracking and devolatilization during coking of Athabasca residues. Industrial & Engineering Chemistry Research, 43(18), 5438-5445.

[34] Wiehe, I.A., 1993. Phase-separation kinetic model for coke formation. Industrial & Engineering Chemistry Research 32 (11), 2447–2454.

[35] Dutta, R. P., McCaffrey, W. C., Gray, M. R., & Muehlenbachs, K. (2001). Use of 13C tracers to determine mass-transfer limitations on thermal cracking of thin films of bitumen. Energy & Fuels, 15(5), 1087-1093.

[36] Reid, R. C., Prausnitz, J. M., & Poling, B. E. (1987). The properties of gases and liquids. 675-677.

[37] Aminu, M. O., Elliott, J. A., McCaffrey, W. C., & Gray, M. R. (2004). Fluid properties at coking process conditions. Industrial & Engineering Chemistry Research, 43(12), 2929-2935.

[38] Tosun, I. (2007). Modeling in transport phenomena: A Conceptual Approach. Elsevier Science. 35-57

[39] Babu, D. R., & Cormack, D. E. (1984). Effect of low-temperature oxidation on the composition of Athabasca bitumen. Fuel, 63(6), 858-861.

[40] Hassan, A., Carbognani, L., & Pereira-Almao, P. (2008). Effect of O2 on Microcarbon Residue Standards Analysis. Energy & Fuels, 22(6), 4062-4069.

[41] Kotov, S. V., Levanova, S. V., Madumarova, Z. R., Pogulyaiko, V. A., Zinov'eva, L. V., & Tyshchenko, V. A. (2009). Influence of the hydrocarbon composition of vacuum residues on their kinetic behavior in oxidation.Petroleum Chemistry, 49(3), 225-228.

[42] Hassan, A., Carbognani, L., & Pereira-Almao, P. (2010). Oxidation of Oils and Bitumen at Various O2 Concentrations. Energy & Fuels, 24(10), 5378-5386.

[43] Paramguru, R. K., Rath, P. C., & Misra, V. N. (2004). Trends in red mud utilization–A review. Mineral Processing & Extractive Metall. Rev., 26(1), 1-29.

[44] Li, X. B., Xiao, W., Liu, W., Liu, G. H., Peng, Z. H., Zhou, Q. S., & Qi, T. G. (2009). Recovery of alumina and ferric oxide from Bayer red mud rich in iron by reduction sintering. Transactions of Nonferrous Metals Society of China, 19(5), 1342-1347.

[45] Aquino, A. J., Tunega, D., Haberhauer, G., Gerzabek, M. H., & Lischka, H. (2008). Acid–base properties of a goethite surface model: A theoretical view.Geochimica et Cosmochimica Acta, 72(15), 3587-3602.

[46] Alvarez, J., Rosal, R., & Sastre, H. (1998). Characterization and deactivation studies of an activated sulfided red mud used as hydrogenation catalyst.Applied Catalysis A: General, 167(2), 215-223.

[47] Lu, M. C. (2000). Oxidation of chlorophenols with hydrogen peroxide in the presence of goethite. Chemosphere, 40(2), 125-130.

[48] Chung, K. H., Xu, C., Hu, Y., & Wang, R. (1997). Supercritical fluid extraction reveals resid properties. Oil and Gas Journal, 95(3), 66-69.

[49] Sánchez, S., Ancheyta, J., & McCaffrey, W. C. (2007). Comparison of probability distribution functions for fitting distillation curves of petroleum.Energy & Fuels, 21(5), 2955-2963.

[50] Whitson, C. H., Anderson, T. F., & Sqreide, I. (1990). Application of the gamma distribution model to molecular weight and boiling point data for petroleum fractions. Chemical Engineering Communications, 96(1), 259-278.

[51] Dhulesia, H. (1984). Equation fits ASTM distillations. Hydrocarbon Processing,62(9), 179-180.

[52] Riazi, M. R. (1989). Distribution model for properties of hydrocarbon-plus fractions. Industrial & Engineering Chemistry Research, 28(11), 1731-1735.

[53] Nadarajah, S., & Zografos, K. (2005). Expressions for Rényi and Shannon entropies for bivariate distributions. Information Sciences, 170(2), 173-189.

[54] Lin, L. C., Deo, M. D., Hansonf, F. V., & Oblad, A. G. (1990). Kinetics of tar sand pyrolysis using a distribution of activation energy model. AIChE Journal,36(10), 1585-1588.

[55] Braun, R. L., & Burnham, A. K. (1987). Analysis of chemical reaction kinetics using a distribution of activation energies and simpler models. Energy & Fuels,1(2), 153-161.

[56] Golikeri, S. V., & Luss, D. (1972). Analysis of activation energy of grouped parallel reactions. AIChE Journal, 18(2), 277-282.

[57] Gautschi, W., & Cahill, W. F. (1964). Handbook of Mathematical Functions. National Bureau of Standards, Washington, 298.

[58] Whitley, D. (1994). A genetic algorithm tutorial. Statistics and Computing, 4(2), 65-85.

[59] Burnham, K. P., & Anderson, D. R. (2002). Model selection and multi-model inference: a practical information-theoretic approach. Springer Verlag. 295.

[60] Singh, J., Kumar, M. M., Saxena, A. K., & Kumar, S. (2005). Reaction pathways and product yields in mild thermal cracking of vacuum residues: A multi-lump kinetic model. Chemical Engineering Journal, 108(3), 239-248.

[61] Payzant, J. D., Lown, E. M., & Strausz, O. P. (1991). Structural units of Athabasca asphaltene: The aromatics with a linear carbon framework. Energy & fuels, 5(3), 445-453.

[62] Sheu, E. Y., Storm, D. A., & De Tar, M. M. (1991). Asphaltenes in polar solvents. Journal of Non-Crystalline Solids, 131, 341-347.

[63] Wiehe, I. A. (1999). Tutorial on the phase behavior of asphaltenes and heavy oils. AIChE Spring National Meeting, 3-8

[64] Carraher, C. E. (2010). Introducyion to Polymer Chemistry. New York: CRC press, Taylor and Francis. p. 224

[65] Pojman, John A.; Jason Willis, Dionne Fortenberry, Victor Ilyashenko, Akhtar M. Khan (1995). "Factors affecting propagating fronts of addition polymerization: Velocity, front curvature, temperatue profile, conversion, and molecular weight distribution". Journal of Polymer Science Part A: Polymer Chemistry **33** (4): 643–652

[66] Peterson, J. D., Vyazovkin, S., & Wight, C. A. (2001). Kinetics of the thermal and thermo-oxidative degradation of polystyrene, polyethylene and poly (propylene). Macromolecular Chemistry And Physics, 202(6), 775-784.

[67] Blake Olson, M.Sc. Thesis (Spring 2013), “The Role of Sulfur During the Cracking of n-Hexadecane and Cold Lake Bitumen with α-Fe2O3 and Steam”. 25-27.

[68] Silverman, M. A.; Pavel, S. K.; Hillerman, M. D. HTL Heavy Oil Upgrading: A key solution for heavy oil upstream and midstream operations. In World Heavy Oil Congress, Edmnonton, AB, March 14–17, 2011; p 7

[69] Vafi, K., McCaffrey, W. C., & Gray, M. R. (2012). Minimization of Coke in Thermal Cracking of Athabasca Vacuum Residue in a High-Temperature Short-Residence Time Continuous Flow Aerosol Reactor. Energy & Fuels, 26(10), 6292-6299.

Appendixes

Appendix A

A-1: MATALAB code for the Open Reactor Model

Reaction Kinetic:

```
function f = innerIntegral(A,E,R,T,ti)
sum = 0;
a1=2.334733;
a2=0.250621;
b1=3.330657;
b2=1.681534;
for i = 1:length(ti)-1
%     sum = sum + A*exp(-E(end)/(R*T(i)))*(ti(i+1)-ti(i));
%     sum=sum+(A*exp(-E(end)/(R*T(i)))+A*exp(-E(end)/(R*T(i+1))))*(ti(i+1)-
ti(i))/2;
    p1=(ti(i+1)-ti(i))/(T(i+1)-T(i));
    ac1=T(i+1)*A*exp(-E(end)/(R*T(i+1)));
    ac2=1-
((E(end)/(R*T(i+1)))^2+a1*(E(end)/(R*T(i+1)))+a2)/((E(end)/(R*T(i+1)))^2+b1*(E(end
)/(R*T(i+1)))+b2);
    ac3=1-
((E(end)/(R*T(i)))^2+a1*(E(end)/(R*T(i)))+a2)/((E(end)/(R*T(i)))^2+b1*(E(end)/(R*T
(i)))+b2);
    deltaI=p1*(ac1*ac2-T(i)*A*exp(-E(end)/(R*T(i)))*ac3);
    sum = sum +deltaI;
end
f = sum;
```

```
function calc=outerintegrant6(E,A,T,R,ti,currentIndex)

innerInteg=innerIntegral(A,E,R,T(1:currentIndex),ti(1:currentIndex));

A*exp(-E/(R*T(currentIndex)))*exp(-innerInteg)*(fi/beta)*( (E-alpha)/beta)^(fi-
1)*exp(-((E-alpha)/beta)^fi)% For Weibull distribution function
```

Numerical Calculation:

```
function f=RSS(x)
clc
load 25File.mat; % Loads the TGA data
E0 = 205372;
A = 6.57101301E+12;
R = 8.314;
beta=2000;
alph=10;
fi=x(1);

OuterInteg = zeros(length(dwdt),1);
   for n = 1:length(dwdt);
       currentIndex=n;

OuterInteg(n)=quadv(@(E)outerintegrant6(E,A,T,R,ti,currentIndex),0,400000);

   end
```

```
f=((OuterInteg-dwdt))'*((OuterInteg-dwdt));
```

Plot:

```
load 25jadidbell.mat;
E0 = 205372;
A = 6.57101301E+12;
R = 8.314;
beta=224740;
alph=26.3750;
fi=16.82386;

OuterInteg = zeros(length(dwdt),1);
        for n = 1:length(dwdt);
            currentIndex=n;

OuterInteg(n)=quadv(@(E)outerintegrant6(E,A,T,R,ti,currentIndex),0,400000);
        end
x=linspace(0,1500,29);
plot(ti,OuterInteg,'red');
hold on
plot(ti,dwdt,'blue');
legend('Numerical','Experimental');
```

Optimization Method:

```
clc
lb=(1);
ub=(50);
options =
gaoptimset('PopulationSize',3000,'Generations',20000,'Display','iter','TolFun',1e-
100);
[x,fval,exitflag]=ga(@RSS,1,[],[],[],[],lb,ub,[],options);
```

A-2: MATLAB code for the Closed Reactor Model

Reaction Kinetic:

```
function f=gas(x)

x(4)=x(1)+x(2);
t=30;
f1=(x(2)/x(4))*(exp(-x(4)*t)-1)-((x(3)*x(1))/(x(4)*(x(3)-x(4))))*(exp(-x(4)*t)-
1)+(x(3)*x(1)/(x(3)*(x(3)-x(4))))*(exp(-x(3)*t)-1);
if (f1 <= 1)
    f=f1;
else
    f1=1;
end
if (f1 >= 0)
    f=f1;
else
    f=0;
end


function f=liquid(x)

x(6)=x(1)+x(2)+x(3);
x(7)=x(5)+x(4);
W=1;
t=30;
f1=-1*(((x(1)+x(2))*W/x(6))*(exp(-x(6)*t)-1)-(x(1)*x(5)*W/(x(6)*(x(7)-
x(6))))*(exp(-x(6)*t)-1)+(x(1)*x(5)*W/(x(7)*(x(7)-x(6))))*(exp(-x(7)*t)-1));
```

```
if (f1 <= 1)
    f=f1;
else
    f1=1;
end
if (f1 >= 0)
    f=f1;
else
    f=0;
end


function f=liquidlong(x)

x(6)=x(1)+x(2)+x(3);
x(7)=x(5)+x(4);
W=1;
t=60;
f1=-1*((x(3)*W/x(6))*(exp(-x(6)*t)-1)+(x(1)*x(5)*W/(x(6)*(x(7)-x(6))))*(exp(-
x(6)*t)-1)-(x(1)*x(5)*W/(x(7)*(x(7)-x(6))))*(exp(-x(7)*t)-1));
if (f1 <= 1)
    f=f1;
else
    f1=1;
end
if (f1 >= 0)
    f=f1;
else
    f=0;
end

function f=vgo(x)

x(4)=x(1)+x(2);
t=30;
f1=(x(1)/(x(3)-x(4)))*(exp(-x(4)*t)-exp(-x(3)*t));
if (f1 <= 1)
    f=f1;
else
    f1=1;
end
if (f1 >= 0)
    f=f1;
else
    f=0;
end

function f=vgolong(x)

x(4)=x(1)+x(2);
t=60;
f1=(x(1)/(x(3)-x(4)))*(exp(-x(4)*t)-exp(-x(3)*t));
if (f1 <= 1)
    f=f1;
else
    f1=1;
end
if (f1 >= 0)
    f=f1;
else
    f=0;
end
```

Optimization Method:

```
clc

clear all
lb=[0,0,0,0,0];
ub=[0.01,0.01,0.01,0.01,0.01];
```

```
options=gaoptimset('PopulationSize',3000,'Generations',20000,'Display','iter','Tol
Fun',1e-100);
[x,fval,exitflag]=ga(@(x)RSS1(x),5,[],[],[],[],[],[],lb,ub,[],options)


function f=RSS1(x)

x(6)=x(1)+x(2)+x(3);
x(7)=x(5)+x(4);

f=abs(liquid(x)-0.6211)/(liquid(x))+abs(vgo(x)-0.5673)/(vgo(x))+abs(liquidlong(x)-
0.4656)/(liquidlong(x))+abs(gaslong(x)-0.4327)/(gaslong(x))+abs(vgolong(x)-
0.4868)/(vgolong(x));
```

Appendix B

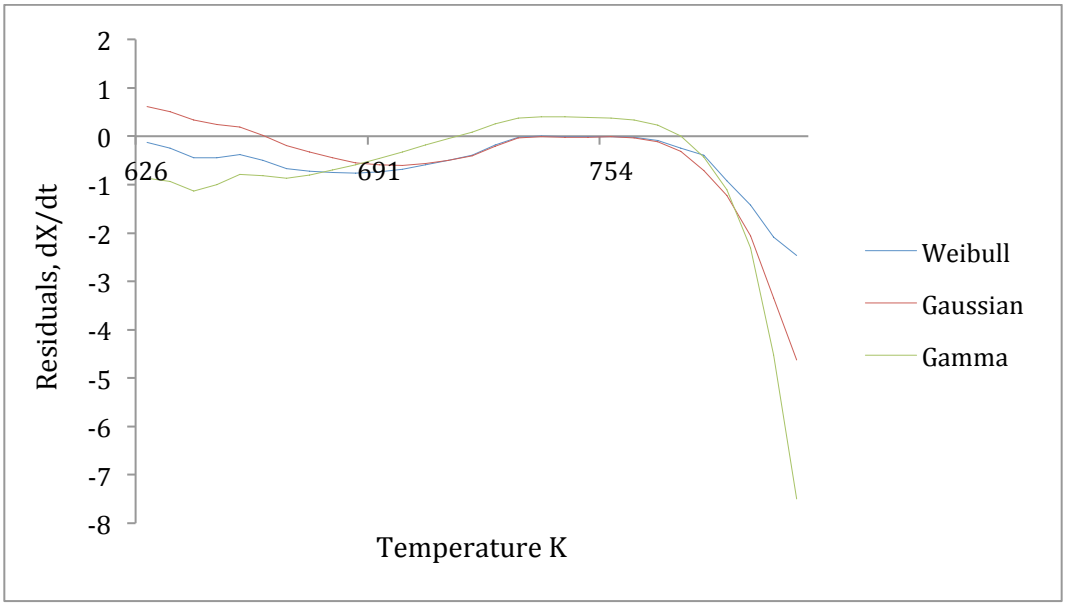

Figure B-1: Residuals of model versus different distribution functions at 25 K/min

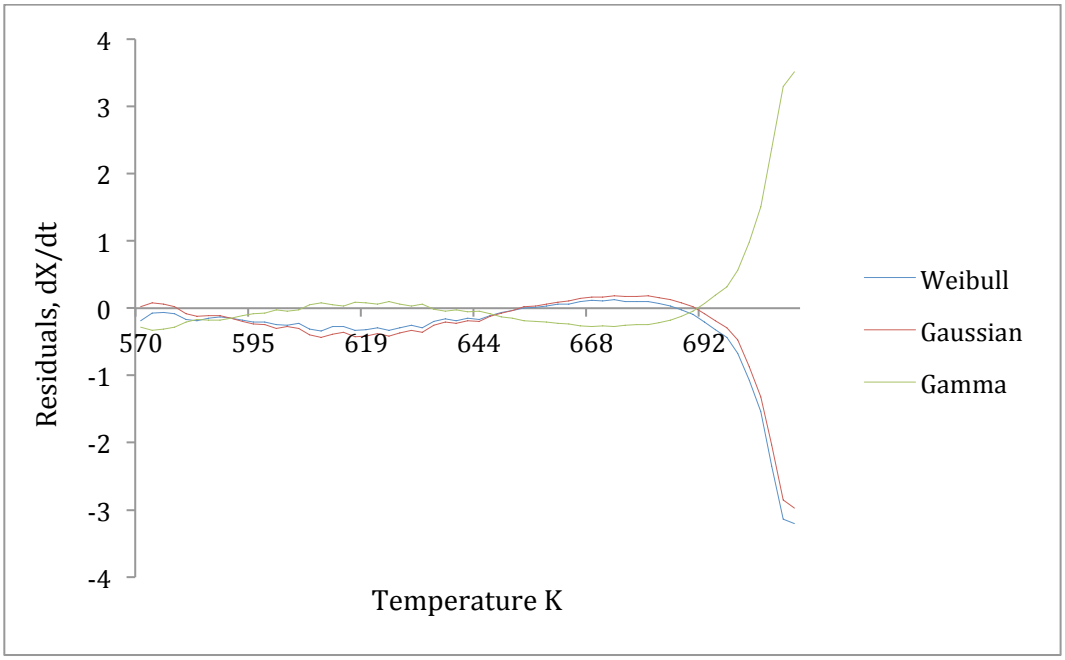

Figure B-2: Residuals of model versus different distribution functions at 0.5 K/min

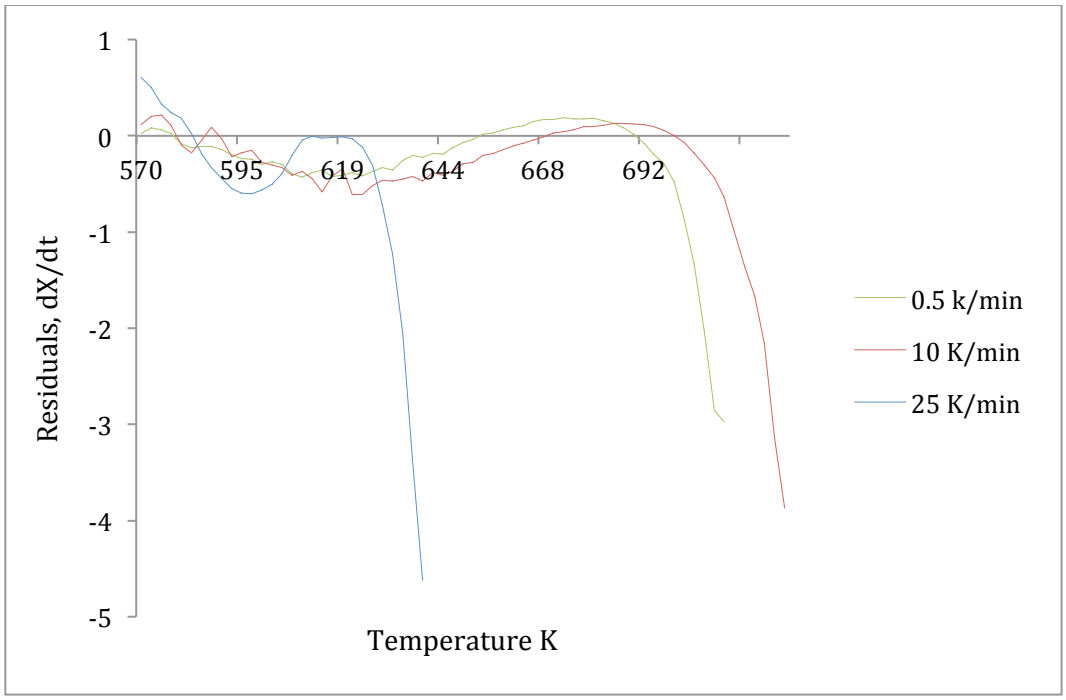

Figure B-3. Residuals of Gaussian model versus different heating rates

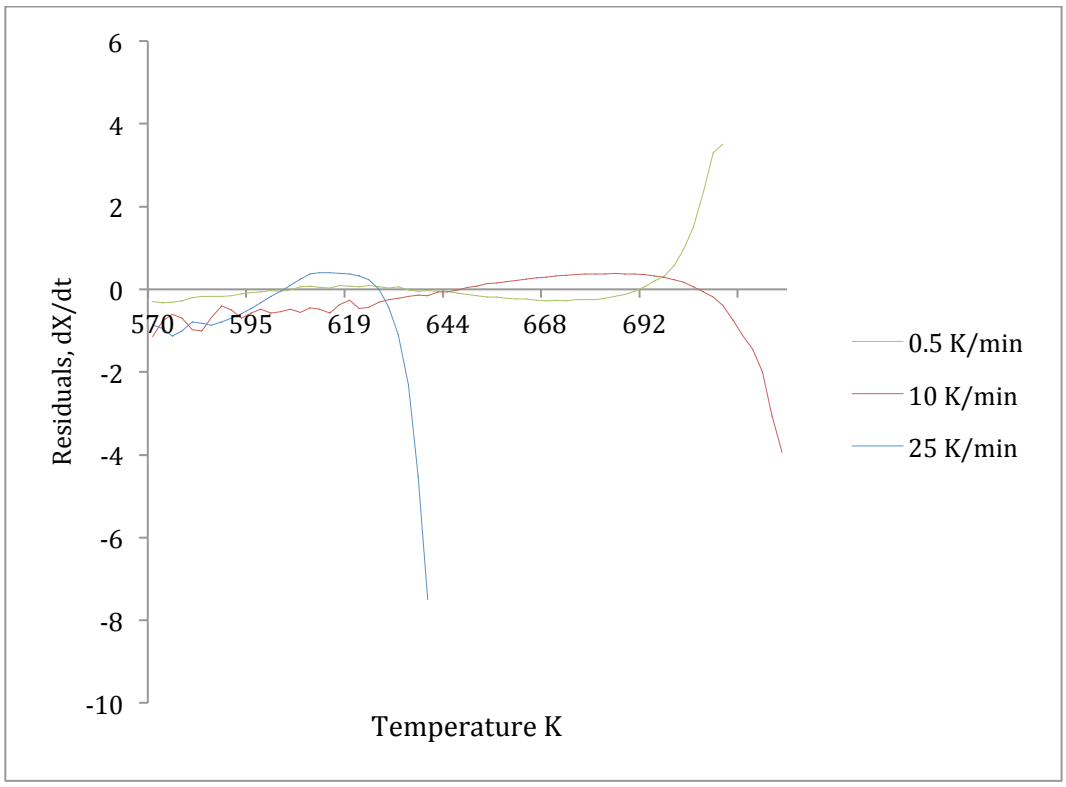

Figure B-4. Residuals of Gamma model versus different heating rates

Appendix C

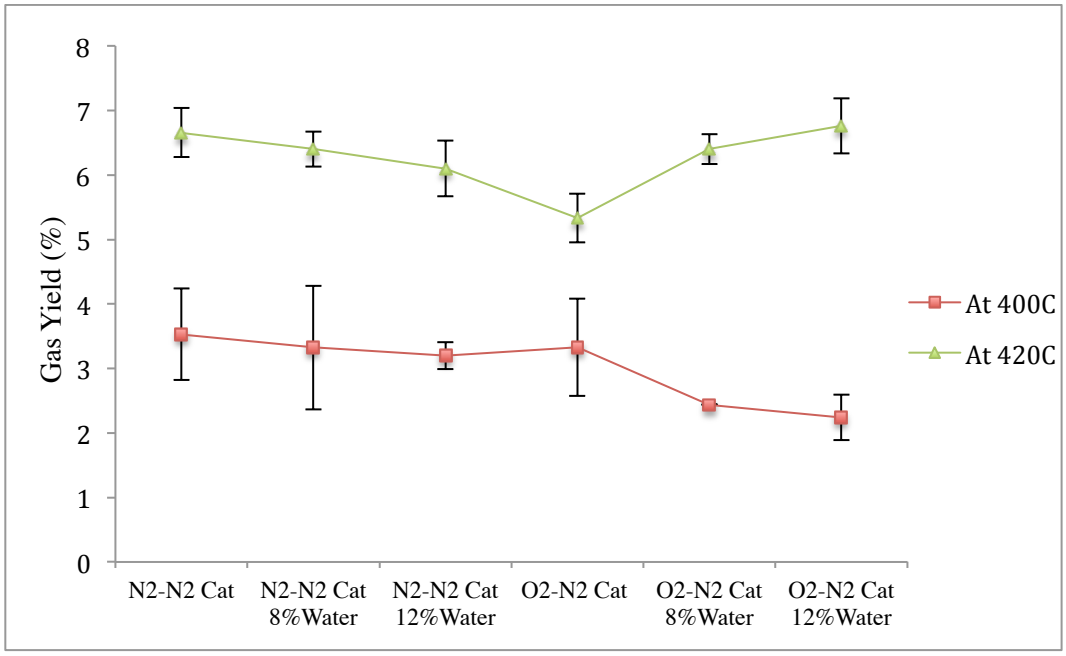

Figure C-1. Gas yield of AVR in a batch reactor during thermal cracking with the presence of water with two different concentrations and goethite 10% wt.

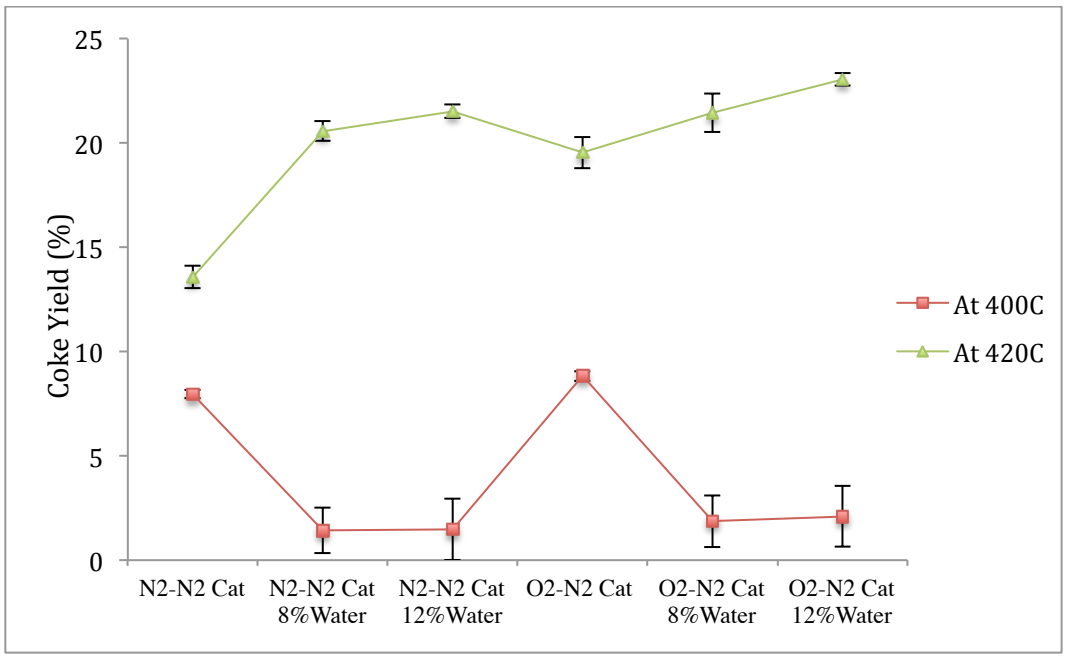

Figure C-2. Coke yield of AVR in a batch reactor during thermal cracking with the presence of water with two different concentrations and goethite 10% wt.

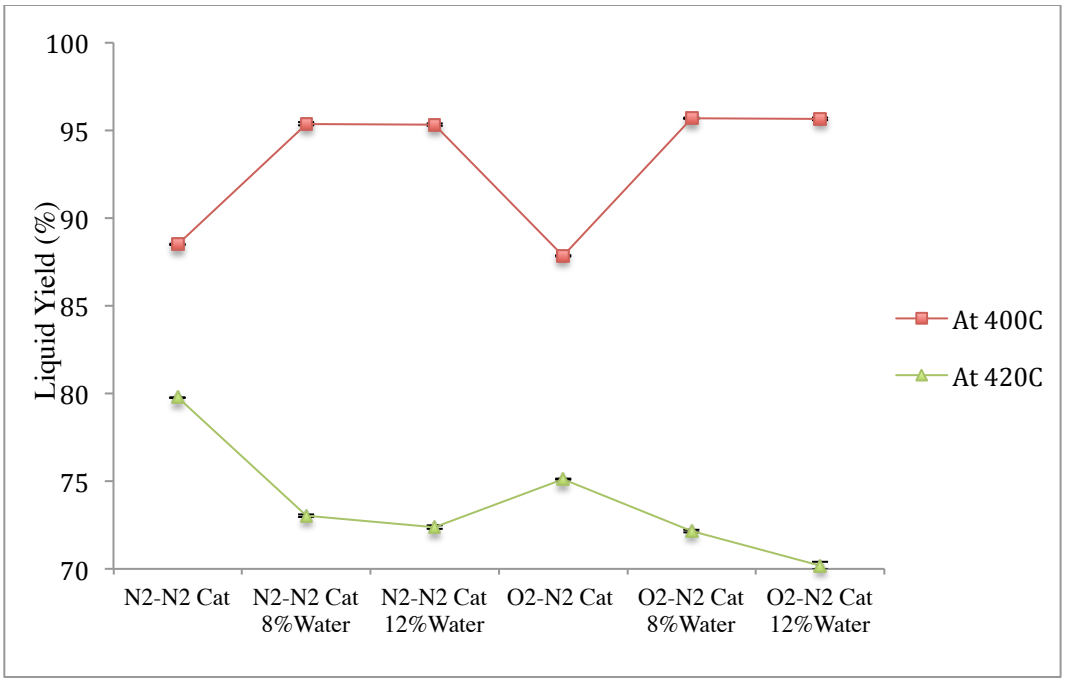

Figure C-3. Liquid yield of AVR in a batch reactor during thermal cracking with the presence of water with two different concentrations and goethite 10% wt.